Astronomy Reports, Vol. 44, No. 5, 2000, pp. 279–285. Translated from Astronomicheskiĭ Zhurnal, Vol. 77, No. 5, 2000, pp. 323–330.

Dynamics and Stability of Resonant Rings in Galaxies

B. P. Kondrat'ev

Udmurt State University, Krasnoarmeĭskaya ul. 71, Izhevsk, 426034 Russia

Received December 24, 1998

Abstract—We have developed a model for a spheroidal, ring-shaped galaxy. The stars move in a ring with an elliptical cross section at the 1 : 1 frequency resonance. The shape of the cross section of the equilibrium ring depends on the oblateness of the galaxy itself, so that the ellipse of the ring cross section is radially extended when the oblateness of the galaxy is small. If the oblateness of galaxy exceeds some critical value, the ellipse cross section is extended along the Ox_3 axis. The shape of the ring cross section is circular for a galaxy with critical eccentricity. The stability of the ring over a wide range of perturbations is studied. A fundamental bicubic dispersion equation for the frequencies of small oscillations of a perturbed ring is derived. Application of the model to the ring galaxy NGC 7020 shows that its ring cross section should be approximately circular. Analysis of the dispersion equation demonstrates that stellar orbits in the arm are unstable (but the instability increment is small). We conclude that stars in the ring of this galaxy should drift from the 1 : 1 resonance, and the ring itself should evolve. *© 2000 MAIK "Nauka/Interperiodica".*

1. INTRODUCTION

The rings (or partial ring structures) existing in many galaxies have long attracted the attention of theorists. The abundance of such stellar systems was emphasized, for example, in [1], which notes about 200 flat galaxies with ring structures. The most prominent example of a galaxy possessing a distinct nucleus–ring combination (outwardly similar to Saturn and its rings) is NGC 7702. According to [2], this galaxy has not one but two well-separated rings. The well-known examples [3–5] indicate that ring and spiral-arm structures have similar compositions and stellar dynamics. Investigations of such structures are necessary if we wish to elucidate the important role of secular evolution processes in spiral and SO galaxies.

The existence of ring galaxies is a serious theoretical problem. A quite simple stellar dynamical model for a galactic ring was developed and its stability studied in [6]. That paper was primarily concerned with general collective effects in the dynamics of prolate structures, whereas the dynamics of individual stars within such structures were not studied. However, the existence of prolate structures and circular rings is possible only if there are certain definite relations between the parameters of stellar orbits and the corresponding first integrals of motion. Precisely the character of individual orbits is the decisive factor determining the particular form of the components of the velocity dispersion tensor, and pressure anisotropy in the "stellar gas," which is characterized by these components, will considerably affect the stability of rings in galaxies.

Therefore, when considering the orbits of individual stars in the arms, we should first and foremost examine possible resonances. This is especially important since the evolution of dynamical systems often leads to the appearance of various commensurability ratios. Recall that our solar system is literally saturated with resonances between the frequencies of the spin–orbital motions of planets and satellites [7].

Galaxies are the oldest stellar systems and have undergone long periods of evolution. Therefore, we can assume that resonances could be formed in galaxies in much the same way as in the solar system. Taking such resonances into account when developing galactic models can radically change the dynamical properties of the models.[1] Therefore, when constructing models for ring galaxies, we should first and foremost investigate the dynamical consequences of resonances between the frequencies of small oscillations of stars in a plane of the ring cross section.

The present paper is concerned with a stellar dynamical model for a ring galaxy with a local 1 : 1 resonance of the frequencies of stellar motions in a circular arm with an elliptical cross section. The equilibrium model itself is developed in Sections 2–5, and its stability is studied in Sections 6–10. We apply this model to the ring galaxy NGC 7020, whose structure was studied in detail in [9].

2. EQUATIONS OF STELLAR MOTION IN AN ELLIPTICAL ARM

Let us consider an axially symmetric galaxy possessing a uniform circular arm with density ρ and ellip-

[1] See, for example, [8], which describes a self-consistent phase model for a spheroidal galaxy with an additional resonant integral of the stellar motion. Torus-shaped vortex motions of the centroids arise in this model, in agreement with both observations and numerical experiments in the framework of the *N*-body problem.

1063-7729/00/4405-0279$20.00 © 2000 MAIK "Nauka/Interperiodica"

tical cross section. The arm is characterized by a cross section with semi-axes a_1 and a_3:

$$\frac{x_3^2}{a_3^2} + \frac{\xi^2}{a_1^2} = 1, \quad a_1 \geq a_3, \tag{1}$$

(where $\xi = R - R_0$), and is filled with stellar orbits. Since the cross section and curvature of the generatrices of the arm are small, we can take its inner potential at the point (ξ, x_3) in the form

$$\varphi_p = \text{const} - \alpha_1 \xi^2 - \alpha_3 x_3^2, \tag{2}$$

which is typical for a uniform two-dimensional elliptical cylinder with straight generatrices. The constant coefficients in expression (2) are equal to

$$\alpha_1 = 2\pi G\rho \frac{a_3}{a_1 + a_3}; \quad \alpha_3 = 2\pi G\rho \frac{a_1}{a_1 + a_3}. \tag{3}$$

A star in the arm is also affected by the gravitational field of the galaxy itself. Let us expand the galactic field potential in a Taylor series in powers of ξ and x_3 in the neighborhood of the arm. Then, with accuracy up to quadratic terms, we obtain

$$\varphi_g = \text{const} - \Omega_c^2 R_0 \xi - A_1 \xi^2 - A_3 x_3^2. \tag{4}$$

Here,

$$\Omega_c^2(R_0) = -\left(\frac{1}{R}\frac{\partial \varphi_g}{\partial R}\right)_{R = R_0} \tag{5}$$

is the square of the angular velocity in a reference orbit with radius R_0 from the galaxy center and the coefficients of the potential are equal to

$$A_1 = -\frac{1}{2}\left(\frac{\partial^2 \varphi_g}{\partial R^2}\right)_{\substack{R = R_0 \\ x_3 = 0}}, \quad A_3 = -\frac{1}{2}\left(\frac{\partial^2 \varphi_g}{\partial x_3^2}\right)_{\substack{R = R_0 \\ x_3 = 0}}. \tag{6}$$

The total potential inside the arm is the sum of the contributions:

$$\begin{aligned} \varphi &= \varphi_P + \varphi_g \\ &= \text{const} - \Omega_c^2 R_0 \xi - (\alpha_1 + A_1)\xi^2 - (\alpha_3 + A_3)x_3^2. \end{aligned} \tag{7}$$

The initial equations for the motion of a star inside the arm in cylindrical coordinates (R, θ, x_3) are well-known:

$$\begin{aligned} \ddot{R} &= \frac{\partial \varphi}{\partial R} + R\dot{\theta}^2, \\ \frac{d}{dt}(R^2\dot{\theta}) &= \frac{\partial \varphi}{\partial \theta}, \\ \ddot{x}_3 &= \frac{\partial \varphi}{\partial x_3}. \end{aligned} \tag{8}$$

When solving this system of equations, we first note the quadratic dependence (7) of φ on x_3. As a result, motion along the corresponding axis is described by the equation of a one-dimensional harmonic oscillator

$$\ddot{x}_3 = -2(\alpha_3 + A_3)x_3, \tag{9}$$

and obviously does not depend on motions along the R and θ directions.

Let us simplify the problem and assume that the distribution of mass in the galaxy and ring possesses circular symmetry; i.e.,

$$\frac{\partial \varphi}{\partial \theta} = 0. \tag{10}$$

Next, let us consider a coordinate system rotating with angular velocity Ω_c:

$$\theta(t) = \tilde{\theta}(t) + \Omega_c t. \tag{11}$$

Then, the first two equations of (8) take the form

$$\begin{aligned} \ddot{R} &= \frac{\partial \varphi}{\partial R} + R(\dot{\tilde{\theta}} + \Omega_c)^2, \\ \frac{d}{dt}(R^2\dot{\tilde{\theta}}) &= -2R\Omega_c\dot{R}. \end{aligned} \tag{12}$$

Consequently, we obtain in a linear approximation with respect to ξ and $\dot{\tilde{\theta}}$

$$\ddot{\xi} = (\Omega_c^2 - 2\alpha_1 - 2A_1)\xi + 2R_0\Omega_c\dot{\tilde{\theta}} \tag{13}$$

and

$$R_0\ddot{\tilde{\theta}} = -2\Omega_c\dot{\xi}. \tag{14}$$

By substituting $\eta = R_0\tilde{\theta}$ into the last two equations and using (9), the complete system of equations for the stellar motion can be reduced to the form

$$\begin{aligned} \ddot{\xi} &= (\Omega_c^2 - 2\alpha_1 - 2A_1)\xi + 2\Omega_c\dot{\eta}, \\ \ddot{\eta} &= -2\Omega_c\dot{\xi}, \\ \ddot{x}_3 &= -2(\alpha_3 + A_3)x_3. \end{aligned} \tag{15}$$

After the first integration (to within a constant, which is not important in our consideration), the middle equation of system (15) gives

$$\dot{\eta} = -2\Omega_c\xi. \tag{16}$$

Substituting (16) into the right-hand side of the first equation of (15), we finally obtain the equations of a two-dimensional harmonic oscillator,

$$\begin{aligned} \ddot{\xi} &= -\omega_1^2\xi, \\ \ddot{x}_3 &= -\omega_3^2 x_3, \end{aligned} \tag{17}$$

where we have introduced the parameters

$$\omega_1^2 = 3\Omega_c^2 + 2(\alpha_1 + A_1), \qquad \omega_3^2 = 2(\alpha_3 + A_3). \tag{18}$$

In particular, when the arm is absent (i.e., $\alpha_1 = \alpha_3 = 0$), the first relation of (18) can be written in the equivalent form

$$\frac{3}{R}\frac{\partial \varphi_g}{\partial R} + \frac{\partial^2 \varphi_g}{\partial R^2} < 0, \tag{19}$$

leading to the well-known criterion for the stability of circular orbits (see, for example, [10]).

3. STELLAR MOTIONS AT THE FREQUENCY RESONANCE

The solution of system (17) can be written in the form

$$\xi = C_1 \cos(\omega_1 t + k_1), \qquad x_3 = C_3 \sin(\omega_3 t + k_3). \tag{20}$$

Next, we require that the stellar orbits be closed in the meridional plane of the arm; i.e., that they be represented by Lissajous figures. In this case, the ratio of the oscillation frequencies must be a rational number:

$$\frac{\omega_1}{\omega_2} = \frac{m}{n}. \tag{21}$$

In addition, the condition of conservation of the ellipse boundary (1) must be satisfied for all stellar orbits. We shall consider here the simplest case of equal frequencies (i.e., the 1 : 1 resonance) and initial phases:

$$\omega_1 = \omega_3, \quad k_1 = k_3. \tag{22}$$

Then, the motion of a star is described by the formulas

$$\xi(t) = C_1 \cos(\omega_1 t + k_1), \qquad x_3(t) = C_3 \sin(\omega_1 t + k_1) \tag{23}$$

and under the condition

$$\frac{C_1}{C_3} = \frac{a_1}{a_3}, \tag{24}$$

the stars move along ellipses similar to the boundary ellipse (1). Such an arm, resembling a swiss roll, consists of concentric tori with homothetic elliptical cross sections. Consequently, the condition that the boundary (1) be conserved is satisfied.

Note that equality (22) implies the relation

$$\Psi = 3\Omega_c^2 + 2(A_1 - A_3) = 4\pi G\rho\frac{1-\chi}{1+\chi} \tag{25}$$

between the ratio of the semi-axes of the arm cross section $\chi = a_3/a_1$ and the parameters of the galaxy itself.

4. SLOW EVOLUTION OF A RING GALAXY

In the case of slow evolution, the adiabatic invariants must be conserved. In accordance with (17), we have a harmonic oscillator with respect to ξ and x_3. Consequently, as is well known [11], the products of the squares of the amplitudes and the frequency are conserved:

$$a_1^2\sqrt{3\Omega_c^2 + 2(\alpha_1 + A_1)} = a_3^2\sqrt{2(\alpha_3 + A_3)}. \tag{26}$$

In addition, the mass per unit length of the arm should be conserved:

$$\rho a_1 a_2 = \text{const}. \tag{27}$$

The system of equations (25), (26), and (27) determines variations in the arm parameters during the secular evolution of the stellar system.

5. MODEL CALCULATIONS

As a simple equilibrium model of a galaxy, let us consider a nonuniform stratified spheroid with similar layers and the realistic normalized density distribution [12]

$$\rho(m^2) = \frac{1}{[1+\beta m^2]^{3/2}}, \tag{28}$$

where

$$m^2 = \frac{R^2}{\tilde{a}_1^2} + \frac{x_3^2}{\tilde{a}_3^2} \quad \text{and} \quad 0 \le m \le 1,$$

$\tilde{a}_1$ and $\tilde{a}_3$ are the semi-axes of the spheroidal galaxy itself, and β is a constant that can be derived from photometric data.

It follows from (25) that

$$\chi = \frac{1 - \dfrac{\Psi}{4\pi G\rho(R_0)}}{1 + \dfrac{\Psi}{4\pi G\rho(R_0)}}, \tag{29}$$

where

$$\rho(R_0) = \frac{1}{[1+\beta R_0^2]^{3/2}}. \tag{30}$$

As a result (for details, see the *Appendix*), the expression for Ψ from (25) will be equal to

$$\Psi(e) = \frac{4\pi G}{e^2 + \beta R_0^2} \times \left\{2\sqrt{\frac{1-e^2}{e^2+\beta R_0^2}}\left[\frac{e^2(F-E)}{\beta R_0^2} + E\right] - \frac{2 - e^2 + \beta R_0^2}{(1+\beta R_0^2)^{3/2}}\right\}. \tag{31}$$

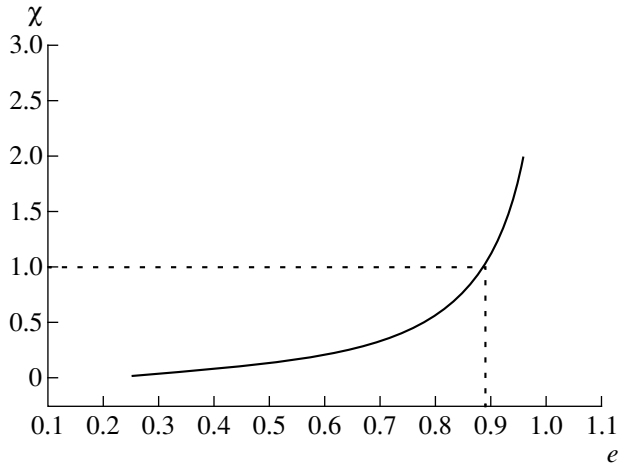

Dependence of the semi-axis ratio $\chi = a_3/a_1$ of the elliptical cross section of an equilibrium ring at the 1 : 1 frequency resonance on the eccentricity of the meridional cross section e of a spheroidal galaxy with density distribution (28). The calculations were conducted for NGC 7020. We found, in accordance with the photometric data [9], that $\beta \approx 100$, $R_0/\tilde{a}_1 \approx 0.6$, and $e \approx 0.89$. The ellipse of the arm cross section turns into a circle at $e_{cr} \approx 0.88$.

Here, $e = \sqrt{1 - \left(\frac{\tilde{a}_3}{\tilde{a}_1}\right)^2}$ is the eccentricity of a meridional cross section of the galaxy (and all its layers of equal density), R_0 is normalized to $\tilde{a}_1$, and F and E are elliptical integrals of the first and second kinds.

Formulas (31) and (29) specify the ratio of the semiaxes $\chi = a_3/a_1$ of the arm as a function of the eccentricity e of the galactic layers β via the parameters $R_0/\tilde{a}_1$ (the central radius of the arm) and β. The calculations showed that the dependence of χ on β and $R/\tilde{a}_1$ is quite weak over a wide range of their values. Therefore, it is possible that the results of our calculations, with reasonable accuracy, are characteristic for many ring galaxies. Of course, the condition of azimuthal symmetry in these objects must be satisfied. This is true, for example, for the ring galaxy NGC 7020. The corresponding plot of $\chi(e)$ is shown in the figure.

There is an interesting characteristic feature: The cross sections of the resonant rings in weakly oblate galaxies are radially extended, while the cross sections of the arms in galaxies whose oblateness exceeds the critical value e_{cr} are extended along the Ox_3 axis. The value of e_{cr} is determined by equation (29) for $\chi = 1$. For NGC 7020, we obtained $e_{cr} \approx 0.88$, which is very close to the mean eccentricity $e \approx 0.89$ of the isophotes in the galaxy itself. Consequently, in the resonance model under consideration, the ring of NGC 7020 has an approximately circular cross section.

6. SMALL PERTURBATIONS OF THE ARM

Let the elliptical cross section of the arm (1) at each time be deformed into a slightly different ellipse by the linear transformation

$$\begin{aligned} \delta\xi &= a\xi + bx_3, \\ \delta x_3 &= c\xi + dx_3, \end{aligned} \tag{32}$$

where the functions of time $a(t)$, $b(t)$, $c(t)$, and $d(t)$ [whose specific form is given by (45)] are small enough that we can neglect their squares in the subsequent analysis. The symmetric part of transformations (32)

$$\delta_1\xi = a\xi, \quad \delta_1 x_3 = dx_3 \tag{33}$$

obviously leads to changes in the semi-axes $a_1 \longrightarrow a_1(1 + a)$ and $a_3 \longrightarrow a_3(1 + d)$ and, consequently, in the density ρ.

We can easily find the new coefficients of the inner potential of the elliptical arm. It is obvious that

$$\alpha_1 = 2\pi G\rho \frac{a_3}{a_1 + a_3}\left[1 - a - \frac{aa_1 + da_3}{a_1 + a_3}\right];$$

i.e., the increment in the first coefficient is

$$\delta\alpha_1 = -2\pi G\rho \frac{a_3}{a_1 + a_3}\left(a + \frac{aa_1 + da_3}{a_1 + a_3}\right).$$

In the same way, we find

$$\delta\alpha_3 = -2\pi G\rho \frac{a_1}{a_1 + a_3}\left(d + \frac{aa_1 + da_3}{a_1 + a_3}\right).$$

On the other hand, the antisymmetric part of transformations (32)

$$\delta_2 x_3 = bx_3, \quad \delta_2 x_3 = c\xi \tag{34}$$

leads to rotation of the arm through a small angle θ and a trivial shift of the particles along the elliptical cross section of the orbits. Indeed,

$$\begin{aligned} \delta_2 x_3 &= c\xi = \theta\xi - \varepsilon a_3^2\xi, \\ \delta_2\xi &= bx_3 = -\theta x_3 + \varepsilon a_1^2 x_3, \end{aligned} \tag{35}$$

where θ is just the small angle of the arm rotation:

$$\theta = \frac{a_1^2 c + a_3^2 b}{a_1^2 - a_3^2}.$$

7. PERTURBATION OF THE POTENTIAL

The potential of the unperturbed elliptical arm is given above by formula (2). A shift along the ellipse obviously does not affect the arm potential. Therefore, we obtain

$$\tilde{\varphi} = \text{const} - \alpha_1(\xi + \theta x_3)^2 - \alpha_3(x_3 - \theta\xi)^2. \tag{36}$$

The increment in the potential due to the antisymmetric part of transformations (35) is equal to

$$\delta_2\tilde{\varphi} = 4\pi G\rho\frac{a_1^2c + a_3^2b}{(a_1 + a_3)^2}\xi x_3. \tag{37}$$

Then, the total increment of the potential at the inner point (ξ, x_3) is given by the formula

$$\delta\tilde{\varphi} = -\alpha_1\left(a + \frac{aa_1 + da_3}{a_1 + a_3}\right)\xi^2 - \alpha_3\left(d + \frac{aa_1 + da_3}{a_1 + a_3}\right)x_3^2 + 4\pi G\rho\frac{a_1^2c + a_3^2b}{(a_1 + a_3)^2}\xi x_3. \tag{38}$$

8. MOTION OF A PARTICLE IN THE PERTURBED ARM

Let us now consider the motion of a particle. The equations of its dynamics in the unperturbed potential

$$\Phi = \varphi - \frac{L^2}{2R^2}, \quad R = R_0 + \xi, \tag{39}$$

(where φ is given by formula (7), and L is the integral of angular momentum) will be

$$\frac{d^2\xi}{dt^2} = \frac{\partial\Phi}{\partial\xi}, \quad \frac{d^2x_3}{dt^2} = \frac{\partial\Phi}{\partial x_3}. \tag{40}$$

In the perturbed state,

$$\xi \longrightarrow \xi + \delta\xi, \quad x_3 \longrightarrow x_3 + \delta x_3, \quad \varphi \longrightarrow \varphi + \delta\tilde{\varphi},$$

in place of (40), we obtain the following set of inhomogeneous, ordinary differential equations for the unknown quantities $\delta\xi$ and δx_3:

$$\begin{aligned}\frac{d^2}{dt^2}\delta\xi - \frac{\partial^2\Phi}{\partial\xi^2}\delta\xi - \frac{\partial^2\Phi}{\partial\xi\partial x_3}\delta x_3 &= \frac{\partial}{\partial\xi}\delta\tilde{\varphi},\\ \frac{d^2}{dt^2}\delta x_3 - \frac{\partial^2\Phi}{\partial\xi\partial x_3}\delta\xi - \frac{\partial^2\Phi}{\partial x_3^2}\delta x_3 &= \frac{\partial}{\partial x_3}\delta\tilde{\varphi},\end{aligned} \tag{41}$$

where $\delta\tilde{\varphi}$ is given by formula (38). For the reduced potential

$$\Phi = \varphi - \frac{L^2}{2R_0^2\left(1 + \frac{\xi}{R_0}\right)^2}, \tag{42}$$

we obtain with the required accuracy the expression

$$\Phi = \text{const} - \Omega_c R_0\xi - (A_1 + \alpha_1)\xi^2 - (A_3 + \alpha_3)x_3^2 - \frac{L^2}{2R_0^2}\left(1 - 2\frac{\xi}{R_0} + 3\frac{\xi^2}{R_0^2}\right). \tag{43}$$

Consequently, equations (42) reduce to the form

$$\begin{aligned}\frac{d^2}{dt^2}\delta\xi + \omega_1^2\delta\xi &= -2\alpha_1\left(a + \frac{aa_1 + da_3}{a_1 + a_3}\right)\xi + 4\pi G\rho\frac{a_1^2c + a_3^2b}{(a_1 + a_3)^2}x_3,\\ \frac{d^2}{dt^2}\delta x_3 + \omega_1^2\delta x_3 &= -2\alpha_3\left(d + \frac{aa_1 + da_3}{a_1 + a_3}\right)x_3 + 4\pi G\rho\frac{a_1^2c + a_3^2b}{(a_1 + a_3)^2}\xi.\end{aligned} \tag{44}$$

9. THE DISPERSION EQUATION

The unperturbed solutions $\xi(t)$ and $x_3(t)$ from (23), as well as the time dependences for the coefficients

$$\begin{aligned}a &= a_0e^{i\omega t}, \quad c = c_0e^{i\omega t},\\ b &= b_0e^{i\omega t}, \quad d = d_0e^{i\omega t}\end{aligned} \tag{45}$$

(where ω is the frequency of small oscillations of the perturbed arm), must be substituted into the right-hand sides of equations (44). In addition,

$$\begin{aligned}\delta\xi &= [a_0\xi(t) + b_0x_3(t)]e^{i\omega t},\\ \delta x_3 &= [c_0\xi(t) + d_0x_3(t)]e^{i\omega t},\end{aligned} \tag{46}$$

[where $\xi(t)$ and $x_3(t)$ are also taken from (23)] must be substituted for $\delta\xi$ and δx_3 on the left-hand sides of the above equations. After these substitutions into (44) and calculation of the second derivatives of functions (46), the system (44) can be reduced after extensive manipulation to the equations

$$\begin{aligned}&Q_1(a_0, b_0, d_0)\cos(\omega_1t + k_1)\\ &+ Q_2(a_0, b_0, c_0)\sin(\omega_1t + k_1) = 0,\\ &Q_3(b_0, c_0, d_0)\cos(\omega_1t + k_1)\\ &+ Q_4(a_0, c_0, d_0)\sin(\omega_1t + k_1) = 0.\end{aligned} \tag{47}$$

Here,

$$Q_1 = a_0C_1\left[-\omega^2 + 2\alpha_1\left(1 + \frac{a_1}{a_1 + a_3}\right)\right] + b_0C_3[2i\omega\omega_1] + d_0C_1\left[2\alpha_1\frac{a_3}{a_1 + a_3}\right],$$

$$Q_2 = a_0C_1[-2i\omega\omega_1] + b_0C_3\left[-\omega^2 - 4\pi G\rho\frac{a_3^2}{(a_1 + a_3)^2}\right]$$

Solutions of the dispersion equation

e	χ	ω_1^2	ω_2^2	ω_3^2
0.25	0.029431	5.341189	5.133680	−0.176781
0.5	0.139000	5.442480	5.005362	−0.140321
0.75	0.461141	5.439000	4.615930	−0.078983
0.85	0.810901	5.224364	4.292386	−0.060398
0.88	0.998620	5.091055	4.151278	−0.060223
0.90	1.169900	4.970489	4.037862	−0.063190
0.95	1.995270	4.467905	3.633548	−0.093558

$$+ c_0C_3\left[-4\pi G\rho\frac{a_1^2}{(a_1+a_3)^2}\right], \quad (48)$$

$$Q_3 = b_0C_1\left[-4\pi G\rho\frac{a_3^2}{(a_1+a_3)^2}\right]$$

$$+ c_0C_1\left[-\omega^2 - 4\pi G\rho\frac{a_1^2}{(a_1+a_3)^2}\right] + d_0C_3[2i\omega\omega_1],$$

$$Q_4 = a_0C_3\left[2\alpha_3\frac{a_1}{a_1+a_3}\right]$$

$$+ c_0C_1[-2i\omega\omega_1] + d_0C_3\left[-\omega^2 + 2\alpha_3\left(1+\frac{a_3}{a_1+a_3}\right)\right].$$

Since equations (47) must be satisfied at any instant of time t, we impose the requirement

$$Q_1 = Q_2 = Q_3 = Q_4 = 0. \quad (49)$$

Equality (49) represents a system of four linear algebraic equations for the unknown quantities a_0, b_0, c_0, and d_0. Since the right-hand sides of these equations are equal to zero, they have nontrivial solutions only if the determinant of this system is equal to zero. This condition yields the basic dispersion equation of the problem:

$$\omega^2(\omega^6 + K_1\omega^4 + K_2\omega^2 + K_0) = 0 \quad (50)$$

with the coefficients

$$K_1 = \gamma_2 + \gamma_3 - \gamma_1 - \gamma_4 - 8\omega_1^2;$$

$$K_2 = 16\omega_1^4 - 4\omega_1^2(\gamma_2 + \gamma_3 - \gamma_1 - \gamma_4)$$

$$+ \gamma_1\gamma_4 - \gamma_2\gamma_3 - (\gamma_1 + \gamma_4)(\gamma_2 + \gamma_3); \quad (51)$$

$$K_0 = 4\omega_1^2(\gamma_1\gamma_2 + \gamma_3\gamma_4 - 2\gamma_2\gamma_3)$$
$$+ (\gamma_2 + \gamma_3)(\gamma_1\gamma_4 - \gamma_2\gamma_3).$$

Here, we have introduced the notation

$$\gamma_1 = \frac{\chi(2+\chi)}{(1+\chi)^2}, \quad \gamma_2 = \frac{\chi^2}{(1+\chi)^2}, \quad \gamma_3 = \frac{1}{(1+\chi)^2}, \quad (52)$$
$$\gamma_4 = \frac{2\chi+1}{(1+\chi)^2},$$

and $\left(\chi = \frac{a_3}{a_1}\right)$. In addition, ω^2 and ω_1^2 are normalized to $4\pi G\rho$:

$$\omega^2 \equiv \frac{\omega^2}{4\pi G\rho};$$
$$\omega_1^2 = \frac{1}{1+\chi} + \frac{A_3}{4\pi G\rho} = \frac{\chi}{1+\chi} + \frac{3\Omega_c^2}{4\pi G\rho} + \frac{A_1}{4\pi G\rho}. \quad (53)$$

10. ANALYSIS OF THE DISPERSION EQUATION

Since $\omega^2 \neq 0$, the dispersion equation (50) can be reduced to the bicubic equation:

$$\omega^6 + K_1\omega^4 + K_2\omega^2 + K_0 = 0. \quad (54)$$

We calculated the coefficients of this equation for the same parameters β and $R/\tilde{a}_1$ as in the figure. Solutions of equation (54) for several values of e are presented in the table.

We can see that there are two positive and one negative square of the frequency at each value of e. This implies the existence of imaginary frequencies and, therefore, the instability of the stellar orbits in the arm around the galaxy. We can also see that the absolute value of the negative square of the frequency is small everywhere. Consequently, the instability increment of the stellar orbits is also a small quantity.

11. CONCLUSION

As can be seen in the figure, the most interesting consequence of our assumption that the frequencies of stellar oscillations in an equilibrium ring have a resonant character is that the shape of the ring cross section depends on the oblateness of the spheroidal galaxy itself. In the framework of the model considered, rings whose cross sections vary from flat to circular and further to prolate in the direction perpendicular to the symmetry plane of the galaxy are possible from the dynamical point of view. In particular, the ring in the galaxy NGC 7020 should have an approximately circular arm cross section in the case of the 1 : 1 resonance. We have studied the stability of rings in the general case of linear affine perturbations. Our solution of the dispersion equation for NGC 7020 shows that orbits in the ring will be slightly unstable. We conclude that the stellar orbits in the ring of this galaxy will drift from the 1 : 1 resonance, and the ring will slowly evolve as a whole.

REFERENCES

1. S. N. Nuritdinov and M. V. Usarova, *Problems in the Physics and Dynamics of Stellar Systems* (Tashkent, 1989), p. 49.
2. R. Buta, Astrophys. J. **370**, 130 (1991).
3. B. A. Vorontsov-Vel'yaminov, Astron. Zh. **37**, 381 (1960).
4. B. A. Vorontsov-Vel'yaminov, *Extragalactic Astronomy* (Nauka, Moscow, 1978).
5. C.-Y. Wong, Astrophys. J. **190**, 675 (1974).
6. V. A. Antonov and S. N. Nuritdinov, Astrofizika **19**, 547 (1983).
7. H. Alfven and G. Arrenius, *Evolution of the Solar System* (NASA, Washington, 1979).
8. B. P. Kondrat'ev, Astron. Zh. **74**, 845 (1997).
9. R. Buta, Astrophys. J. **356**, 87 (1990).
10. S. Chandrasekhar, *Principles of Stellar Dynamics* (Univ. Chicago Press, Chicago, 1942; Inostrannaya Literatura, Moscow, 1948).
11. A. S. Bakaĭ and Yu. P. Stepanovskiĭ, *Adiabatic Invariants* (Naukova Dumka, Kiev, 1981).
12. B. P. Kondrat'ev, *Dynamics of Ellipsoidal Gravitating Figures* (Nauka, Moscow, 1989).

APPENDIX

Since the ring in NGC 7020 is an inner ring [2], we shall use the formulas for the inner potential of nonuniform stratified ellipsoids from monograph [12], ch. 2, when calculating the quantities appearing in expression (25) for Ψ. In the case under consideration, the layers with constant density are spheroids that are similar to each other. This simplifies the calculations.

First, we must find the derivative

$$\frac{\partial \varphi_g}{\partial R} = -2\pi G \tilde{a}_1^2 \tilde{a}_3 R \int_0^\infty \frac{\rho[m^2(u)]du}{(\tilde{a}_1^2+u)^2\sqrt{\tilde{a}_3^2+u}}. \quad (A.1)$$

By substituting here the density distribution (28) in the form

$$\rho[m^2(u)] = \frac{1}{\left[1+\beta\left(\frac{R^2}{\tilde{a}_1^2+u}+\frac{x_3^2}{\tilde{a}_3^2+u}\right)\right]^{3/2}}, \quad (A.2)$$

we obtain for Ω_c^2 from formula (5)

$$\Omega_c^2 = 2\pi G \tilde{a}_1^2 \tilde{a}_3 \int_0^\infty \frac{du}{(\tilde{a}_1^2+u)^2\sqrt{\tilde{a}_3^2+u}\left[1+\frac{\beta R_0^2}{\tilde{a}_1^2+u}\right]^{3/2}}. \quad (A.3)$$

Finally, Ω_c^2 can be expressed in terms of the incomplete elliptical integrals of the first and second kinds:

$$\Omega_c^2 = \frac{4\pi G}{\beta R_0^2}\sqrt{\frac{1-e^2}{e^2+\beta R_0^2}}[F(\varphi,k)-E(\varphi,k)], \quad (A.4)$$

where

$$\varphi = \arccos\sqrt{\frac{1-e^2}{1+\beta R_0^2}}, \quad k = R_0\sqrt{\frac{\beta}{e^2+\beta R_0^2}}.$$

Next, the second derivative of the potential in the equatorial plane of the galaxy is equal to

$$\left.\frac{\partial^2\varphi_g}{\partial R^2}\right|_{\substack{R=R_0\\ x_3=0}} = -\Omega_c^2 + 6\pi G\tilde{a}_1^2\tilde{a}_3\beta R_0^2 \times\int_0^\infty \frac{du}{[\tilde{a}_1^2+\beta R_0^2+u]^{5/2}\sqrt{(\tilde{a}_1^2+u)(\tilde{a}_3^2+u)}}. \quad (A.5)$$

After the substitution $x = [\tilde{a}_1^2+\beta R_0^2+u]^{-1/2}$ and a series of transformations, we obtain the following expression for $2A_1$ from formula (6):

$$2A_1 = \Omega_c^2 - 4\pi G\sqrt{\frac{1-e^2}{e^2+\beta R_0^2}} \times\left\{\frac{1}{(1+\beta R_0^2)^{3/2}}\sqrt{\frac{1-e^2}{e^2+\beta R_0^2}} + \frac{(2+k^2)F(\varphi,k)-2(1+k^2)E(\varphi,k)}{\beta R_0^2}\right\}. \quad (A.6)$$

In the same way, after quite simple but cumbersome calculations, we obtain

$$2A_3 = \frac{4\pi G}{e^2+\beta R_0^2} \times\left\{\frac{1}{\sqrt{1+\beta R_0^2}} + \sqrt{\frac{1-e^2}{e^2+\beta R_0^2}}[F(\varphi,k)-2E(\varphi,k)]\right\}. \quad (A.7)$$

Substituting expressions (A.4), (A.6), and (A.7) into (25), we finally obtain the required formula (31).

Translated by Yu. Dumin

Astronomy Reports, Vol. 44, No. 5, 2000, pp. 286–297. Translated from Astronomicheskiĭ Zhurnal, Vol. 77, No. 5, 2000, pp. 331–344.

Physical Conditions in Steep-Spectrum Radio Sources

S. A. Tyul'bashev[1] and P. A. Chernikov[2]

[1]*Pushchino Radio Astronomy Observatory, Astro Space Center, Lebedev Institute of Physics, Leninskiĭ pr. 53, Moscow, 117924 Russia*

[2]*Sternberg Astronomical Institute, Universitetskiĭ pr. 13, Moscow, 119899 Russia*

Received July 22, 1998

Abstract—Interplanetary scintillation observations of the radio sources 4C 31.04, 3C 67, 4C 34.07, 4C 34.09, OE 131, 3C 93.1, OF 247, 3C 147, 3C 173, OI 407, 4C 68.08, 3C186, 3C 190, 3C 191, 3C 213.1, 3C 216, 3C 237, 3C 241, 4C 14.41, 3C 258, and 3C 266 have been carried out at 102 MHz. Scintillations were detected for nearly all the sources. The integrated flux densities and flux densities of the scintillating components are estimated. Nine of the 21 sources have a low-frequency turnover in their spectra; three of the sources have high-frequency turnovers. The physical parameters are estimated for sources with turnovers in the spectra of their compact components. In most of the quasars, the relativistic-plasma energy exceeds the magnetic-field energy, while the opposite is true of most of the radio galaxies. Empirical relations between the size of the compact radio source and its magnetic field and relativistic-electron density are derived. © *2000 MAIK "Nauka/Interperiodica".*

1. INTRODUCTION

Observations at 2.7 GHz [1, 2] have shown that about 30% of strong radio sources have angular sizes less than 2″ and steep spectra. Thus, there exists a special sample of compact radio sources with steep spectra above 1 GHz. These sources have been actively studied with high angular resolution and high sensitivity at centimeter and decimeter wavelengths, while observations at meter wavelengths are virtually absent. We decided to conduct meter-wavelength interplanetary-scintillation observations of these compact steep-spectrum (CSS) radio sources in order to acquire a better understanding of their nature. The basis for these observations was the sample of 62 CSS sources published in [3].

We presented results for 12 sources in [4], our first paper in this cycle. We took primarily strong sources from the initial sample, for which there were abundant high-frequency observations. This enabled us to construct the spectra of compact ($< 0.1''$) features. The spectra for the compact features of all 12 sources had low-frequency turnovers. Assuming that these were the result of synchrotron self-absorption, we obtained estimates of the magnetic field, number density of relativistic electrons, and energies in the magnetic field and in relativistic electrons. In most cases, equipartition of energy between the magnetic field and relativistic particles was violated.

The present paper is the second in this cycle. Our main goal is to study the physical conditions in the compact ($\leq 1''$) features of the CSS sources studied and to search for differences in these physical conditions for the quasars and radio galaxies in the sample.

2. OBSERVATIONS

Our 102-MHz interplanetary-scintillation observations were carried out in 1995–1997 on the Large Phased Antenna (LPA) of the Lebedev Physical Institute. The effective area of the antenna in the zenith direction is 3×10^4 m^2. The receiver time constant is $\tau = 0.4$ s and the receiver bandwidth is about 200 kHz. The rms confusion for the LPA due to extended (non-scintillating) sources is 1 Jy. Here, we present results for 21 sources.

We calibrated the observations using radio sources from the 3C catalog. As a rule, data for no fewer than five calibration sources were recorded in each observing session. All flux-density estimates were obtained using the scale of Kellermann [5]. The observation reduction method is described in [6, 7]. The method used enables the detection of weak scintillating sources whose scintillation dispersions are smaller than the noise dispersion.

We present a detailed description of the results for each source. As a rule, the sources have complex structures, and our observations separate out the main component (or components) contributing to the scintillations. Unless otherwise indicated, scintillations were reliably detected. Unfortunately, we are not able to publish all the spectra (they are accessible in [8]); therefore, the spectra were divided into groups with characteristic behaviors.

4C 31.04

4C 31.04 is a radio galaxy with redshift $z = 0.059$. Observations at 327 MHz with resolution $0.064'' \times 0.041''$ [9] showed that it has a double structure with

1063-7729/00/4405-0286$20.00

separation 0.07″ in the southeast–northwest direction. Both components make roughly equal contributions to the scintillations at 102 MHz, since their flux densities differ by less than a factor of two and they are both equally compact (0.03″ × 0.02″ for the southeast component and 0.043″ × 0.024″ for the northwest component). 1.5-GHz observations with resolution ~1″ and ~7′ [9, 10] show an extended (~2″) halo whose flux density is less than 6% of the total flux density.

We observed 4C 31.04 over four days at elongations ~26°. Strong scintillations were recorded. Taking into account the angular size of the source and its elongation, we estimate the flux density of the scintillating component to be S_{scin} = 2.6 Jy. We estimate the integrated flux density to be S_{int} = 4.7 Jy. The integrated spectrum of the source (Fig. 1) shows a clear flattening toward lower frequencies; given the large errors in the flux density due to the effect of confusion, there may even be a turnover in the integrated spectrum. The spectrum of the compact radio emission also has a maximum near 200 MHz and a turnover at lower frequencies. Note that, in connection with the small number of observations with high angular resolution (~0.01″), the inferred spectrum of the compact emission corresponds to the sum of the flux densities of both compact components. In this case, the turnover in the spectrum could reflect a turnover in the spectrum of either one or both components.

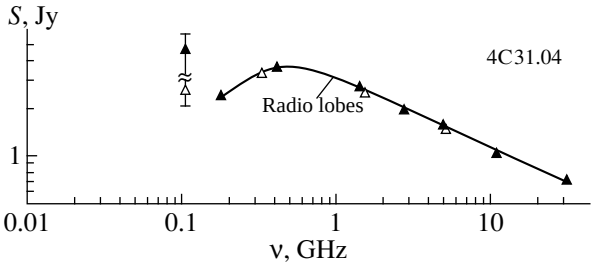

Fig. 1. Integrated spectrum of 4C 31.04 (filled triangles) based on points at 31.4 GHz (0.71 Jy) [11], 10.7 GHz (1.03 Jy) [12], 4.85 GHz (1.57 Jy) [13], 2.7 GHz (1.93 Jy) [14], 1.4 GHz (2.68 Jy) [15], 0.408 GHz (3.6 Jy) [15], 0.178 GHz (2.4 Jy) [16], and 0.102 GHz (4.7 Jy) [this paper]. Spectrum for the compact (scintillating) component (hollow triangles) based on points at 5 GHz (1.48 Jy) [10], 1.5 GHz (2.46 Jy) [10], 0.327 GHz (3.3 Jy) [9], and 0.102 GHz (2.6 Jy) [this paper].

3C 67

This source is a radio galaxy with redshift z = 0.31. The radio source is double, with northern and southern components separated by 2.4″. The southern component contributes about 60% of the total flux at 1.6 GHz [3]. At 0.6 GHz, the northern component is only half as strong as the southern component and is twice as large. This suggests that the contribution of the southern component will dominate at 102 MHz. This component is 0.06″ × 0.02″ in size and is surrounded by a diffuse halo. The flux density of the halo is about 80% of the flux density of the southern component at 1.6 GHz [17]. 0.6-GHz observations with resolution ~0.1″ [18] yield a size for the halo of 0.09″ × 0.09″. We adopted this size for the characteristic size of the source. The optical object that has been identified with the radio source coincides with the southern component, which is probably the radio core.

3C 67 was observed over five days at elongations ~30°. We estimate the flux density of the scintillating component to be S_{scin} = 5.2 Jy, and the integrated flux density to be S_{int} = 14.6 Jy. The integrated spectrum of 3C 67 and the spectrum of its southern component do not show a low-frequency turnover.

4C 34.07

The redshift of 4C 34.07 is unknown, though optical observations suggest that it is probably a quasar [3]. Observations at 1.66, 5, and 15 GHz with resolution ~0.1″ [19] show that it is a very compact source surrounded by an extended halo. The halo contributes about 2% of the integrated flux density at 5 GHz and about 20% of the integrated flux density at 1.67 GHz. Since the halo is rather large (~2″ at 1.67 GHz [19]), we do not expect it to make a significant contribution to scintillations at 102 MHz. 1.67-GHz observations with resolution ~0.01″ [20] indicate that more than 50% of the total flux density at this frequency is associated with a component 0.006″ × 0.003″ in size. We expect that precisely this component will dominate the scintillations at 102 MHz.

We observed 4C 34.07 over three days at elongations near 33°. There were large variations in the flux density from day to day (ΔS = 1.4 – 2.4). This may be due to the small angular size of the scintillating radio source. We estimate S_{scin} = 2.2 Jy. The integrated spectrum shows some steepening at low frequencies (S_{int} = 6 Jy). This overestimation of the integrated flux density is probably the result of confusion. The spectrum of the scintillating radio source has a maximum at 300–500 MHz and turnover at lower frequencies (similar to the spectrum in Fig. 1).

4C 34.09

This source is a radio galaxy with redshift z = 0.020. 5-GHz observations with resolution 0.4″ [3] show that the source has two components separated by 1.1″ in the southeast–northwest direction. 1.6-GHz observations with resolution 0.08″ [3] confirm that the source has two main components surrounded by a weak halo. The halo is large (~3″) and extended in the southeast–northwest direction. Its contribution to the 102-MHz scintillation is insignificant. The southeast component contributes ~80% of the integrated flux density at 1.6 GHz, and we expect that this same feature will dominate the 102-MHz scintillations. Its angular size is 0.15″ × 0.075″.

We observed 4C 34.09 over three days at elongations ~40°. We estimate S_{scin} = 3.8 Jy and S_{int} = 11 Jy.

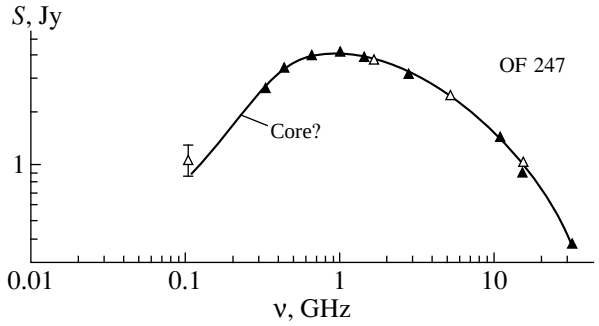

Fig. 2. Integrated spectrum of OF 247 (filled triangles) based on points at 31.4 GHz (0.38 Jy) [11], 15 GHz (0.92 Jy) [25], 10.7 GHz (1.44 Jy) [15], 5 GHz (2.47 Jy) [15], 2.7 GHz (3.18 Jy) [15], 1.41 GHz (3.89 Jy) [15], 0.960 GHz (4.2 Jy) [15], 0.635 GHz (3.96 Jy) [15], 0.430 GHz (3.42 Jy) [15], and 0.318 GHz (2.65 Jy) [15]. Spectrum for the compact (scintillating) component (hollow triangles) based on points at 15 GHz (1.06 Jy) [19], 5 GHz (2.34 Jy) [19], 1.6 GHz (3.77 Jy) [19], and 0.102 GHz (1.1 Jy) [this paper].

The integrated spectrum clearly steepens at low frequencies, probably due to confusion. The spectrum of the scintillating component does not show a low-frequency turnover.

OE 131

Not much information about OE 131 is available. Its optical counterpart has been identified with a quasar with redshift $z = 2.67$. Observations at 5 and 1.66 GHz [20, 21] revealed several components with sizes ~ 0.001″; however, most (60%) of the flux density at this frequency is from a compact region $0.0012'' \times 0.0002''$ in size. There is no significant halo component of OE 131 at least to 1 GHz.

We observed OE 131 over six days at elongations 23° and 32°. There were large jumps in the measured flux-density fluctuations, $\Delta S = 0.35$–1.3 Jy. This may be due to the small angular size of the compact radio emitting region. We estimate $S_{scin} = 0.8$ Jy and $S_{int} = 3.6$ Jy. The spectrum of the scintillating component has a maximum near 400 MHz and a turnover at lower frequencies (similar to the spectrum in Fig. 1).

3C 93.1

This source is a radio galaxy with redshift $z = 0.244$. Observations at 1.67 and 5 GHz with resolution ~0.1″ [19, 22, 23] show a compact component with characteristic angular size $0.3'' \times 0.2''$ and a weak extended halo, whose contribution to the scintillations at 102 MHz will be negligible. 1.67-GHz observations with resolution ~0.01″ [20] indicate that ~70% of the emission at this frequency comes from a compact region $0.19'' \times 0.19''$ in size. This region should also dominate the 102-MHz scintillations.

We observed 3C 93.1 over three days at elongations ~31°. We estimate $S_{scin} = 3.9$ Jy and $S_{int} = 11$ Jy. The radio spectrum is flat.

OF 247

This source is a radio galaxy with redshift $z = 0.219$. It was unresolved in observations at 1.67, 5, and 15 GHz with resolution ~0.1″ [19], so that it is very compact. 1.67-GHz observations with resolution ~0.01″ [24] indicate that the structure of OF 247 is asymmetric and that there is weak emission from a region to the northeast. The characteristic angular size of the source indicated by the radio contours in [24] is $0.02'' \times 0.01''$.

We observed OF 247 over three days at elongations ~35°. We estimate $S_{scin} = 1.1$ Jy; we were not able to measure the integrated flux density. Figure 2 presents the spectrum of OF 247. The general appearance of the spectrum indicates that the role of the weak halo should be completely negligible, even at the lowest frequencies. The spectrum has a peak at 1 GHz and a turnover at lower frequencies. Therefore, OF 247 is more aptly classified as a GHz-peaked-spectrum (GPS) source rather than a CSS source.

3C 147

This is a quasar with redshift $z = 0.545$. Observations at 22.5, 15, 8.4, 5, and 1.6 GHz with resolution ~0.1″ [19, 22, 26–29] show a weak, extended component to the north and a stronger, more compact structure to the south, stretching 0.25″ from northwest to southeast. Observations with resolution ~0.02″ [30–34] indicate that the souther component has a core–jet structure surrounded by a weak halo. The core, which is at the southern end of the jet, is very compact ($\approx 0.005'' \times 0.002''$) and contributes most of the flux density from compact emission at 1.67 GHz [34]. Superluminal expansion has been observed in the core [35]. A comparison of the core and jet at 1.67 GHz, 609 MHz, and 329 MHz [32] showed that the shape and size of the jet are the same at these three frequencies, but its relative contribution to the total flux changes. At 1.67 GHz, the core contributes most of the compact flux density, while the flux densities from the core and the two knots dominating the jet emission are comparable at 329 MHz. Unfortunately, many papers dealing with high-resolution observations do not present estimates for the flux densities of individual features, forcing us to estimate these flux densities from the radio maps presented.

We observed 3C 147 over six days at elongations ~29°. This is the strongest source in our sample, both in terms of its integrated flux density ($S_{int} = 84$ Jy) and the flux density of the scintillating component ($S_{scin} = 39$ Jy, for $\theta \approx 0.2''$). Figure 3 presents an example of a recording for 3C 147. The scintillations are clearly visible, even in the sidelobes of the antenna. There is an appreciable turnover in the integrated spectrum, due to a turnover in the spectrum of the compact features. How-

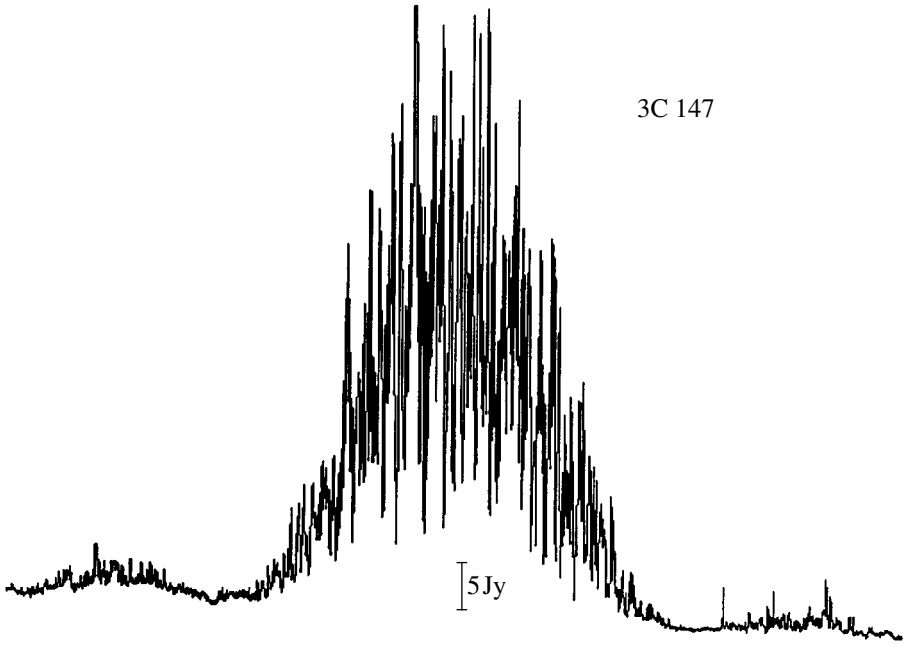

Fig. 3. Analog recording of strong scintillations from 3C 147.

ever, we were not able to construct a trustworthy spectrum including our measurement. It appears that this is one of relatively few cases in which the components dominating the scintillations are negligible at high frequencies. Therefore, we used the spectrum presented in [32] to estimate the physical conditions in this source.

3C 173

This source is a radio galaxy with redshift $z = 1.035$. 1.67-GHz observations with resolution 0.1″ [19] show that it has a double structure with separation 2″ in the northeast–southwest direction. The northeast component is an extended (~0.7″) region of low surface brightness and contributes ~10% of the total flux density at 5 GHz [23]. Thus, we expect the 102-MHz scintillations to be dominated by the southwest component, which has angular size $0.2'' \times 0.1''$.

We observed 3C 173 over three days at elongations ~30°. We estimate $S_{scin} = 4$ Jy and $S_{int} = 18$ Jy. A modest flattening can be seen in the spectrum of the compact component (Fig. 4). However, there is an evident flattening of the integrated spectrum at 38 MHz, suggesting there is a turnover in the spectrum of the compact component near 38 MHz.

OI 407

The redshift of this radio source is unknown; optical observations indicate that it is probably a quasar [3]. The source was essentially unresolved in 5-GHz observations with resolution ~0.1″ [3]. VLBI observations at 1.6 GHz with resolution 0.007″ [3] show that the source is an east–west double with the components separated by 0.052″. Both components have roughly equal angular sizes of $0.008'' \times 0.004''$ and should probably make comparable contributions to 102-MHz scintillations. A comparison of the integrated flux densities at 1.4 GHz (resolution ~10″, 1.57 Jy [39]) and 1.67 GHz (resolution 0.007″, 1.37 Jy [3]) indicate that ~90% of

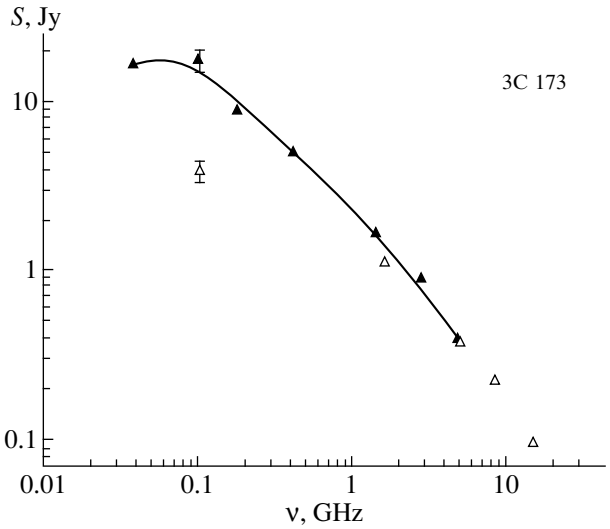

Fig. 4. Integrated spectrum of 3C 173 (filled triangles) based on points at 4.85 GHz (0.4 Jy) [13], 1.4 GHz (1.666 Jy) [36], 0.408 GHz (5.01 Jy) [37], 0.178 GHz (9 Jy) [16], 0.102 GHz (18 Jy) [this paper], and 0.038 GHz (17 Jy) [38]. Spectrum for the compact (scintillating) component (hollow triangles) based on points at 15 GHz (0.098 Jy) [29], 8.4 GHz (0.223 Jy) [29], 5 GHz (0.373 Jy) [23], 1.6 GHz (1.14 Jy) [19], and 0.102 GHz (4 Jy) [this paper].

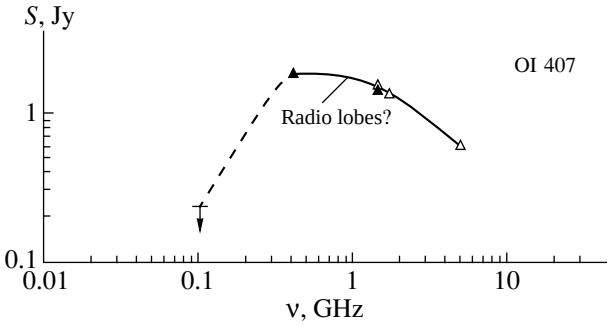

Fig. 5. Integrated spectrum of OI 407 (filled triangles) based on points at 4.85 GHz (0.625 Jy) [13], 1.4 GHz (1.44 Jy) [36], and 0.408 GHz (1.9 Jy) [37]. Spectrum for the compact (scintillating) component (hollow triangles) based on points at 5 GHz (0.61 Jy) [2], 1.67 GHz (1.37 Jy) [3], 1.4 GHz (1.568 Jy) [39], and 0.102 GHz (0.25 Jy; upper limit) [this paper].

the emission is from compact components, and the contribution of halo emission is negligible.

We observed OI 407 over five days at elongations ~31°. No scintillations were detected. The extended component was also not detected. We estimate the upper limit $S_{scin} \leq 0.25$ Jy. Figure 5 shows the spectrum, which has a maximum at 300–500 MHz and a rather sharp turnover at lower frequencies ($\alpha \approx -1.5$, where $S \sim \nu^{-\alpha}$).

4C 68.08

This is a quasar with redshift $z = 1.139$. 1.67-GHz observations with resolution 0.08″ [3] show that the source has a triple structure oriented in the southeast–northwest direction. The central component includes several features, the brightest and most compact of which is probably the core. Two extended (~0.6″) regions of emission are located 0.4″ to the northwest and southeast of the central component. The northwest component contributes ~65% of the total flux density at 1.67 GHz, and we expect this component to dominate in 102-MHz scintillations. Most of the energy flux from this region is contributed by a component with angular size $0.17'' \times 0.10''$.

We observed 4C 68.08 over two days at elongation 47°. Due to the large elongation, it was necessary to make large corrections in order to estimate the flux density of the scintillating source. If $\Delta S = 0.6$ Jy, then $S_{scin} = 1.5$ Jy. We estimate $S_{int} = 3$ Jy. We were unable to construct an accurate spectrum using our measurements. However, in our view, it is unlikely that there is a low-frequency turnover in the spectrum of the compact emission.

3C 186

This source is a quasar with redshift $z = 1.063$. In low-resolution images (~1″), it has two components lying in the southeast–northwest direction [29]. However, higher resolution observations show a more complex structure [18, 28, 29, 40, 41]. The brightest component at 15 GHz, which has been identified as the core [40], is absent from a 0.6-GHz image [18], suggesting the presence of synchrotron self-absorption [28]. Observations with higher resolution reveal additional components. Three components are visible in images with resolution ~0.1″ ($\nu = 15$ GHz) [40], while six components can be distinguished in 1.6-GHz images with resolution ~0.025″ [41]. Considering all the available radio observations, the radio source has an S-shaped structure with the core at the center; the core flux density is negligible at frequencies below 1 GHz. There is a jet consisting of a number of weak knots leading to a radio lobe to the northwest. There is no jet visible to the southeast, though the southeast lobe has a compact hot spot (~0.03″). All the observed components are compact and should therefore scintillate at 102 MHz. However, the lowest frequency ($\nu = 609$ MHz) observations indicate that 2/3 of the energy in compact components is emitted by the southeast lobe and its hot spot [18]. Thus, we expect the contribution of the southeast lobe ($\theta = 0.2'' \times 0.04''$) and its hot spot ($\theta = 0.05'' \times 0.015''$) to dominate in 102-MHz scintillations.

We observed 3C 186 over four days at elongations ≈37°. Averaging over the days of observations yielded an estimate of the integrated flux density $S_{int} = 33$ Jy, while averaging of the observations of flux-density fluctuations with allowance for the angular size and elongation of 3C 186 yielded an estimate of the flux density for the scintillating radio source $S_{scin} = 7.7$ Jy. The spectrum of the southeast lobe and hot spot remains steep to 102 MHz. At the same time, the spectrum of the northwest lobe and jet has a maximum near 1.5 GHz and a turnover at lower frequencies (Fig. 6).

3C 190

This is a quasar with redshift $z = 1.197$. Observations at 15, 5, and 1.6 GHz with angular resolution ~0.2″ [22, 28, 41] show four components extending roughly 3″ in the southwest–northeast direction. There is also a weak, diffuse halo surrounding this structure. 609-MHz observations with comparable resolution [18] only detect three of the components visible at higher frequencies. The angular size of the 609-MHz components (~0.3″) are in agreement with those for the corresponding components detected at the higher frequencies. Nan *et al.* [18] suggest that there is a low-frequency turnover in the spectrum of the component that was not detected at 609 MHz, which is probably the core ($0.03'' \times 0.017''$ at 1.66 GHz) [41]. The coordinates of this component are also closest to those of the optical quasar [22]. The spectra of the remaining three components are steep ($\alpha \sim 1$), and their expected 102-MHz flux is 6 Jy. Due to their small sizes, all three of these components should scintillate, so that the observed

102-MHz scintillations should correspond to the sum of their flux densities.

We observed 3C 190 over four days (in the middle of June 1996) at elongations near 40°. The source showed appreciable scintillation, and $\Delta S \approx 2$ Jy. However, as noted above, these scintillations probably correspond to all three compact components. Taking into account the direction of the solar wind, the component sizes, and the elongation, we obtained the crude estimate $S_{scin} = 2$ Jy. We estimate $S_{int} = 24.5$ Jy. The spectrum of the core turns over at low frequencies, as noted in [18]. The spectra of the three remaining components essentially merge due to their similar flux densities. Both the integrated spectrum and the spectrum of the compact emission show a clear flattening. There is probably a turnover at lower frequencies (similar to that in Fig. 6).

3C 191

This is a quasar with redshift $z = 1.956$. Few observations with high resolution are available. A north–south triple structure can be seen in images at 15, 8.4, 5, and 1.6 GHz [22, 29, 40]. There is a compact hot spot in the northern component. The central component is a relatively weak core, whose spectrum may be flat, but probably has a maximum near 6–7 GHz and a turnover at lower frequencies. A long (~3″) strongly polarized jet extends to the south of the core [29]. The northern component is ~0.1″–0.15″ in size and should scintillate strongly at 102 MHz. The contribution of the core to the scintillations should be negligible. The southern jet may or may not scintillate, depending on its orientation on the sky relative to the solar wind during the 102-MHz observations.

We observed 3C 191 in the middle of June 1996 at elongation 33°. The effective angular size of the jet was ~1.5″, so that its contribution to the scintillations should have been negligible. Thus, the scintillations were dominated by the northern hot spot. We estimate $S_{scin} = 4.3$ Jy and $S_{int} = 23$ Jy. The integrated spectrum remains steep to the lowest frequencies. There is a modest flattening in the spectrum of the northern component (similar to the spectrum in Fig. 6).

3C 213.1

This source is a radio galaxy with redshift $z = 0.194$. Observations with resolution as good as ≤0.2″ are few in number and reveal a complex structure [19, 23, 29]. Observations with resolution ~1″ show two large, diffuse regions, in one of which (the northern region) there are compact features [29]. The overall extent of the source is ~30″. 8.4-GHz observations with resolution ~0.2″ show three compact features in the northern component, lying along a line north–south [29]. The maximum distance between these features is 7–8″. The southern compact feature in the northern component is the most powerful and is strongly polarized (to 38%) [29]. The central feature in the northern component is the weakest, is unpolarized (~0.2%), and is probably the core [29]. This feature was not detected in 5- and 1.6-GHz observations [19, 23, 29]. The flux density of the southern feature in the northern component is twice that of the northern feature at 1.6 GHz [19], suggesting that the main contribution to the 102-MHz scintillations should be the southern compact feature. 1.6-GHz observations with resolution ~0.3″ show that this feature is compact ($0.2'' \times 0.2''$) and is submerged in a halo $1.2'' \times 0.7''$ in size.

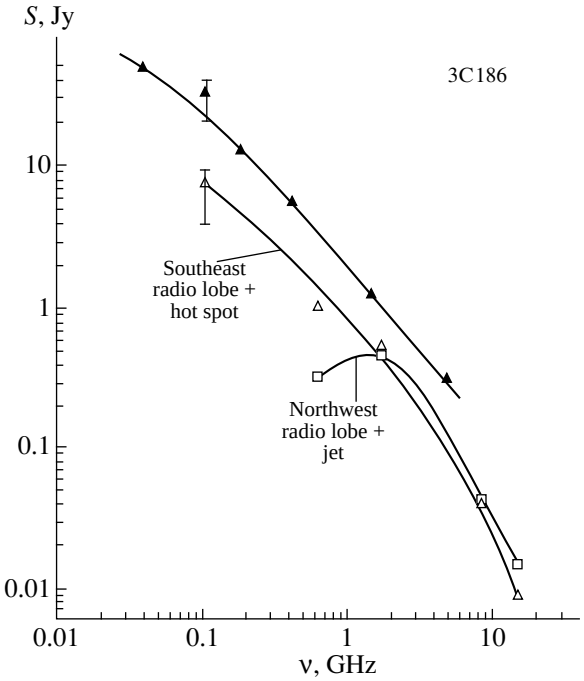

Fig. 6. Integrated spectrum of 3C 186 (filled triangles) based on points at 4.85 GHz (0.308 Jy) [13], 1.4 GHz (1.261 Jy) [36], 0.408 GHz (5.55 Jy) [37], 0.102 GHz (33 Jy) [this paper], and 0.038 GHz (49 Jy) [38]. Spectrum for one compact (scintillating) component (hollow triangles) based on points at 15 GHz (0.009 Jy) [40], 8.4 GHz (0.041 Jy) [29], 1.67 GHz (0.52 Jy) [41], 0.61 GHz (1.019 Jy) [18], and 0.102 GHz (7.7 Jy) [this paper]. Spectrum for the other compact (scintillating) component (hollow squares) based on points at 15 GHz (0.015 Jy) [40], 8.4 GHz (0.042 Jy) [29], 1.67 GHz (0.5 Jy) [41], and 0.61 GHz (0.315 Jy) [18].

We observed 3C 213.1 over four days at elongations near 40°. No scintillations were detected. We estimate an upper limit for $S_{scin} \leq 0.8$ Jy and estimate the integrated flux density to be $S_{int} = 12$ Jy. We are not able to construct an accurate spectrum using our measurements; however, we suggest that it is very likely that there is a low-frequency turnover in the spectrum of the compact emission.

3C 216

This source is a quasar with redshift $z = 0.668$. In low-resolution (~1″) maps, it has an irregular shape ~8″ in size extending from southwest to northeast (see, for example, [28, 29, 42]). In higher resolution (~0.2″) images, three components can be distinguished, whose relative flux densities vary with frequency [18, 22, 28, 29].

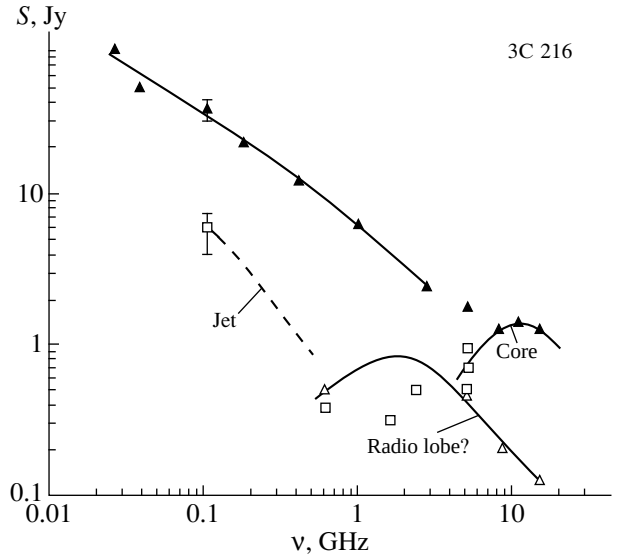

Fig. 7. Integrated spectrum of 3C 216 (filled triangles) based on points at 14.9 GHz (1.27 Jy) [48], 10.695 GHz (1.41 Jy) [49], 8.085 GHz (1.26 Jy) [50], 5 GHz (1.8 Jy) [15], 2.7 GHz (2.45 Jy) [15], 0.968 GHz (6.2 Jy) [15], 0.408 GHz (11.9 Jy) [37], 0.178 GHz (21.54 Jy) [15], 0.102 GHz (36 Jy) [this paper], 0.038 GHz (51 Jy) [38], and 0.026 GHz (89 Jy) [15]. Spectrum of the radio lobe (?) (hollow triangles) based on points at 15 GHz (0.125 Jy) [28], 8.4 GHz (0.204 Jy) [29], 5 GHz (0.45 Jy) [22], 0.6 GHz (0.505 Jy) [18]. Spectrum of the core and jet (?) (hollow squares) based on points at 5 GHz (0.966 Jy) [43], 5 GHz (0.7 Jy) [45], 5 GHz (0.5 Jy) [44], 2.3 GHz (0.5 Jy) [46], 1.6 GHz (0.32 Jy) [47], and 0.6 GHz (0.389 Jy) [18].

The southwest component is extended (>1″) and weak, so that it should contribute to the total flux density at 102 MHz, but should not scintillate. The northeast component is compact (≈0.19″ × 0.035″ [18]) and has a steep spectrum above 5 GHz ($\alpha \approx 1$, see the fluxes in [28, 29, 42]). The spectrum of this component (Fig. 7) has a maximum near 2 GHz and turns over at lower frequencies. The central component, in turn, consists of a variable, very compact (~0.1 milliarcsecond [43]) core and ≈0.09″ × 0.05″ jet; superluminal expansion has been observed on milliarcsecond scales [18, 43–47]. It is difficult to measure the spectrum of the core due to its variability. Using observations separated by roughly a year and assuming that the variability will be modest on such time scales (≤10% of the total core flux density), it appears that the core spectrum has a maximum at 10 GHz and turns over at lower frequencies, while the jet spectrum remains steep. The flux densities from the core and jet are approximately equal at 5 GHz [22, 44]. The spectrum constructed (Fig. 7) suggests that the flux density from the core should fall toward lower frequencies, while the expected flux density from the jet rises. Thus, we expect the jet to make the dominant contribution to 102-MHz scintillation observations.

We observed 3C 216 over two days at elongations ~40°. The quality of the observations was high. Large fluctuations of the flux density ΔS = 3 Jy were recorded. We estimate S_{scin} = 6 Jy and S_{int} = 36 Jy. It is difficult to derive the spectrum of the jet due to uncertainty about separating the core and jet emission in our observations. It is likely that the spectrum of the jet remains steep to 102 MHz. Note also that the spectrum of 3C 216 is the most complex among those considered in this study.

3C 237

This source is a radio galaxy with redshift z = 0.877. The numerous observations of this source at various frequencies with various resolutions indicate that it has an east–west double structure with separation ~1″ [17–19, 22, 28, 29, 51]. Both components have sizes ~0.1″–0.2″, so that they should scintillate at 102 MHz.

We observed 3C 237 over three days at elongations 30–35°. Powerful scintillations were recorded (ΔS = 6.8 Jy). We estimate S_{scin} = 7.4 Jy for each of the components, and S_{int} = 28 Jy. The spectra for the two compact features are very similar. They appear to have maxima at 102 MHz and to turn over at lower frequencies. The integrated spectrum shows a clear flattening at 102 MHz (similar to the spectrum in Fig. 8 below).

3C 241

This source is a radio galaxy with redshift z = 1.617. It is an east–west double with separation ~0.9″ [3, 17–19, 22, 23, 28, 29]. Maps with resolution ~0.1″ show that the western component is made up of two compact (<0.1″) features [3, 17, 18, 23, 28], which should both scintillate at 102 MHz.

We observed 3C 241 over four days at elongations near 35°. The mean value of the flux variations as ΔS = 3 Jy. We estimate S_{scin} = 2.5 Jy for each of the two compact components, and S_{int} = 14.5 Jy. The spectra of the compact features clearly have maxima near 400 MHz and turn over at lower frequencies (Fig. 8). A modest flattening is also apparent in the integrated spectrum.

4C 14.41

Few data are available for this source; its redshift is unknown, but it is expected to be a quasar [3]. The source was unresolved in 1.6-GHz observations with resolution ~1″ [53]. Higher resolution (~0.01″) observations at 1.66 and 0.6 GHz [3, 54] show that the source is double. The components are both compact (~0.01″) and are separated by ~0.08″ in the northwest–southeast direction. We expect both these features to scintillate at 102 MHz.

We observed 4C 14.41 over two days at elongation 21°. In spite of the small fluctuations in the flux density (ΔS = 0.65 Jy), scintillations were clearly detected. We estimate S_{scin} = 0.4 Jy for each of the two components, and S_{int} = 4.5 Jy. The spectra of the scintillating components have obvious low-frequency turnovers (similar to the spectrum in Fig. 8).

3C 258

This is a radio galaxy with redshift $z = 0.165$. Low-resolution (~2″) 5-GHz maps show a bright, unresolved core with jets ~30″ in length extending toward the north and south [55]. The core emits a large fraction of the energy. Higher-resolution (0.08″) 5-GHz observations indicate that the core has two components with similar flux densities separated by ~0.1″ in the southwest–northeast direction [23]. 1.6-GHz observations with resolution 0.007″ show that these components are ~0.01″ in size [3]. Thus, we expect both components to scintillate at 102 MHz.

We observed 3C 258 at the end of September 1997 over two days, in the presence of sharply worsening interference. The observations were of low quality, though scintillations were detected. We estimate S_{scin} = 0.55 Jy and S_{int} = 3.5 Jy. There is no low-frequency turnover in the spectra.

3C 266

This is a radio galaxy with redshift $z = 1.275$. Observations at 8.4, 5, and 1.6 GHz show that it has a double structure with separation 4″ [19, 29, 56]. The northern and southern components have sizes 0.5″ × 0.1″ and 0.7″ × 0.3″, respectively [19]. The flux densities of the components are roughly equal at all frequencies. We therefore expect both components to scintillate at 102 MHz.

We observed 3C 266 over six days. Scintillations were recorded reliably. Given the source elongation (44°), the component separation (4″), and the direction of solar-wind propagation, we estimated the flux density in the compact features and the integrated flux density to be S_{scin} = 4.2 Jy and S_{int} = 19 Jy, respectively. There is no low-frequency turnover in the spectra of the two compact features.

3. PHYSICAL CONDITIONS IN THE CORES OF THE SOURCES STUDIED

Our observations indicate the presence of low-frequency (102 MHz) turnovers in the spectra of the compact components of nine of the 21 radio source investigated. For three sources, there is a turnover at higher frequencies. As discussed in [4], the most probable reason for a low-frequency turnover is synchrotron self-absorption. Artyukh [57] has presented a method for estimating the magnetic field and relativistic plasma density without resorting to the usual assumption of equipartition.

Assuming that the radio emission of the sources studied is synchrotron radiation and that the inferred low-frequency turnovers are the result of synchrotron self-absorption, we have estimated the corresponding physical parameters for all 12 sources with low-frequency turnovers. We adopted H_0= 75 km s^{-1} Mpc^{-1} and q_0 = 1/2 for the calculations. The results are presented in Table 1. The columns give (1) the source name, (2) redshift z, (3) angular size Ω, (4) mean linear size L,

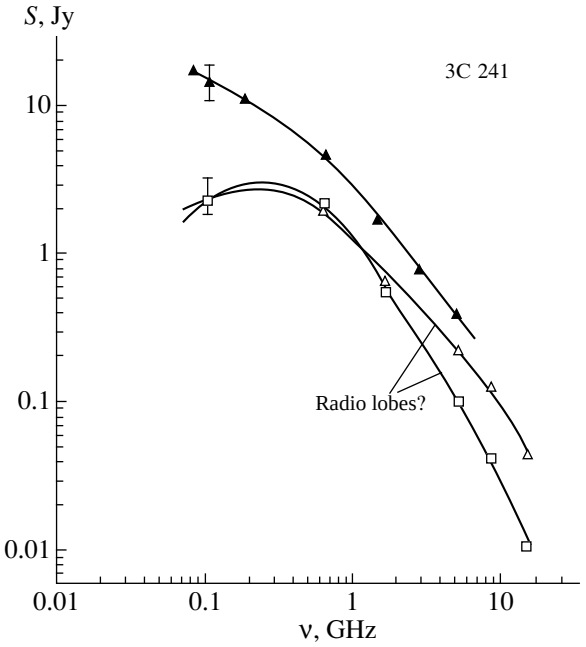

Fig. 8. Integrated spectrum of 3C 241 (filled triangles) based on points at 4.85 GHz (0.388 Jy) [13], 2.7 GHz (0.8 Jy) [52], 1.41 GHz (1.7 Jy) [52], 0.635 GHz (4.8 Jy) [52], 0.178 GHz (11.1 Jy) [52], 0.102 GHz (14 Jy) [this paper], and 0.08 GHz (17 Jy) [52]. Spectrum for one compact (scintillating) component (hollow triangles) based on points at 15 GHz (0.046 Jy) [28], 8.4 GHz (0.124 Jy) [29], 5 GHz (0.22 Jy) [3], 1.6 GHz (0.65 Jy) [3], 0.6 GHz (2 Jy) [18], and 0.102 GHz (2.4 Jy) [this paper]. Spectrum for the other compact (scintillating) component (hollow squares) based on points at 15 GHz (0.011 Jy) [28], 8.4 GHz (0.043 Jy) [29], 5 GHz (0.095 Jy) [3], 1.6 GHz (0.57 Jy) [3], 0.6 GHz (2.2 Jy) [18], and 0.102 GHz (2.4 Jy) [this paper].

(5) spectral indices in the optically thin region of the spectrum α, (6) magnetic-field strength, (7) energy of the magnetic field per cm^3, (8) total magnetic-field energy in the volume L^3, (9) density of relativistic electrons, (10) energy of relativistic electrons per cm^3, and (11) total relativistic-electron energy in the volume L^3. The accuracy of this method is approximately an order of magnitude, or two orders of magnitude if the source angular size is not accurately known [57].

The redshifts of 4C 34.07, OI 407, and 4C 14.41 are unknown, and we have adopted $z = 2$. In the formula used to derive the physical parameters considered, the redshift enters as $(1 + z)^{-1}$, so that the value of z only weakly influences the final result. In the case of 3C 147 and 3C 241, the estimates of the physical parameters are different for different components; the components are marked by letters A and B in Table 1.

We can see from Table 1 that all estimates correspond to linear scales $L \sim 100$ pc, except in the case of 4C 31.04, 4C 34.07, OE 131, and OI 407, where $L \sim 10$ pc. Our results indicate equipartition of energy only for 4C 31.04. The magnetic field varies over a wide range from 10^{-11} to 10^5 G. It is obvious that the existence of fields of 10^5 or 10^4 G on scales of 100 pc is improbable.

Table 1. Estimates of the physical conditions in compact radio sources with steep spectra

Name	z	Ω, arcsec	L, pc	α	$H_\perp$, G	$E_{H_\perp}$, erg cm^{-3}	$E_{H_\perp}$, erg	n_e, cm^{-3}	E_e, erg cm^{-3}	E_e, erg
4C 31.04	0.059	0.03×0.02 $+0.043\times0.024$	20	0.4	10^{-3}	10^{-7}	4×10^{52}	10^{-3}	4×10^{-7}	10^{53}
4C 34.07	2	0.006×0.003	20	0.4	10^{-7}	6×10^{-16}	10^{44}	10^{3}	5×10^{1}	10^{61}
OE 131	2.67	0.0012×0.0002	3	0.5	10^{-10}	6×10^{-22}	3×10^{35}	10^{9}	10^{9}	4×10^{65}
OF 247	0.219	0.02×0.01	50	1.1	6×10^{-2}	10^{-4}	4×10^{56}	4×10^{-3}	7×10^{-8}	10^{53}
3C 147 A	0.545	0.17×0.05	400	1.1	10^{-1}	10^{-3}	6×10^{60}	10^{-6}	10^{-11}	3×10^{52}
3C 147 B	0.545	0.5×0.5	2500	1.3	10^{-3}	10^{-7}	10^{59}	7×10^{-7}	6×10^{-11}	3×10^{55}
OI 407	2	0.008×0.004 $+0.008\times0.004$	30	0.8	6×10^{-5}	10^{-10}	10^{50}	1	10^{-3}	10^{57}
3C 186	1.063	0.224×0.083	500	1.6	10^{4}	4×10^{6}	7×10^{70}	10^{-12}	7×10^{-20}	10^{45}
3C 190	1.197	0.03×0.017	100	0.8	10^{5}	3×10^{8}	10^{70}	5×10^{-12}	10^{-19}	4×10^{42}
3C 213.1	0.194	0.2×0.2	600	0.8	5	1	5×10^{63}	6×10^{-10}	10^{-15}	10^{49}
3C 237	0.877	0.2×0.1	800	1.4	4×10^{-3}	7×10^{-7}	10^{58}	3×10^{-5}	10^{-9}	10^{55}
3C 241 A	1.617	0.1×0.1	600	1.1	10^{-2}	4×10^{-6}	10^{58}	3×10^{-6}	10^{-10}	7×10^{53}
3C 241 B	1.617	0.1×0.1	600	1.6	6×10^{-3}	10^{-6}	7×10^{57}	2×10^{-5}	10^{-9}	5×10^{54}
4C 14.41	2	0.01×0.01	60	0.4	10^{-4}	7×10^{-10}	3×10^{51}	6×10^{-2}	7×10^{-5}	3×10^{56}

It is likely that such results are severely overestimated due to our inadequate knowledge of the source structure. As noted above, we took the angular sizes for components from VLBI observations and assumed that these angular sizes did not depend on frequency. However, in contrast to the situation in [4], where there were numerous VLBI observations for most of the sources studied, many of the sources considered in the present paper have only sparse data on the angular sizes of their components. It is likely that some of the angular sizes we have adopted are only upper limits. The method used to estimate the physical parameters is very sensitive to the source angular size.

Let us consider, for example, the quasar 3C 190. According to [41], the angular size of the core (for which we determined the physical parameters) was $\approx 0.03'' \times 0.017''$. However, the highest resolution measurements for 3C 190 have resolution $0.034'' \times 0.034''$ [41]. Thus, the real angular sizes of components could be smaller than indicated in radio measurements. For example, if the angular size of the core of 3C 190 is decreased by an order of magnitude, the magnetic field will decrease by four orders of magnitude and become 10 G for a linear scale of 10 pc. For comparison, a magnetic field >0.1 G was obtained for a scale of 40 pc for the giant radio galaxy DA 240 [58]. It is likely that such errors in the angular sizes of components led to errors in the calculated physical conditions for 3C 186, 3C 190, and 3C 213.1.

Figure 9 presents the dependences of the (a) magnetic field and (b) relativistic-electron density on the linear scale of the source. We can see especially clearly in Fig. 9a that the distribution of points is not random. We have fit linear dependences to both distributions on logarithmic scales. The points corresponding to results obtained in the present paper show the largest scatter about these lines. This probably reflects larger errors in the derived physical parameters resulting from the relatively sparse input data available for these sources. The parameters for the two linear dependences fit are

$$H = 10^{-11.7} L^{3.6} \text{ G},$$

$$n_e = 10^{9.5} L^{-5} \text{ cm}^{-3}.$$

Note that, if the density behaves in a fairly natural fashion (the smaller the scale for a feature, the higher the density in that feature), the behavior of the magnetic field is difficult to explain. The field is virtually absent on small linear scales and begins to grow as the linear size scale increases.

It is also possible that the turnovers in the spectra are due to thermal absorption. In [4], the possible presence of thermal plasma in the region emitting synchrotron radiation was considered; the temperature of the nonrelativistic plasma was $\sim 10^4$ K, and X-ray emission should come from a very small region $L_p < 1$ pc. In this case, the emission coefficient is determined by the synchrotron radiation, while the absorption coefficient is determined by the thermal plasma. It was demonstrated that the inferred density of thermal electrons was comparable to the density of thermal electrons in the cores of ultraluminous infrared galaxies. In [4], we considered this to be improbable. However, it seems appropriate to estimate in the same way the thermal electron

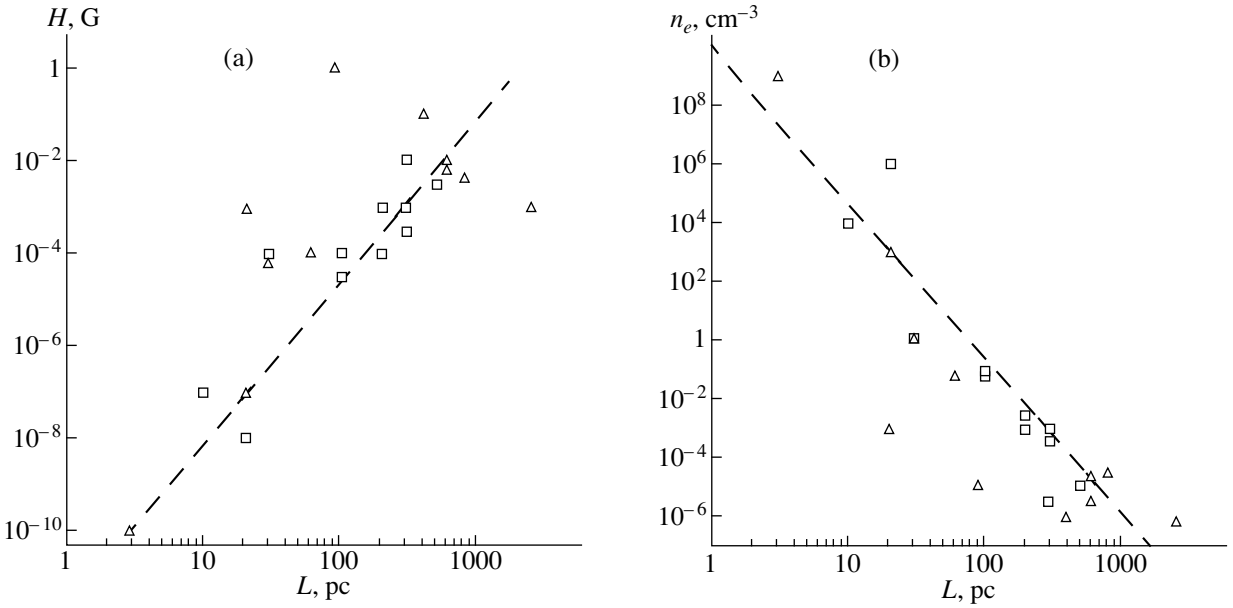

Fig. 9. Dependence of the (a) magnetic field strength H and (b) density of relativistic electrons n_e on the linear size of the radio source L. The squares present results from [4] and the triangles results from the present paper.

densities for the radio sources studied here, since the previous estimates for the thermal electron density exceed the expected densities on the size scales considered by only an order of magnitude. The resulting estimates are presented in Table 2. The columns present (1) the source name, (2) linear size, (3) peak frequency in the spectrum, and (4) inferred thermal electron density. We can see from this table that the estimates for n_e are higher than the densities of thermal electrons in our Galaxy on the same scales [59] and are close to the thermal plasma densities in ultraluminous IR galaxies [60]. Consequently, as asserted in [4], this mechanism for the low-frequency turnovers is improbable.

Table 2. Estimates of the nonrelativistic-electron density at temperature $T = 10^4$ K

Source name	L, pc	ν_p, GHz	n_e, cm^{-3}
4C 31.04	20	0.5	140
4C 34.07	20	0.4	110
OE 131	3	0.4	290
OF 247	50	1	90
3C 147 A	400	1.6	100
3C 147 B	2500	0.1	3
OI 407	30	0.6	140
3C 186	500	1	60
3C 190	100	3	380
3C 213.1	600	0.3	16
3C 237	800	0.2	9
3C 241	600	0.3	16
4C 14.41	60	0.4	66

Absorption due to the Razin–Tsytovich effect [61, 62] was also considered in [4], where it was shown to be improbable.

4. CONCLUSION

(1) 102-MHz interplanetary-scintillation observations of 21 compact steep-spectrum radio sources carried out on the LPA of the Lebedev Physical Institute indicate that nine of the sources have low-frequency turnovers in their radio spectra. Three of the 21 sources had been known earlier to have high-frequency turnovers.

(2) The most probable origin for such turnovers is synchrotron self-absorption. Based on this assumption, we estimated the magnetic-field strengths, relativistic-electron densities, and the energies of the magnetic field and relativistic electron–positron plasma in the compact components of the sources studied.

In all the quasars with low-frequency turnovers in their spectra, the relativistic-electron energy is much larger than the magnetic-field energy, with the exception of 3C 147, in which the opposite is true. At the same time, in all the radio galaxies analyzed, the magnetic-field energy is much larger than the relativistic-particle energy, with the exception of 4C 31.04, in which the two energies are comparable.

(3) There may be a correlation between the size of compact features and the physical conditions in them. The smaller the feature, the higher the density of relativistic electrons and the weaker the magnetic field. At the same time, the number of steep-spectrum sources for which we have been able to estimate these physical conditions is insufficient for a statistical analysis of the

properties of these sources and of possible differences between the conditions in quasars and radio galaxies. We are currently planning a final paper that will present our results for the remaining (~20) sources from the sample of [3], together with an analysis of our results for the sample as a whole.

ACKNOWLEDGMENTS

We wish to thank V.S. Artyukh for posing the initial problem and for his attention to our work, D. Dallacasa for presenting us with data for some of the sources, and L.B. Potapova for help in preparing the manuscript. This work was supported by the State Science and Technology Project "Astronomy" (project 1.2.5.7).

REFERENCES

1. J. A. Peacock and J. V. Wall, Mon. Not. R. Astron. Soc. **198**, 843 (1982).
2. V. K. Kapahi, Astron. Astrophys. Suppl. Ser. **43**, 381 (1981).
3. H. S. Sanghera, D. J. Saikia, E. Lüdke, *et al.*, Astron. Astrophys. **295**, 629 (1995).
4. V. S. Artyukh, S. A. Tyul'bashev, and P. A. Chernikov, Astron. Zh. **76**, 3 (1999).
5. K. J. Kellerman, Astrophys. J. **140**, 969 (1964).
6. V. S. Artyukh, Astron. Zh. **58**, 208 (1981).
7. V. S. Artyukh and S. A. Tyul'bashev, Astron. Zh. **73**, 669 (1996).
8. http:/www.prao.psn.ru/papers/tyulbashev
9. J. M. Wrobel and R. S. Simon, Astrophys. J. **309**, 593 (1986).
10. R. A. Perley, Astron. J. **87**, 859 (1982).
11. B. J. Geldzahler and A. Witzel, Astron. J. **86**, 1306 (1981).
12. I. I. K. Pauliny-Toth, K. I. Kellermann, M. M. Davis, *et al.*, Astron. J. **77**, 265 (1972).
13. P. C. Gregory and J. J. Condon, Astrophys. J., Suppl. Ser. **75**, 1011 (1991).
14. A. Witzel, P. Veron, and M. P. Veron, Astron. Astrophys. **11**, 171 (1971).
15. H. Kuehr, A. Witzel, I. I. K. Pauliny-Toth, *et al.*, Astron. Astrophys. Suppl. Ser. **45**, 367 (1981).
16. J. D. H. Pilkington and P. F. Scott, Mem. R. Astron. Soc. **69**, 183 (1965).
17. C. Fanti, R. Fanti, P. Parma, *et al.*, Astron. Astrophys. **143**, 292 (1985).
18. Rendong Nan, R. T. Schilizzi, C. Fanti, *et al.*, Astron. Astrophys. **252**, 513 (1991).
19. R. E. Spencer, J. C. McDowell, M. Charlesworth, *et al.*, Mon. Not. R. Astron. Soc. **240**, 657 (1989).
20. D. Dallacasa, *PhD Thesis*, Bologna (1993).
21. D. Dallacasa, C. Fanti, R. Fanti, *et al.*, Astron. Astrophys. **295**, 27 (1995).
22. T. J. Pearson, R. A. Perley, and A. C. S. Readhead, Astron. J. **90**, 738 (1985).
23. C. E. Akujor, R. E. Spencer, F. J. Zhang, *et al.*, Mon. Not. R. Astron. Soc. **250**, 215 (1991).
24. R. B. Phillips and R. L. Mutel, Astrophys. J. **244**, 19 (1981).
25. F. N. Owen, R. W. Porcas, and S. G. Neff, Astron. J. **83**, 1009 (1978).
26. W. J. M. van Breugel, G. Miley, and T. Heckman, Astron. J. **89**, 5 (1984).
27. C. E. Akujor, R. E. Spencer, and P. N. Wilkinson, Mon. Not. R. Astron. Soc. **244**, 362 (1990).
28. W. J. M. van Breugel, C. Fanti, R. Fanti, *et al.*, Astron. Astrophys. **256**, 56 (1992).
29. C. E. Akujor and S. T. Garrington, Astron. Astrophys. Suppl. Ser. **112**, 235 (1995).
30. P. N. Wilkinson, A. C. S. Readhead, G. H. Purcell, *et al.*, Nature **269**, 764 (1977).
31. A. C. S. Readhead, P. F. Napier, and R. C. Bignell, Astrophys. J. Lett. **237**, 55 (1980).
32. R. S. Simon, A. C. S. Readhead, A. T. Moffet, *et al.*, Astrophys. J. **236**, 707 (1980).
33. R. S. Simon, A. C. S. Readhead, A. T. Moffet, *et al.*, Astrophys. J. **354**, 140 (1990).
34. F. J. Zhang, C. E. Akujor, H. S. Chu, *et al.*, Mon. Not. R. Astron. Soc. **250**, 650 (1991).
35. W. Alef, E. Preuss, K. I. Kellermann, *et al.*, *IAU Symp. 129: The Impact of VLBI on Astrophysics and Geophysics*, Ed. by M. J. Reid and J. M. Moran (Reidel, Dordrecht, 1988), p. 95.
36. R. L. White and R. H. Becker, Astrophys. J., Suppl. Ser. **79**, 331 (1992).
37. A. Ficarra, G. Grueff, and G. Tomassetti, Astron. Astrophys. Suppl. **59**, 255 (1985).
38. P. J. S. Williams, S. Kenderdine, and J. E. Baldwin, Mem. R. Astron. Soc. **70**, 53 (1966).
39. T. A. T. Spoelstra, A. R. Patnaik, and Gopal-Krishna, Astron. Astrophys. **152**, 38 (1985).
40. T. V. Cawthorne, P. A. G. Scheuer, I. Morison, *et al.*, Mon. Not. R. Astron. Soc. **219**, 883 (1986).
41. R. E. Spencer, R. T. Schilizzi, C. Fanti, *et al.*, Mon. Not. R. Astron. Soc. **250**, 225 (1991).
42. I. Fejes, R. W. Porcas, and C. E. Akujor, Astron. Astrophys. **257**, 459 (1992).
43. T. J. Pearson and A. C. S. Readhead, Astrophys. J. **328**, 114 (1988).
44. P. D. Barthel, T. J. Pearson, and A. C. S. Readhead, Astrophys. J. **329**, L51 (1988).
45. T. J. Pearson and A. C. S. Readhead, Astrophys. J. **248**, 61 (1981).
46. R. A. Preston, D. D. Morabito, J. G. Williams, *et al.*, Astron. J. **90**, 1599 (1985).
47. A. G. Polatidis, P. N. Wilkinson, W. Xu, *et al.*, Astrophys. J., Suppl. Ser. **98**, 1 (1995).
48. R. Genzel, I. I. K. Pauliny-Toth, E. Preuss, *et al.*, Astron. J. **81**, 1084 (1976).
49. I. I. K. Pauliny-Toth, A. Witzel, E. Preuss, *et al.*, Astron. J. **83**, 451 (1978).
50. F. N. Owen, S. R. Spangler, and W. D. Cotton, Astron. J. **85**, 351 (1980).
51. B. Anderson and W. Donaldson, Mon. Not. R. Astron. Soc. **137**, 81 (1967).

52. A. Wright and R. E. Otrupcek, Bull. Inf. Centre Donnees Stellaires **41**, 47 (1992).
53. D. W. Murphy, I. W. A. Browne, and R. A. Perley, Mon. Not. R. Astron. Soc. **264**, 298 (1993).
54. L. Padrielli, W. Eastman, L. Gregorini, *et al.*, Astron. Astrophys. **249**, 351 (1991).
55. R. G. Strom, J. M. Riley, H. Spinrad, *et al.*, Astron. Astrophys. **227**, 19 (1990).
56. R. Liu and G. Pooley, Mon. Not. R. Astron. Soc. **249**, 343 (1991).
57. V. S. Artyukh, Tr. Fiz. Inst. im. P. N. Lebedeva **189**, 223 (1988).
58. V. S. Artyukh and M. A. Ogannisyan, Pis'ma Astron. Zh. **14**, 706 (1988).
59. D. Downes and A. Maxwell, Astrophys. J. **146**, 653 (1966).
60. V. S. Artyukh, A. V. Zasov, and S.A. Tyul'bashev, Pis'ma Astron. Zh. **21**, 723 (1995).
61. V. A. Razin, Izv. Vyssh. Uchebn. Zaved., Radiofiz. **3**, 921 (1960).
62. V. N. Tsytovich, *Nonlinear Effects in Plasma* (Nauka, Moscow, 1967), p. 287.

Translated by D. Gabuzda

Astronomy Reports, Vol. 44, No. 5, 2000, pp. 298–308. Translated from Astronomicheskiĭ Zhurnal, Vol. 77, No. 5, 2000, pp. 345–356.

Equilibrium Phase-Space Density Distribution in Numerical Dynamical Models of Open Clusters

V. M. Danilov

Astronomical Observatory, Ural State University, pr. Lenina 51, Yekaterinburg, 620083 Russia

Received November 12, 1998

Abstract—In dynamical models for open clusters, virial equilibrium is not achieved over the violent relaxation time scale τ_{vr}. The stars form an equilibrium distribution in (ε, ε_ζ, l) space, where ε and l are the energy and angular momentum per unit stellar mass in the combined field of the Galaxy and cluster and ε_ζ is the energy of motion perpendicular to the Galactic plane per unit mass of cluster stars in the gravitational field of the Galaxy. This distribution of stars changes little when $t > \tau_{vr}$. The stellar phase-space distribution corresponding to this type of equilibrium and the regular cluster potential vary periodically (or quasi-periodically) with time. This phase-space equilibrium is probably possible due to an approximate balance in the stellar transitions between phase-space cells over times equal to the oscillation period for the regular cluster field. *© 2000 MAIK "Nauka/Interperiodica".*

1. INTRODUCTION

In [1], we considered models of open clusters that were nonstationary with respect to the regular cluster field. In the course of their dynamical evolution, such models develop an equilibrium distribution of stars in the space of certain parameters of the stellar motion over the first violent-relaxation time scale τ_{vr}. This distribution varies little with time when $t > \tau_{vr}$. The stellar phase-space distribution corresponding to this equilibrium and the regular potential of the cluster vary periodically (or quasi-periodically) with time. In the open-cluster models of [1], virial equilibrium was not attained, and at $t > \tau_{vr}$, the virial coefficients of the cluster models continued oscillating with nearly constant amplitude and period. We will call the phase-space density of the cluster corresponding to the equilibrium attained at $t > \tau_{vr}$ the equilibrium phase-space density. In this equilibrium, there is probably an approximate balance in the stellar transitions between phase-space cells on time scales equal to the oscillation period of the regular cluster field.

Due to the instability of the phase-space density to small perturbations, open-cluster models with low phase-space densities develop different equilibrium phase-space densities over the time $t \simeq \tau_{vr}$. In each of the intervals of distance from the cluster center considered in [1], the relative differences between the phase-space densities of such models averaged over the stellar velocities increased at $t < \tau_{vr}$ and stabilized at $t > \tau_{vr}$. Here, t_r is the local violent relaxation time a distance r from the cluster center. The fact that the mean-velocity relative phase-space density differences stabilize and remain constant in time indicates the formation of an equilibrium phase-space density in the cluster models.

Kandrup *et al.* [2] considered the energy–space domain occupied by the particles of an isolated system that is nonstationary in the regular field, subdividing this domain into 20-particle intervals at each moment in time. The mean particle energies in these intervals remain nearly constant once the system attains a certain equilibrium state. According to [2], this indicates a constraint on the coarse-grained phase-space density, which restricts the possible outcome of violent relaxation in the system. We believe that this constancy of the average particle energies is due to a balance in the particle transitions between the energy intervals considered in [2], which is typical of systems that have attained equilibrium in the particle energy space.

Kandrup [3] performed a theoretical analysis of the evolution of collisionless self-gravitating systems. According to [3], in a "coarse-grained" description, such systems can approach a time-independent equilibrium during their evolution, which corresponds to time-dependent distribution functions f_0 for certain parameters that are "energy extremal" with respect to all perturbations δf in the systems of gravitating points. Depending on the type of extremum, the function f_0 can be linearly stable or unstable, and the system's evolution can proceed with linear or nonlinear phase-space oscillations about f_0. At the same time, Kandrup [3] points out that it is not clear what sort of coarse-grained description should be implemented in order to recognize the approach of the system to equilibrium.

Theoretical and experimental analyses of the properties and parameters of the equilibrium phase-space density that develops as a result of the violent relaxation of a nonstationary open cluster are of interest here. In the case of open clusters moving in circular orbits in the Galactic plane, the phase-space density

1063-7729/00/4405-0298$20.00

that forms as a result of violent relaxation is constrained by the conditions of conservation of cluster mass M and energy E, as well as by the symmetries present in the density and stellar velocity distributions in the cluster.

According to formulas (5.517–5.519) in [4], the equations of motion for cluster stars in (ξ, η, ζ) coordinates imply, under a number of assumptions, that the cluster "energy" is an integral of motion; i.e., E = const (formula (5.522) in [4]). In addition, if the cluster is symmetric with respect to the $\xi\zeta$ and/or $\eta\zeta$ planes, the angular momentum of the cluster is another integral of motion; i.e., A_ζ = const (formula (5.530) in [4]). (Chandrasekhar [4] uses the rotating coordinate system (ξ, η, ζ) fixed to the center of mass of the cluster, where the ξ, η, and ζ axes are directed from the center of mass of the cluster away from the Galactic center, in the direction of Galactic rotation, and perpendicular to the Galactic plane, respectively.) After multiplying by $\dot\zeta_i = \frac{d\zeta_i}{dt}$ and summing over all cluster stars, the stellar equation of motion along the ζ coordinate (formula (5.519) in [4]) yields

$$\frac{d}{dt}\sum_{i=1}^{N} m_i\varepsilon_{\zeta,i} = -\sum_{i=1}^{N}\dot\zeta_i\frac{\partial\Omega}{\partial\zeta_i} = Q, \qquad (1)$$

where m_i is the mass of the ith cluster star; Ω and N are the potential energy and the number of stars in the cluster, respectively; $m_i\varepsilon_{\zeta,i} = \frac{1}{2}m_i(\dot\zeta_i^2 + \alpha_3\zeta_i^2)$ is the energy of motion of the ith cluster star along the ζ axis in the Galactic gravitational field; and α_3 = const.

In the cluster models considered here, Q and $E_\zeta = \sum_{i=1}^{N} m_i\varepsilon_{\zeta,i}$ exhibit oscillations that are damped with time t. Q oscillates about $Q = 0$. The largest deviations of Q from zero are small and correspond to relative E_ζ variations of several per cent (6.4 and 4.5%) for cluster models 1 and 2 below, respectively. The oscillations in Q and E_ζ are due to oscillations in $\varepsilon_{\zeta,i}$ for the relatively small number of stars with the highest $\varepsilon_{\zeta,i}$ values (see Fig. 2 below). The relative deviations of $\varepsilon_{\zeta,i}$ for these stars are, on average, 20% when $t < \tau_{vr}$ and decrease by a factor of 2–4 when $t > \tau_{vr}$. The oscillations in $\varepsilon_{\zeta,i}$ averaged over several stars within specified $\varepsilon_{\zeta,i}$ intervals (see Fig. 2 below) indicate that the establishment of an equilibrium stellar distribution function in ε_ζ space proceeds more slowly at high ε_ζ than at low and intermediate ε_ζ. Some of the stars with the highest $\varepsilon_{\zeta,i}$ values gradually escape from the cluster in the course of its evolution.

Using the condition $Q = 0$ as an approximation to describe the evolution of the open cluster, we find, in accordance with (1), that E_ζ = const. This condition follows from the symmetry of the potential $U(\mathbf{r})$ and the velocity distribution $g(\dot\zeta)$ with respect to the $\zeta = 0$, plane in the cluster model (here, $\mathbf{r} = (\xi, \eta, \zeta)$ is the radius-vector of a cluster star).

In the collisionless approximation, the right-hand sides of the equations of stellar motion (formulas (5.517–5.519) in [4]) should be replaced by partial derivatives (multiplied by m_i) of the regular potential U with respect to the corresponding coordinates ξ, η, ζ. In this case, after computing the stellar integrals of motion in the usual way, it can easily be shown that the energy of the motion per unit stellar mass ε_i is an integral of the motion:

$$\varepsilon_i = \frac{v_i^2}{2} - U + \alpha_1\frac{\xi_i^2}{2} + \alpha_3\frac{\xi_i^2}{2} = \text{const}, \qquad (2)$$

where α_1 = const, $v_i^2 = \dot\xi_i^2 + \dot\eta_i^2 + \dot\zeta_i^2$, and the angular momentum per unit mass l_i and energy $\varepsilon_{\zeta,i}$ of motion along the ζ coordinate are not integrals of the motion:

$$l_i = \dot\xi_i\eta_i - \xi_i\dot\eta_i - \omega_c(\xi_i^2 + \eta_i^2) \neq \text{const},$$
$$\varepsilon_{\zeta,i} \neq \text{const}, \qquad (3)$$

where ω_c = const is the angular velocity of the cluster with respect to the Galactic center.

The quantities M, E, $A_\zeta = \sum_{i=1}^{N} m_i l_i$, and E_ζ are conserved during violent relaxation of the cluster (see [4] and text above). Following [5], we can obtain the most likely (equilibrium) stellar distribution in $(\varepsilon, \varepsilon_\zeta, l)$ space from the condition of maximum entropy of the system combined with the above constraints on M, E, A_ζ, and E_ζ. If the possible states are filled by only a few stars (i.e., if the stars occupy only a small fraction of the phase-space microcells belonging to a predefined macrocell—a "coarse-grained" cell in the phase space [6]), this leads to the Maxwell–Boltzmann distribution

$$f(\varepsilon, \varepsilon_\zeta, l) = f_0\exp(-\nu - \mu\varepsilon - \beta l - \gamma\varepsilon_\zeta), \qquad (4)$$

where f_0, ν, μ, β, γ are constants.

If a star cluster develops an equilibrium distribution of the form (4) as a result of various relaxation mechanisms (including those due to stellar encounters), the mean values of ε, ε_ζ, and l for stars located in predefined cells in $(\varepsilon, \varepsilon_\zeta, l)$ space (see below) should be conserved at times $t > \tau_{vr}$. Kandrup *et al.* [2] obtained a similar result for ε in models of isolated star clusters for systems that have attained some sort of equilibrium by the end of the violent-relaxation stage.

An experimental analysis of the form, parameters, and properties of the equilibrium phase-space distribution of stars $F_0(\mathbf{r}, \mathbf{v}) \sim f(\varepsilon, \varepsilon_\zeta, l) = f(\varepsilon(\mathbf{r}, \mathbf{v}), \varepsilon_\zeta(\mathbf{r}, \mathbf{v}), l(\mathbf{r}, \mathbf{v}))$ for nonstationary open-cluster models is of interest. Here, $\mathbf{v} = (\dot\xi, \dot\eta, \dot\zeta)$ is the star's velocity vector in the cluster. The results of such analyses can be used to construct analytical cluster models that are nonstationary in the regular cluster field, investigate the stellar velocity fields in such clusters, and estimate the total masses and

other cluster parameters from the coordinate and velocity data for cluster stars.

The aim of this paper is to analyze the equilibrium stellar distribution functions in $(\varepsilon, \varepsilon_\zeta, l)$ space and phase space that develop during violent relaxation in open-cluster models that are nonstationary in the regular cluster field.

2. DESCRIPTION OF MODELS

We now consider a cluster consisting of $N = 500$ stars moving in the Galactic plane about the Galactic center in a circular orbit of radius 8200 pc. At the initial time t, the cluster is modeled as a system of two concentric gravitating spheres, imitating the halo and core of the cluster. We considered open-cluster models with initial parameters $\frac{R_1}{R_2} = 0.24$ and $\frac{N_1}{N_2} = 0.25$ and strong manifestations of non-stationarity in the regular cluster field. Here, R_1 and R_2 are the radii of the cluster core and halo, respectively, and N_1 and N_2 are the number of stars in the core and halo, respectively. These parameters correspond to model 5 in [7]. We assumed that all cluster stars have mass 1 $M_\odot$. We used a random-number generator to specify the initial positions and velocities of the stars in the (r, θ, φ) and $(v_r, \theta_v, \varphi_v)$ spherical coordinate systems fixed to the (ξ, η, ζ) and $(\dot\xi, \dot\eta, \dot\zeta)$ Cartesian reference frames. Here, v_r is a star's radial velocity component and $r = |\mathbf{r}|$.

We analyzed two cluster models. In model 1, as in the models considered in [7], the angles φ and φ_v specifying the direction of the vectors **r** and **v** in the (ξ, η) and $(\dot\xi, \dot\eta)$ planes, and also the angles θ and θ_v specifying the projections of the vectors **r** and **v** onto the ζ and $\dot\zeta$ axes, are randomly distributed in the intervals θ, $\theta_v \in [0, \pi]$ and φ, $\varphi_v \in [0, 2\pi]$ using a random-number generator. In model 2, the azimuthal angles φ and φ_v are distributed as in model 1, and the angles θ and θ_v are distributed in the interval $[0, \pi]$ in accordance with the probability density functions $p(\theta) = \frac{1}{2}\sin\theta$ and $p(\theta_v) = \frac{1}{2}\sin\theta_v$, respectively. In both models, the distance r is distributed over the intervals $[0, R_i]$ with probability density $p(r) = 3r^2/R_i^3$ $(i = 1, 2)$ to ensure constancy of the stellar number density in subsystems at different radii. Model 1 corresponds to model 5 in [7].

The initial stellar number densities in model 2 are approximately the same at all points of the subsystems considered. In model 1, there is some excess of stars with large $|\zeta|$ and $|\dot\zeta|$ at $t = 0$, resulting in a two-peaked initial velocity distribution, with local maxima at large and small $\dot\zeta$. Because of the uniform initial distribution of θ and θ_v over the interval $[0, \pi]$ in model 1, the factors $\sin\theta = r/\sqrt{\xi^2 + \eta^2}$ and $\sin\theta_v = v/\sqrt{\dot\xi^2 + \dot\eta^2}$ appear in the expressions for the initial density and velocity distributions for this model. Here, $r^2 = \xi^2 + \eta^2 + \zeta^2$, $v^2 = \dot\xi^2 + \dot\eta^2 + \dot\zeta^2$ and, for the sake of brevity, we do not present the formulas for the above distributions. According to [7], cluster model 5 develops a core that is extended along the ζ axis. Our computations show that model 2 develops a spherical core. The extension of the cores of the cluster models analyzed in [7] along the ζ axis was, thus, due to the particular choice of initial conditions.

Models 1 and 2 are defined such that, at $t = 0$, they do not rotate with respect to external galaxies, and the cluster and its subsystems meet the conditions of virial equilibrium for isolated clusters. We used the units 1 pc, 1 Ma, and 1 $M_\odot$ in our computations. For each model with fixed R_i, N_i $(i = 1, 2)$ at $t = 0$, we computed the dynamical evolution several times with slightly (and randomly) different initial stellar phase-space coordinates. See [7] for a description of the technique used to generate the magnitudes of the vectors **v** for the initial stellar velocities and small perturbations of the stellar phase-space coordinates in the cluster. We smoothed the force functions in the right-hand sides of the stellar equations of motion (see [7] for a description of the technique employed and the smoothing parameter).

In our computations, we used the (ξ, η, ζ) coordinate system (see above) and corresponding equations of stellar motion (formulas (5.517)–(5.519) in [4]) with the components of the Galactic field given up to linear terms in ξ, η, and ζ. We used the formula for Φ presented by Kutuzov and Osipkov [8] to compute the constant coefficients α_1 and α_3 in the expansion for the regular Galactic potential Φ as a power series in ξ, η, and ζ. In contrast to [4], we have (in the notation adopted here):

$$\Phi \geq 0,\ \frac{\partial\Phi}{\partial R} \leq 0,\ \alpha_1 = \left(\frac{1}{R}\frac{\partial\Phi}{\partial R} - \frac{\partial^2\Phi}{\partial R^2}\right)_0,\ \text{and}\ \alpha_3 = -\left(\frac{\partial^2\Phi}{\partial Z^2}\right)_0,$$

where R and Z are cylindrical Galactocentric coordinates; the subscript 0 indicates that the derivatives of Φ are taken at $R = 8200$ pc and $Z = 0$ for the adopted circular cluster orbit in the Galactic plane.

We monitored the integration errors by checking the constancy of the integral of the energy E of peculiar motions of the cluster stars (formula (5.522) in [4]). We also used the statistical method [9], which is more sensitive to computational errors, to monitor the accuracy of integration of the equations of motion; this allowed us to check the accuracy of the computed phase-space density in the dynamical cluster models.

To integrate the equations of motions of the cluster stars, we used an improved (optimized) version of the code [9] (we reduced the number of operations required to solve the equations, eliminated certain operations involving numbers with different sizes in the computer

memory, etc.). As a result, we increased the time interval t_0 for the dynamical evolution during which the accuracy of the computed cluster phase-space density can be considered sufficient from $t_0 = 1.7\tau_{vr}$ (the maximum attained in [9]) to $t_0 = 1.9\tau_{vr}$ for model 1 and $t_0 = 2.2\tau_{vr}$ for model 2. As in [7, 9], we adopted an initial violent relaxation time of $\tau_{vr} = 2.6\bar{t}_{cr} \sim 5 \times 10^7$ yr; $\bar{t}_{cr}$ is the average cluster crossing time.

We integrated the equations of motion using sixth and seventh order Runge–Kutta methods with the grid functions (2) from [9], with an accuracy of 15–16 decimal places. The maximum relative error of the computed energy E did not exceed 2.8×10^{-8} and 2.1×10^{-9} for cluster models 1 and 2, respectively. The computations also met the statistical criterion for the accuracy of the computed phase-space density ($0.9 \le P_j \le 1.0$) for all distance intervals Δr_j ($j = 1, \ldots, 10$) considered (see below). Here, $P_j = P(r \in \Delta r_j)$ are the probabilities that the samples of stellar phase-space coordinates obtained by solving the equations of motions with seventh- and sixth-order integration methods are drawn from the same stellar phase-space coordinate population. According to [9], the differences between the stellar phase-space coordinate distributions obtained using the seventh- and sixth-order methods are random, and the accuracy of the computed stellar phase-space coordinates can be considered sufficiently high to use them to draw conclusions about the physical properties of the phase-space density of a cluster model.

We compared the results obtained with cluster models 1 and 2 with slightly different initial stellar phase-space coordinates. To this end, we subdivided all the stars of cluster model 1 at time t into ten groups of 50 stars in order of increasing distance r from the cluster center of mass. Let Δr_j be the distance interval r_j corresponding to the jth group ($j = 1, \ldots, 10$). See [1] for the technique used to partition the velocity space occupied by the cluster stars into k equal cells. When computing the cluster evolution, we followed the time variations of the relative differences ψ_j of the phase-space densities of cluster models 1 and 2 in the distance intervals Δr_j averaged over all k velocity-space cells with $k = 1000$.

3. RESULTS OF COMPUTATIONS AND DISCUSSION

In the cluster models considered, there is initially a small contraction (mainly perpendicular to the Galactic plane) that ends by a time $t \simeq (0.30\text{–}0.35) \times \tau_{vr}$. At $t > 0.6 \times \tau_{vr}$, steady-state oscillations in the regular field are established, with periods of $P_r = 0.7 \times \tau_{vr}$ and $P_r = 0.6 \times \tau_{vr}$ in models 1 and 2, respectively. The mean ratios $\delta\alpha$ of the amplitudes of the virial coefficient $\alpha = 2E_c/\Omega$ and the value $\alpha = \alpha_v$ averaged over the period P_r are equal to 0.55–0.59 for models 1 and 2, indicating that the models are appreciably nonstationary in the regular field (here, $E_c = T + \Omega$ and T is the total kinetic energy of the cluster-star peculiar motions).

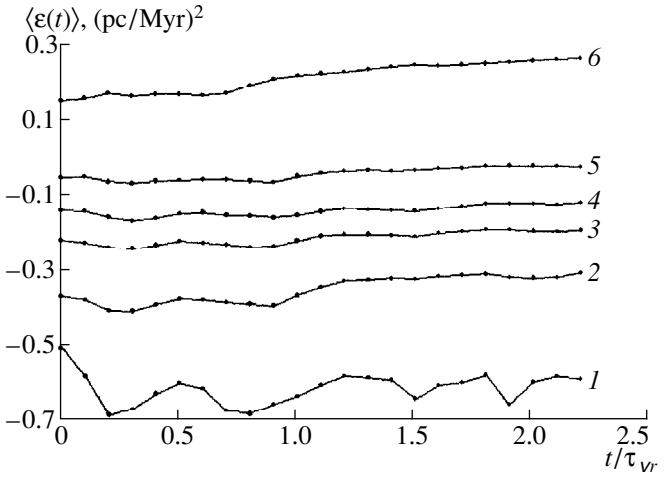

Fig. 1. ⟨ε⟩ values averaged over five stars as a function of time. The stars are numbered in order of increasing ε. Curves *1, 2, 3, 4, 5,* and *6* are based on the results for stars 1–5, 101–105, 201–205, 301–305, 401–405, and 496–500 in ε space, respectively.

The fractional phase-space density differences ψ_j due to instability of the phase-space densities to small initial perturbations in the stellar phase-space coordinates increase rapidly during a time t_r, then remain approximately constant, and an equilibrium phase-space density is established in cluster models 1 and 2 (see, e.g., Fig. 1 in [1]). The values of t_r can be considered estimates of the local relaxation time. t_r in the central regions of models 1 and 2, whereas $t_r \simeq 0.5 \times \tau_{vr}$ and $t_r \simeq 1.1 \times \tau_{vr}$ and $t_r \simeq 1.5 \times \tau_{vr}$ at the peripheries of models 1 (see also [1]) and 2, respectively. Thus, model 2, which has a single-peaked initial distribution of $\dot{\zeta}$ coordinates that is closer to the equilibrium distribution, is slower to develop the equilibrium phase-space density at its periphery. In the central regions, the equilibrium phase-space density develops over essentially the same time for models 1 and 2 ($0.5 \times \tau_{vr}$).

To analyze the properties and parameters of the equilibrium distributions that develop in models 1 and 2, we, like Kandrup *et al.* [2], subdivide all cluster stars at each time t into groups consisting of five stars (10 and 20), with each in order of ascending specific energy ε per unit stellar mass [see formula (2)]. We then compute the mean ⟨ε⟩ and the dispersions of ε—⟨ε⟩ for each group and perform analogous computations for l and ε_ζ [see formula (3) and the discussion of formula (1)]. Figures 1–3 show ⟨ε⟩, ⟨ε_ζ⟩, and ⟨l⟩ plotted as functions of time for a number of the stellar groups in cluster model 2 (the corresponding relations for model 1 are similar to those in Figs. 1–3). ⟨ε⟩, ⟨ε_ζ⟩, and ⟨l⟩ remain virtually constant at $t > \tau_{vr}$ throughout most of the ε, ε_ζ, and l domain occupied by the cluster stars. Deviations of ⟨ε⟩,

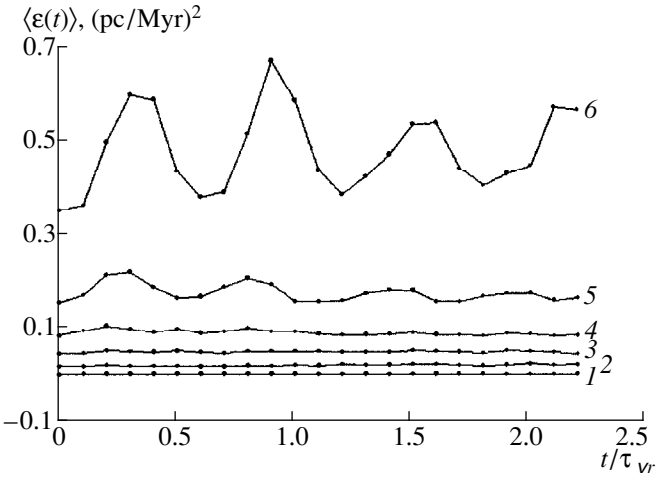

Fig. 2. Same as Fig. 1 for $\langle\varepsilon_\zeta\rangle$.

$\langle\varepsilon_\zeta\rangle$, and $\langle l\rangle$ from their constant values become appreciable with time only near the boundaries of the distributions of ε, ε_ζ, and l, where the number of stars is small. The increase of $\langle\varepsilon\rangle$ with time at high ε at $t > \tau_{vr}$ is due to stars at the cluster periphery (near or outside the cluster tidal radius $r = R_t$ [10]). The fractional amplitudes of oscillations of $\langle\varepsilon\rangle$ are small for small ε, amounting to ~11 and 6% at $t < \tau_{vr}$ and $t > \tau_{vr}$, respectively, and are determined by stars located near the cluster center. The decrease with time of $\langle l\rangle$ at small l is due to stars escaping from the cluster, located at distances $r > 2R_t$ from the cluster center. The highest fractional amplitudes of oscillations of $\langle\varepsilon_\zeta\rangle$ at large ε_ζ are 13–25% at $t < \tau_{vr}$ and decrease by a factor of 2–4 at $t > \tau_{vr}$. These oscillations are due to the small number of stars outside the cluster core, at the cluster periphery. Since $\langle\varepsilon\rangle$, $\langle\varepsilon_\zeta\rangle$, and $\langle l\rangle$ are primarily constant in time only for stars at distances $r < R_t$ (i.e., inside the cluster), the constancy of $\langle\varepsilon\rangle$, $\langle\varepsilon_\zeta\rangle$, and $\langle l\rangle$ must be due to stellar encounters within the cluster. (The periods of temporal oscillations of $\langle\varepsilon\rangle$, $\langle\varepsilon_\zeta\rangle$, and $\langle l\rangle$ are mostly near $P_r = 0.6\tau_{vr}$, so that temporal oscillations of $\langle\varepsilon\rangle$, $\langle\varepsilon_\zeta\rangle$, and $\langle l\rangle$ are most likely due to oscillations of the regular cluster field.)

The dispersions σ_ε, $\sigma_{\varepsilon,\zeta}$, and σ_l of the deviations of ε, ε_ζ, and l from $\langle\varepsilon\rangle$, $\langle\varepsilon_\zeta\rangle$, and $\langle l\rangle$ in the intervals of these parameters considered are also characterized by the sizes of these intervals and, at $t > \tau_{vr}$, should exhibit small, random oscillations about certain constant values over most of the domain $S = (\varepsilon, \varepsilon_\zeta, l)$ occupied by the cluster stars in the (ε, ε_ζ, and l) coordinate space. σ_l for stars with small l increases when these stars move to distances $r > 2R_t$. The dispersions σ_ε for the stars with the highest and lowest ε change appreciably at $t < \tau_{vr}$ (the stellar ε distributions develop their "wings" during this period). The constancy of $\langle\varepsilon\rangle$, $\langle\varepsilon_\zeta\rangle$, and $\langle l\rangle$ and of σ_ε, $\sigma_{\varepsilon,\zeta}$, and σ_l for most of the cluster stars at $t > \tau_{vr}$ indicates that the stellar distribution in (ε, ε_ζ, and l) space has attained equilibrium.

Figure 4 shows the distribution of stars in model 2 in (ε, ε_ζ, l) space for seven equally spaced times t_i (separated by steps $\Delta t = 0.1\tau_{vr}$ for $t_i/\tau_{vr} \in [1.0, 1.6]$, $i = 1, \ldots, 7$) spanning the period $P_r = t_7 - t_1$ for the oscillations of the regular cluster field. The dashed curves show the distributions averaged over P_r. The central distributions correspond to $\bar{t} = \frac{1}{7}\sum_{i=1}^{7} t_i = 1.3 \times \tau_{vr}$,

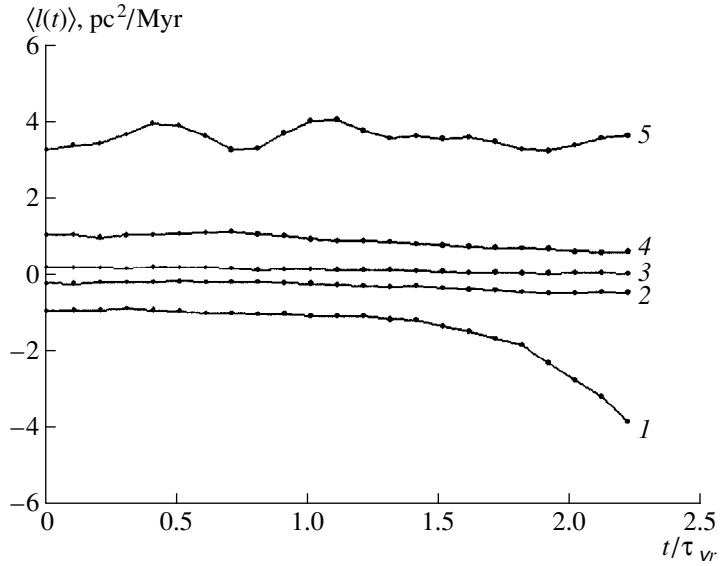

Fig. 3. Same as Fig. 1 for $\langle l\rangle$. Curves *1*, *2*, *3*, *4*, and *5* are based on results for stars 101–105, 201–205, 301–305, 401–405, and 496–500 in l space, respectively.

and have been constructed as follows. During the integration of the equations of stellar motions, the sets of stellar phase-space coordinates for the seven times indicated are written to a single file, which is then used to compute the overall stellar distributions in (ε, ε_ζ, l) space. The resulting distributions are then normalized to the number of stars in the cluster ($N = 500$). Although the cluster is strongly nonstationary, and in spite of the oscillations of the regular field in cluster model 2 over the period P_r, the "instantaneous" distributions of ε, ε_ζ, and l at time t differ little from the corresponding distributions averaged over the period for oscillations of the regular field. Figure 5 shows the distributions of the magnitude of the stellar velocities $v = |\mathbf{v}|$ for the times indicated, which differ more from the mean distribution than do the distributions in Fig. 4. It is interesting that, during the violent relaxation of the cluster model considered, i.e., for $t_i/\tau_{vr} \in [0, 0.6]$, the differences between the instantaneous distributions of ε_ζ and l and the corresponding mean distributions are as small as those in Fig. 4. The differences between the instantaneous and mean distributions of ε for $t_i/\tau_{vr} \in [0, 0.6]$ are somewhat more substantial than for $t_i/\tau_{vr} \in [1.0, 1.6]$.

Although cluster model 2 is strongly nonstationary in the regular field, the instantaneous distribution of the stars in (ε, ε_ζ, l) space attains equilibrium at $t > \tau_{vr}$; the resulting equilibrium distribution varies only slightly over the period P_r, does not differ statistically from the distribution $f(\varepsilon, \varepsilon_\zeta, l)$ averaged over P_r, and exhibits only small random deviations from (ε, ε_ζ, l) (see below).

4. EQUILIBRIUM DISTRIBUTION OF CLUSTER STARS IN (ε, ε_ζ, l) SPACE

We estimated the parameters of the stellar distribution in (ε, ε_ζ, l) space for cluster model 2 for several times $\dot{t}$. To this end, we used the distribution (4) written in the more convenient form

$$f(\varepsilon, \varepsilon_\zeta, l) = f_0 \exp(-\mu|\varepsilon - \bar{\varepsilon}| - \beta|l - \dot{l}| - \gamma\varepsilon_\zeta), \quad (5)$$

where $\bar{\varepsilon}$ and $\dot{l}$ are ε and l averaged over P_r, derived from the set of stellar phase-space coordinates for seven equally spaced times corresponding to the given $\dot{t}$. The quantity ν from (4) can be written $\nu = \pm\mu\bar{\varepsilon} \pm \beta\dot{l}$, where the signs in front of the μ and β coefficients depend on those of $\varepsilon - \bar{\varepsilon}$ and $l - \dot{l}$.

To estimate the parameters of distribution (5), we subdivided the ε domain occupied by the cluster stars during the given period P_r into $L = 60$ equal intervals $\Delta\varepsilon$. To determine this domain, we used the combined file containing the stellar phase-space coordinates for seven equally spaced times spanning the period P_r. We also partitioned the $\Delta\varepsilon_\zeta$ and Δl domains occupied by the cluster stars during the period P_r into intervals ε_ζ and l in the same way. We then determined the stellar number densities $f(\varepsilon, \varepsilon_\zeta, l)$ in the resulting (ε, ε_ζ, l)-space cells

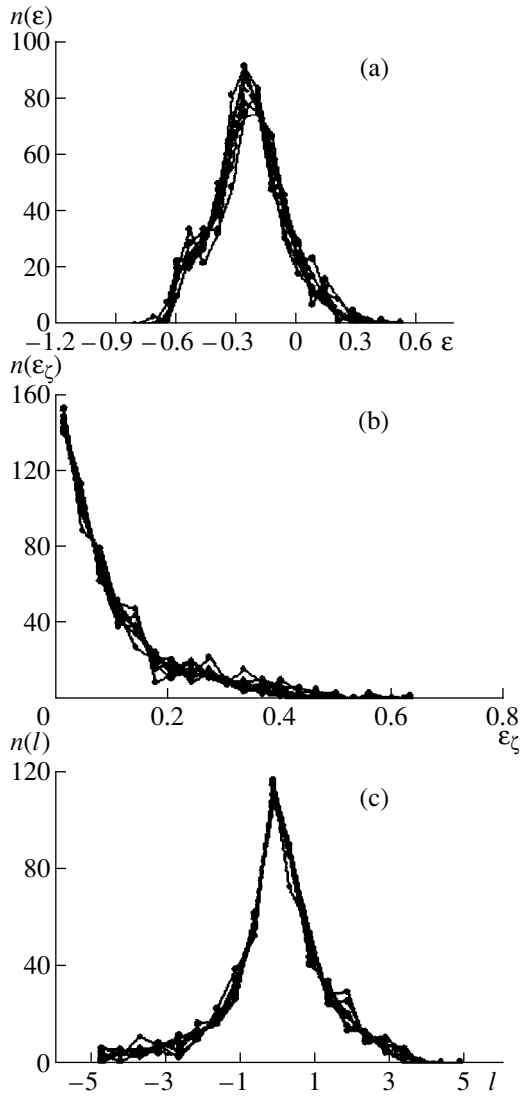

Fig. 4. The ε, ε_ζ, and l distributions for stars in model 2 for times $t_i = [1 + (i - 1) \times 0.1]\tau_{vr}$, $i = 1, \ldots, 7$. The dashed curves show the $n(\varepsilon)$, $n(\varepsilon_\zeta)$, and $n(l)$ distributions of the cluster stars averaged over P_r at time $\dot{t} = 1.3\tau_{vr}$.

and derived the parameters of distribution (5) using the method of Marquardt [11] to minimize the sum of the squares of the deviations of f_1 from f computed using (5). We repeated these computations for $L = 20$ and 40.

The table summarizes the resulting coefficient estimates for $L = 60$ (for $L = 20$ and 40, the function f is more coarsely represented by f_1 near the maximum f values). We can see from the table that the parameters of the stellar distribution $f(\varepsilon, \varepsilon_\zeta, l)$ averaged over P_r for cluster model 2 vary comparatively little over the time interval considered (from $\dot{t} = 1.3 \times \tau_{vr}$ to $\dot{t} = 1.9 \times \tau_{vr}$). Such variations of the stellar distribution in (ε, ε_ζ, l) space could be due, among other things, to approximation errors when fitting the function $f_1(\varepsilon, \varepsilon_\zeta, l)$ using (5).

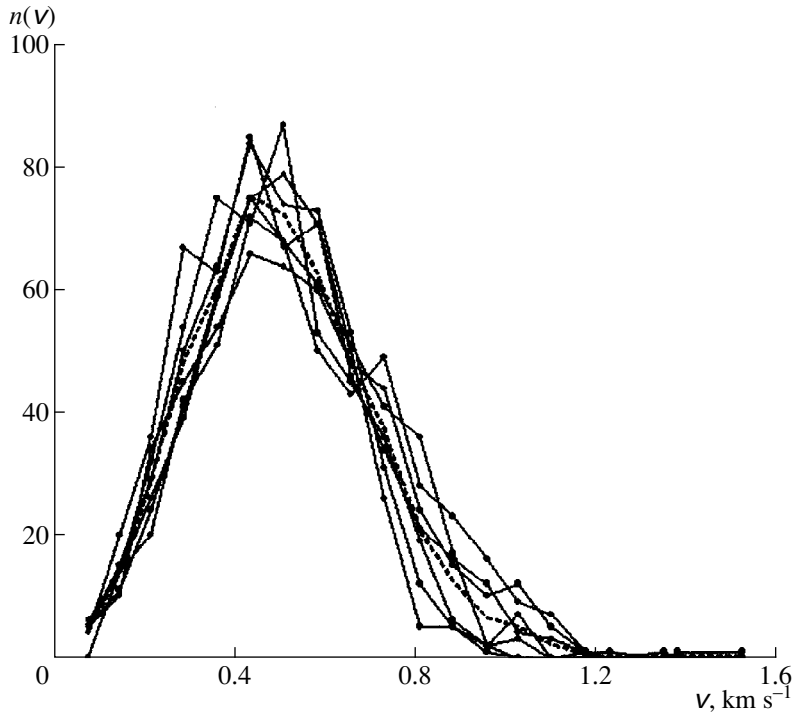

Fig. 5. Distributions of stellar velocity magnitudes in model 2 for times $t_i = [1 + (i - 1) \times 0.1]\,\tau_{vr}$, $i = 1, \ldots, 7$. The dashed curve shows the $n(v)$ distribution of the cluster stars averaged over P_r at time $\dot{t} = 1.3\tau_{vr}$.

The function (5) used as $f(\varepsilon, \varepsilon_\zeta, l)$ only approximately describes the properties of $f_1(\varepsilon, \varepsilon_\zeta, l)$. A more accurate description of the averaged ε distribution of stars could probably be obtained by using two exponential functions in (5) to fit the distributions of ε in the cluster core and halo (see Fig. 4a). The small temporal variations of distribution (5) in the table could also be due to systematic changes (evolution) of the averaged cluster model. f_0 systematically decreases over the time considered in the table due to the expansion of the cluster in phase space.

When comparing $f_1(\varepsilon, \varepsilon_\zeta, l)$ and $f(\varepsilon, \varepsilon_\zeta, l)$, we should bear in mind that ε and ε_ζ are not independent. To determine the boundaries of the $(\varepsilon, \varepsilon_\zeta)$ domain occupied by the stars in the cluster model averaged over P_r, we used the combined file containing the stellar phase-space coordinates for seven equally spaced times spanning period P_r. We derived the relations $\varepsilon_{1,2} = \varepsilon_{1,2}(\varepsilon_\zeta)$ and $\varepsilon_{\zeta,1,2} = \varepsilon_{\zeta,1,2}(\varepsilon)$ for each time $\dot{t}$ from the table. The subscripts 1 and 2 in relations $\varepsilon_{1,2} = \varepsilon_{1,2}(\varepsilon_\zeta)$ refer to the lowest and highest ε values for stars whose ε_ζ fall in the interval $[\varepsilon_\zeta, \varepsilon_\zeta + \Delta\varepsilon_\zeta]$. The subscripts 1 and 2 in relations $\varepsilon_{\zeta,1,2} = \varepsilon_{\zeta,1,2}(\varepsilon)$ have an analogous meaning. Using the adopted notation, f_0 in (5) can be determined from the normalization condition for (5):

$$N = \iiint_S f(\varepsilon, \varepsilon_\zeta, l)\,d\varepsilon\,d\varepsilon_\zeta\,dl = f_0 \frac{\Psi(\beta)}{\beta\gamma} \int_{\varepsilon_{\min}}^{\varepsilon_{\max}} \exp(-\mu|\varepsilon - \bar{\varepsilon}|\,C(\gamma, \varepsilon))\,d\varepsilon, \quad (6)$$

where

$$\Psi(\beta) = 2 - \exp(-\beta(\dot{l} - l_{\min})) - \exp(-\beta(l_{\max} - \dot{l})),$$

$$C(\gamma, \varepsilon) = \exp(-\gamma(\varepsilon_{\zeta,1}(\varepsilon))) - \exp(-\gamma(\varepsilon_{\zeta,2}(\varepsilon))).$$

Parameters of the stellar distribution in $(\varepsilon, \varepsilon_\zeta, l)$ space averaged over P_r for model 2

Parameter	$\dot{t}/\tau_{vr}$						
	1.3	1.4	1.5	1.6	1.7	1.8	1.9
μ (Myr/pc)^2	4.155 ± .089	4.252 ± .087	4.326 ± .082	4.069 ± .079	3.944 ± .076	4.415 ± .083	3.692 ± .066
β (Myr/pc)^2	0.984 ± .020	0.977 ± .019	1.022 ± .019	0.995 ± .019	0.992 ± .018	1.050 ± .018	1.040 ± .018
γ (Myr/pc)^2	11.090 ± .227	11.143 ± .224	11.810 ± .220	11.177 ± .216	11.656 ± .227	13.049 ± .232	12.331 ± .234

The subscripts "min" and "max" in (6) indicate the minimum and maximum values in the domain S for ε and l. According to (5), the formulas for the stellar distribution in $(\varepsilon, \varepsilon_\zeta, l)$ space can be written in the form

$$\begin{aligned}
\chi(\varepsilon) &= \iint\limits_{(l,\,\varepsilon_\zeta)} f(\varepsilon, \varepsilon_\zeta, l)\,dl\,d\varepsilon_\zeta \\
&= f_0 \frac{\Psi(\beta)}{\beta\gamma} C(\gamma, \varepsilon)\exp(-\mu|\varepsilon - \bar{\varepsilon}|), \\
\psi(l) &= \iint\limits_{(\varepsilon,\,\varepsilon_\zeta)} f(\varepsilon, \varepsilon_\zeta, l)\,d\varepsilon\,d\varepsilon_\zeta \\
&= f_0 \frac{\exp(-\beta|l - \bar{l}|)}{\gamma} \int\limits_{\varepsilon_{\min}}^{\varepsilon_{\max}} \exp(-\mu|\varepsilon - \bar{\varepsilon}|) C(\gamma, \varepsilon)\,d\varepsilon, \\
\omega(\varepsilon_\zeta) &= \iint\limits_{(\varepsilon,\,l)} f(\varepsilon, \varepsilon_\zeta, l)\,d\varepsilon\,dl \\
&= f_0 \frac{\Psi(\beta)}{\beta\mu} K(\mu, \varepsilon_\zeta)\exp(-\gamma\varepsilon_\zeta),
\end{aligned} \tag{7}$$

where $K(\mu, \varepsilon_\zeta) = 2 - \exp(-\mu|\bar{\varepsilon} - \varepsilon_1(\varepsilon_\zeta)|) - \exp(-\mu|\varepsilon_2(\varepsilon_\zeta) - \bar{\varepsilon}|)$ and (l, ε_ζ), $(\varepsilon, \varepsilon_\zeta)$, and (ε, l) refer to the domains for the quantities in parentheses occupied by the stars in the combined file containing stellar phase-space coordinates for seven equidistant times in the period P_r.

On the whole, formulas (7) for $\omega(\varepsilon_\zeta)$ and $\psi(l)$ with the parameters of the distribution (5) given in the table describe the ε_ζ and l distributions of the cluster stars averaged over P_r fairly well (see Figs. 6b, 6c). $\chi(\varepsilon)$ fits the ε distribution somewhat worse (see Fig. 6a), due to the fact that the cluster includes two subsystems (core and halo) with different $\bar{\varepsilon}$ values (see above for a possible way to refine $\chi(\varepsilon)$).

To study the properties of the phase-space density function that forms in cluster model 2 as a result of its violent relaxation, we compared the $(\dot{\xi}, \dot{\eta}, \dot{\zeta})$ stellar velocity distribution averaged over P_r with the corresponding instantaneous distributions for each of the seven equally spaced times t_i in each of the 10 distance intervals Δr_j and for each of the intervals $0 \le r \le r_j$, where $r_j = \sum_{k=1}^{j} \Delta r_k$, $j = 1, \ldots, 10$. We also performed an analogous comparison of the averaged $(\varepsilon, \varepsilon_\zeta, l)$ distribution of the cluster stars and the corresponding instantaneous distributions. We used the Kolmogorov criterion in the comparisons; see [9] for a description of the technique used. We computed for each time $t_i \in P_r$ the probabilities $P(r \in \Delta r_j)$ that the differences in the stellar parameters considered [$(\dot{\xi}, \dot{\eta}, \dot{\zeta})$ or $(\varepsilon, \varepsilon_\zeta, l)$] for the distance interval $r \in \Delta r_j$ (i.e., $r \in [r_{j-1}, r_j]$, where $r_0 = 0$) were purely random and that the corresponding samples of stellar parameters are drawn from the same population. We also computed the probabilities $\bar{P}(r \in \Delta r_j)$ and dispersions $\sigma_{\bar{P}}(r \in \Delta r_j)$ for the deviations of $P(r \in \Delta r_j)$ from $\bar{P}(r \in \Delta r_j)$ averaged over the seven times $t_i \in P_r$. We performed analogous computations for stars at distances $r \le r_j$, $j = 1, \ldots, 10$. We will denote the computed probabilities and their dispersions $P(r \le r_j)$ and $\sigma_{\bar{P}}(r \le r_j)$.

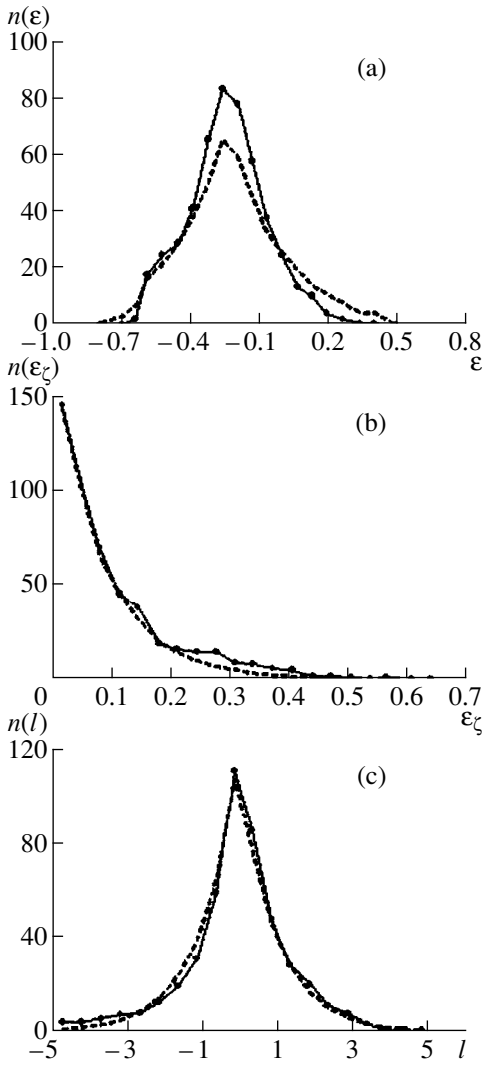

Fig. 6. The $n(\varepsilon)$, $n(\varepsilon_\zeta)$, and $n(l)$ distributions of the cluster stars averaged over P_r at time $t = 1.3\tau_{vr}$ for model 2 (solid curves). The dashed curves show the $\chi(\varepsilon)$, $\omega(\varepsilon_\zeta)$, and $\psi(l)$ distributions for time $t = 1.3\tau_{vr}$ computed in accordance with formulas (7) and the data from the table.

Let us first consider the comparison of the $(\varepsilon, \varepsilon_\zeta, l)$ stellar distribution averaged over P_r and the corresponding instantaneous distributions. The probabilities $P(r \le r_j)$ in the cluster (i.e., at $r \le R_t^-$, see below) increase with j and distance, from $\bar{P}(r \le r_1) \simeq 0.55$–$0.65$ to

$\bar{P}(r \le R_t^-) \simeq 0.85$–$0.95$, for all times in the table. In this case, the characteristic $\sigma_{\bar{P}}(r \le r_j)$ are equal to 0.05–0.06. Here, R_t^- and R_t^+ denote the tidal radii of the cluster for stars with "retrograde" and "prograde" motions, respectively, when the star's angular-velocity vector with respect to the ζ axis is opposite or parallel to the angular-velocity vector of the cluster with respect to the Z axis of the Galactic rotation. The technique we used to estimate R_t^- and R_t^+ from the distance dependences of the squares of the velocities and velocity dispersions for stars with prograde and retrograde cluster orbits is described in [7]. In our models, $R_t^- \simeq 2R_t^+$.

Thus, the (ε, ε_ζ, l) distributions of the cluster stars averaged over P_r are statistically indistinguishable from the corresponding instantaneous distributions, and the probability that the differences between these two distributions are purely random for all times t_i considered is $\bar{P}(r \le R_t^-) \simeq 0.85$–$0.95$.

The probabilities $\bar{P}(r \in \Delta r_j)$ for times $\dot{t} = (1.3\text{–}1.5)\tau_{vr}$ increase with distance, from $\bar{P}(r \in \Delta r_1) \simeq 0.55$–$0.65$ to $\bar{P}(r \in \Delta r_3) \simeq 0.90$; further, they decrease to 0.65–0.75 near $r \simeq R_t^+$, increase to 0.85–0.94 near $r \simeq R_t^-$, and finally decrease to $\bar{P}(r \in \Delta r_{10}) \simeq 0.5$. $\bar{P}(r \in \Delta r_j) \simeq 0.60$–$0.65$ at $\dot{t} > 1.5 \times \tau_{vr}$. They remain approximately constant at $r < R_t^+$, increase with r in the interval $R_t^+ < r < R_t^-$, reaching 0.85 at $r \simeq R_t^-$, and then decrease to $\simeq 0.5$ in the interval $r \in \Delta r_{10}$. The $\sigma_{\bar{P}}(r \in \Delta r_j)$ values are equal to 0.04–0.05 inside the cluster and increase to $\simeq 0.1$ at $r > R_t^-$.

It follows that, for all Δr_j intervals inside the cluster, the (ε, ε_ζ, l) distributions of the cluster stars averaged over P_r are statistically equivalent to the corresponding instantaneous distributions with probability $\bar{P}(r \in \Delta r_j) \simeq 0.6$–$0.9$; i.e., this is the probability that the differences between the distributions can be attributed to random fluctuations for all times t_i in the period P_r.

Let us consider the comparison of the averaged ($\dot{\xi}$, $\dot{\eta}$, $\dot{\zeta}$) stellar velocity distribution and the corresponding instantaneous distributions. For all times $\dot{t}$ in the table, the probabilities $\bar{P}(r \le r_j)$ primarily decrease with distance, from $\bar{P}(r \le r_1) \simeq 0.85$ to $\bar{P}(r \le R_t^-) \simeq 0.65$, or decrease from $\bar{P}(r \le r_1) \simeq 0.75$–$0.85$ to 0.61–0.65 and then increase to $\bar{P}(r \le R_t^-) \simeq 0.75$. The typical dispersions $\sigma_{\bar{P}}(r \le r_j)$ are equal to 0.05–0.07. It follows that, considering the entire cluster, the probability that the ($\dot{\xi}$, $\dot{\eta}$, $\dot{\zeta}$) stellar velocity distribution averaged over P_r and the corresponding instantaneous distributions can be considered statistically equivalent is $\bar{P}(r \le R_t^-) \simeq 0.65$–$0.75$ [which is lower than the corresponding probability for the (ε, ε_ζ, l) distribution], while the differences between them in velocity space can be considered to be random with the same probability for all the times t_i in the period P_r. Indeed, the instantaneous distributions of the velocity magnitudes for cluster model 2 in Fig. 5 differ more from the average distribution than the instantaneous (ε, ε_ζ, l) distributions differ from the corresponding average distributions in Fig. 4.

At times $\dot{t} = (1.3\text{–}1.5)\tau_{vr}$, the probabilities $\bar{P}(r \in \Delta r_j)$ decrease with distance, from $\bar{P}(r \in \Delta r_1) \simeq 0.75$–$0.85$ at the cluster center to $\simeq 0.38$–0.40 at the cluster periphery. At $\dot{t} \ge 1.8 \times \tau_{vr}$, two regions with low probability $\bar{P}(r \in \Delta r_j) \simeq 0.51$–$0.53$ form in the cluster, near $r \simeq R_t^+$ and $r \simeq R_t^-$. $\bar{P}(r \in \Delta r_1)$ remains high and is equal to $\simeq 0.85$. The dispersions $\sigma_{\bar{P}}(r \in \Delta r_j)$ inside the cluster are 0.04–0.10 in this case.

Note that, near the cluster center, $\bar{P}(r \in \Delta r_1)$ and $\bar{P}(r \le r_1)$ are substantially lower for the distribution of stellar coordinates (ε, ε_ζ, l) than for the distribution of stellar velocities ($\dot{\xi}$, $\dot{\eta}$, $\dot{\zeta}$). This is due to the following specific features of the stellar distributions in (ε, ε_ζ, l) and ($\dot{\xi}$, $\dot{\eta}$, $\dot{\zeta}$) space. The distribution of ε near the cluster center differs appreciably from any of the ε distributions for the cluster stars in Fig. 4a, since it has a maximum near $\varepsilon \simeq -0.56$ and contains a large fraction of stars with small $\varepsilon < -0.5$. According to Fig. 1, the mean $\langle\varepsilon\rangle$ for stars in this ε domain exhibit appreciable periodic oscillations, which result in substantial variations of the ε distribution for stars near the cluster center during the period P_r. The distribution of the stellar velocity magnitudes near the cluster center has a maximum near $|\mathbf{v}| \simeq 0.38$–0.40 km s^{-1} and has only a comparatively small number of stars with $|\mathbf{v}| > 0.7$ km s^{-1}, where periodic oscillations of $\langle|\mathbf{v}|\rangle$ become appreciable. Therefore, the stellar velocity distribution near the cluster center undergoes much weaker variations over the period P_r than does the ε distribution of the cluster stars; this is reflected in the comparisons of the (ε, ε_ζ, l) and ($\dot{\xi}$, $\dot{\eta}$, $\dot{\zeta}$) distributions of the cluster stars averaged over P_r and the corresponding instantaneous distributions (see above).

The largest changes of the stellar velocity distribution over the period P_r at $\dot{t} = (1.3\text{–}1.5)\tau_{vr}$ take place at the cluster periphery, in the distance interval $R_t^+ < r < R_t^-$ [where $\bar{P}(r \in \Delta r_j) \simeq 0.38$–$0.40$]; this separates in the course of the cluster's evolution at $\dot{t} > 1.6 \times \tau_{vr}$ into two regions with low $\bar{P}(r \in \Delta r_j) \simeq 0.5$ and appreciable temporal variations of the velocity distribution near the tidal boundaries of the cluster at $r \simeq R_t^+$ and $r \simeq R_t^-$.

The deviations of the instantaneous phase-space densities from the phase-space density of the cluster model averaged over P_r corresponding to these temporal variations of the stellar velocity distributions are due to the departure of the cluster model from virial equilibrium and nonstationarity of the cluster in the regular field. The most important temporal variations of the stellar distributions in $(\varepsilon, \varepsilon_\zeta, l)$ space over the period P_r occur near the cluster center and near $r \simeq R_t^+$. However, even here, the probabilities $\bar{P}(r \in \Delta r_j)$ are equal to 0.55–0.75; i.e., they are fairly high. Thus, this is the probability that the differences between the instantaneous distributions of the cluster stars in $(\varepsilon, \varepsilon_\zeta, l)$ space and the corresponding distributions averaged over P_r are purely random.

According to Fig. 4 and the results of our statistical comparison of the stellar distribution in $(\varepsilon, \varepsilon_\zeta, l)$ space averaged over P_r and the corresponding instantaneous distributions, the distribution (5) with the parameters given in the table are statistically indistinguishable from the equilibrium distribution that develops in cluster model 2, which is nonstationary in the regular field. The linear form

$$\Theta = \Theta(\mathbf{r}, \mathbf{v}) = -\mu|\varepsilon - \bar{\varepsilon}| - \beta|l - \bar{l}| - \gamma\varepsilon_\zeta \qquad (8)$$

for $(\varepsilon, \varepsilon_\zeta, l)$ in (5) is also constant over the period P_r and varies only slightly over a time interval $\sim 2\tau_{vr}$. We now fix the coordinates of the vectors **r** and **v**. If Θ = const, periodic variations of the cluster potential $U(\mathbf{r})$ at the point **r** should produce oscillations (with period P_r) in the stellar distribution function, which are detected via appreciable changes in the magnitudes of the stellar velocities over the period P_r (Fig. 5).

5. CONCLUSIONS

(1) The open-cluster models considered in this paper develop an equilibrium stellar distribution in $(\varepsilon, \varepsilon_\zeta, l)$ space over a time $t \simeq \tau_{vr}$, which varies slowly at $t > \tau_{vr}$. The equilibrium in $(\varepsilon, \varepsilon_\zeta, l)$ space develops as a result of relaxation in the absence of virial equilibrium. The equilibrium distribution function $f(\varepsilon, \varepsilon_\zeta, l)$ for the stars in the cluster models considered can be written $f(\varepsilon, \varepsilon_\zeta, l) \sim \exp(\Theta)$, where Θ is a linear form for the variables $(\varepsilon, \varepsilon_\zeta, l)$, whose coefficients vary only slightly over a time interval $\sim 2\tau_{vr}$. The equilibrium stellar phase-space distribution function $F_0(\mathbf{r}, \mathbf{v})$ corresponding to the equilibrium in $(\varepsilon, \varepsilon_\zeta, l)$ space and the regular cluster potential vary periodically (or quasi-periodically) with time. This equilibrium is probably possible due to an approximate balance of the stellar transitions between phase-space cells over time intervals equal to the oscillation period for the regular cluster field.

(2) The local time for cluster relaxation toward the equilibrium state is $t_r \simeq 0.5 \times \tau_{vr}$ in the central regions of both cluster models considered and $t_r \simeq 1.1 \times \tau_{vr}$ and $t_r \simeq 1.5 \times \tau_{vr}$ at the peripheries of models 1 and 2, respectively.

(3) At $t > \tau_{vr}$, the $\langle\varepsilon\rangle$, $\langle\varepsilon_\zeta\rangle$, and $\langle l\rangle$ values averaged over several stars in intervals of ε, ε_ζ, and l remain approximately constant over most of the domain S of $(\varepsilon, \varepsilon_\zeta, l)$ space occupied by cluster stars at distances $r \leq R_t^-$. Near the boundaries of and outside S, both the number of stars and the stellar density are small, and $\langle\varepsilon\rangle$, $\langle\varepsilon_\zeta\rangle$, and $\langle l\rangle$ are not constant in time. In the cluster models considered, the dispersions σ_ε, $\sigma_{\varepsilon,\zeta}$, and σ_l of the deviations of ε, ε_ζ, and l from the corresponding average values $\langle\varepsilon\rangle$, $\langle\varepsilon_\zeta\rangle$, and $\langle l\rangle$ for stars occupying the $(\varepsilon, \varepsilon_\zeta, l)$ intervals determined above have small (and probably random) oscillations about certain constant values throughout most of S at $t > \tau_{vr}$. σ_ε and σ_l can vary appreciably with time near the boundaries of and outside S. The approximate constancy of the $(\langle\varepsilon\rangle, \langle\varepsilon_\zeta\rangle, \langle l\rangle)$ and $(\sigma_\varepsilon, \sigma_{\varepsilon,\zeta}, \sigma_l)$ values for stars in the domain S of $(\varepsilon, \varepsilon_\zeta, l)$ space at $t > \tau_{vr}$ indicates the formation of an equilibrium stellar distribution function $f(\varepsilon, \varepsilon_\zeta, l)$ in the cluster.

(4) At $t_i > \tau_{vr}$, the probability that the instantaneous distribution function for the cluster stars in $(\varepsilon, \varepsilon_\zeta, l)$ space is statistically indistinguishable from the corresponding distribution function averaged over the period P_r for oscillations of the regular cluster field at all times t_i and in all distance intervals Δr_j is $P(r \in \Delta r_j) \simeq 0.6$–$0.9$. In other words, this is the probability that the differences between the stellar distributions in $(\varepsilon, \varepsilon_\zeta, l)$ space averaged over P_r and the corresponding instantaneous stellar distributions are random in all distance intervals Δr_j considered ($r \leq R_t^-$). On the whole, the stellar distribution function in $(\varepsilon, \varepsilon_\zeta, l)$ space for the entire cluster averaged over P_r is statistically indistinguishable from the corresponding instantaneous distributions with probability $P(r \leq R_t^-) \simeq 0.85$–$0.95$, while the differences between them are random with the same probability for all the times t_i considered in the period P_r. Our technique for computing a cluster-model distribution function in $(\varepsilon, \varepsilon_\zeta, l)$ space averaged over P_r can be used to determine the equilibrium stellar distribution function $f(\varepsilon, \varepsilon_\zeta, l)$ at the central time of the period P_r.

(5) The instantaneous and averaged stellar distributions in velocity space are statistically indistinguishable with probability $P(r \leq R_t^-) \simeq 0.65$–$0.75$ [i.e., somewhat lower than for the $(\varepsilon, \varepsilon_\zeta, l)$-space distribution]. In the distance interval $R_t^+ \leq r \leq R_t^-$ at $t = (1.3\text{–}1.5) \times \tau_{vr}$ and near the tidal boundaries of the cluster $r = R_t^\pm$ at $t > 1.6 \times \tau_{vr}$, the probability that the instantaneous stellar velocity distributions and the corresponding averaged distributions are statistically indistinguishable (i.e., differ only randomly) is only $P(r \in \Delta r_j) \simeq 0.4$–$0.5$ for all times t_i in the period P_r. The temporal variations of the instantaneous phase-space density of the cluster stars over P_r are due primarily to deviations from the stellar phase-space density functions averaged over P_r at the cluster

periphery and near the tidal boundaries of the cluster. The oscillations of the phase-space density for cluster stars about the averaged phase-space density are due to the absence of virial equilibrium in the cluster and its nonstationarity in the regular field.

ACKNOWLEDGMENTS

This work was supported by the Ministry of Science of the Russian Federation (the "Astronomy" State Science and Technology program).

REFERENCES

1. V. M. Danilov, Astron. Zh. **76**, 93 (1999).
2. H. E. Kandrup, M. E. Mahon, and H. Smith, Jr., Astron. Astrophys. **271**, 440 (1993).
3. H. E. Kandrup, Astrophys. J. **500**, 120 (1998).
4. S. Chandrasekhar, *Principles of Stellar Dynamics* (Univ. Chicago Press, Chicago, 1942; Inostrannaya Literatura, Moscow, 1948).
5. D. Lynden-Bell, Mon. Not. R. Astron. Soc. **136**, 101 (1967).
6. W. C. Saslaw, *Gravitational Physics of Stellar and Galactic Systems* (Cambridge Univ. Press, Cambridge, 1985; Mir, Moscow, 1989).
7. V. M. Danilov, Astron. Zh. **74**, 188 (1997).
8. S. A. Kutuzov and L. P. Osipkov, Astron. Zh. **57**, 28 (1980).
9. V. M. Danilov, Pis'ma Astron. Zh. **23**, 365 (1997).
10. I. R. King, Astrophys. J. **67**, 471 (1962).
11. D. W. Marquardt, J. Soc. Indust. Appl. Math. **11**, 431 (1963).

Translated by A. Dambis

Astronomy Reports, Vol. 44, No. 5, 2000, pp. 309–322. Translated from Astronomicheskiĭ Zhurnal, Vol. 77, No. 5, 2000, pp. 357–372.

Nonconservative Evolution of Cataclysmic Binaries

A. V. Fedorova[1], D. V. Bisikalo[1], A. A. Boyarchuk[1], O. A. Kuznetsov[2], A. V. Tutukov[1], and L. R. Yungel'son[1]

[1]*Institute of Astronomy, Russian Academy of Sciences, ul. Pyatnitskaya 48, Moscow, 109017 Russia*

[2]*Keldysh Institute of Applied Mathematics, Russian Academy of Sciences, Miusskaya pl. 4, Moscow, 125047 Russia*

Received May 5, 1999

Abstract—We present a mechanism to take into account angular-momentum loss in binary systems with nonconservative mass transfer. In a number of cases, mass loss in the system can increase the orbital angular momentum of the stars. Including this mechanism in evolutionary models substantially expands the domain of stable mass transfer in binary systems. All observed cataclysmic binaries with known component masses fall within the calculated area for stable mass transfer. © *2000 MAIK "Nauka/Interperiodica".*

1. INTRODUCTION

Cataclysmic variable stars are close binary systems consisting of a low-mass main-sequence star that fills its Roche lobe and a white dwarf. The main sequence star (donor) loses matter through the region surrounding the inner Lagrangian point L_1. The white dwarf (accretor) accretes at least some of this matter via an accretion disk or accretion columns in polar areas (provided the white dwarf possesses a strong magnetic field).

The physics and evolution of cataclysmic binaries (and of low-mass X-ray systems, whose evolution is similar) have been actively studied since the end of the 1960s (see, for example, [1–10] and references therein). Theoretical studies of cataclysmic binaries have been driven by the fact that their evolution is determined by orbital angular momentum loss via gravitational-wave radiation [11, 12] and magnetic stellar wind [13–16]. A number of studies (see, for example, [17–19]) have considered the effect of angular-momentum loss due to matter outflow from the system over the course of a cataclysmic binary's evolution, as well as redistribution of momentum between the components and accretion disk. However, in the absence of gas dynamical calculations of mass transfer in binary systems, it was necessary to study these processes in parametric approximations.

Recent three-dimensional gas dynamical calculations of gas flows in cataclysmic binaries (see, for instance, [20, 21]) have shown that, in the course of mass transfer, an intercomponent envelope is formed around the binary, and a considerable fraction of the matter lost by the donor leaves the system. In the present study, we perform a numerical analysis of the evolution of cataclysmic binaries taking into account the results of these three-dimensional gas dynamical calculations. In accordance with these results, in our model for the evolution of a cataclysmic binary, we take into account the loss of mass and angular momentum by the system during mass transfer.

We pay special attention to the stability of the mass transfer for various values of the donor mass M_2 and donor-to-accretor mass ratio $q = M_2/M_1$. It is known that mass loss from a star results in violation of its hydrostatic and thermal equilibrium. Hydrostatic equilibrium is reestablished adiabatically over the dynamical time scale, while thermal equilibrium is reestablished over the Kelvin time scale. The reestablishment of the star's equilibrium is accompanied by variations in its radius, which depend on the convective or radial stability of the outer envelope. For stars with mass $M \lesssim M_\odot$ and a deep convective zone, and also for white dwarfs, mass loss is accompanied by an increase of the star's radius, while, for stars with radiative envelopes, mass loss results in contraction. The mass transfer in a close binary system is unstable if, in the course of evolution, the donor consistently tends to expand beyond its Roche lobe. This occurs when the radius of the donor R_2 increases more rapidly (or decreases more slowly) than does the average radius of the Roche lobe.[1] It is also possible for the radius of the donor to increase while that of the Roche lobe decreases. Thus, the situation is determined by the ratio of the derivatives of the donor radius $\partial R_2/\partial M_2$ and the average Roche-lobe radius $\partial R_{RL}/\partial M_2$, which admits the possibility of unstable mass transfer even for stars that contract as they lose mass.

Refining our understanding of the conditions for stable mass transfer has two interconnected objectives:

[1] The average radius of the Roche lobe is defined to be the radius of the sphere whose volume is equal to that of the Roche lobe.

1063-7729/00/4405-0309$20.00 © 2000 MAIK "Nauka/Interperiodica"

(a) To understand the 10% of cataclysmic binaries with known component masses for which any combination of M_2 and q should make stable mass transfer impossible under the standard assumptions about variations of the system's angular momentum.

(b) To understand which detached systems consisting of a white dwarf and low-mass secondary can become cataclysmic binaries at the beginning of their evolution (i.e., for which of these systems stable mass transfer is possible), which is essential for modeling of the cataclysmic-binary population. A similar problem also arises, for example, in studies of low-mass X-ray binaries.

In Section 2, we describe the main factors determining the evolution of cataclysmic binaries and the conditions for stable mass transfer in binary systems. Reasons to abandon conservative approximations are considered in Section 3. In Sections 4 and 5, we present a model for the angular-momentum loss due to the nonconservative character of the mass transfer, based on three-dimensional gas dynamical calculations of matter flows in semidetached binary systems. In Section 6, we compare the results of calculations made for conservative and nonconservative evolutionary models. The conditions for stable mass transfer in an evolutionary model that is nonconservative with respect to mass and angular momentum are determined in Section 7.

2. MAIN FACTORS DETERMINING THE EVOLUTION OF CATACLYSMIC BINARIES

In the present study, we consider dynamically stable mass transfer; i.e., we assume that, during mass transfer, the state of the star can differ appreciably from thermal equilibrium and the mass-transfer rate can exceed appreciably a rate corresponding to the Kelvin time scale ($\dot{M} \simeq 3\times 10^{-7}\, RL/M \;\; M_\odot\ \mathrm{yr}^{-1}$, with the radius R, luminosity L, and mass M of the star in solar units). We take the mass transfer to be unstable when the rate of variation of the donor radius exceeds that for the effective radius of the Roche lobe: $\dot{R}_2 > \dot{R}_{\mathrm{RL}}$. Using the derivatives of radius with respect to the donor mass M_2, we can formulate the mass-transfer stability condition

$$\zeta_* = \frac{\partial \ln R_2}{\partial \ln M_2} > \frac{\partial \ln R_{\mathrm{RL}}}{\partial \ln M_2} = \zeta_{\mathrm{RL}}. \qquad (1)$$

The average radius of the donor Roche lobe can be estimated, for example, using the interpolation formula of Eggleton [22]:

$$R_{\mathrm{RL}} \approx 0.49A\frac{q^{2/3}}{0.6q^{2/3} + \ln(1+q^{1/3})},$$

where A is the semimajor axis of the orbit. For $q \lesssim 1$, the approximation of Paczynski [23] is more convenient:

$$R_{\mathrm{RL}} \approx \frac{2}{3^{4/3}}A\left(\frac{q}{1+q}\right)^{1/3}. \qquad (2)$$

The derivative of the Roche lobe radius can be expressed

$$\frac{\partial \ln R_{\mathrm{RL}}}{\partial \ln M_2} = \frac{\partial \ln A}{\partial \ln M_2} + \frac{\partial \ln (R_{\mathrm{RL}}/A)}{\partial \ln M_2}. \qquad (3)$$

We can see from (2) and (3) that the variation of the average Roche-lobe radius as a function of the decrease of the donor mass is determined by the variations of the masses of the donor and accretor and the distance between them, i.e., on the mass and angular momentum lost from the system. As a rule, only the orbital angular momentum of the system has been considered; i.e., the angular momentum is taken to be the sum of the angular momenta of the two stars, which are treated as material points. Consequently, the angular momenta of the axial rotation of the components, of the accretion disk (if it exists), and of matter streams in the system are usually not included in the total angular momentum. The deviation of the donor's angular momentum from that of a point, which can be substantial, is not taken into consideration [24]. This approach has been necessitated by the extreme difficulty of taking all these factors into account in calculations. In the simplified case we consider here, the orbital angular momentum of a binary system with a circular orbit is

$$J = G^{1/2}A^{1/2}\frac{M_1M_2}{(M_1+M_2)^{1/2}}, \qquad (4)$$

where G is the gravitational constant.

It is currently widely believed that the evolution of cataclysmic binaries is determined by the loss of momentum from the system via gravitational-wave radiation (GWR) and/or a magnetic stellar wind (MSW) from the donor, as well as via the transfer of mass between the components. The standard model of close-binary evolution supposes that the mass transfer itself does not affect the momentum of the system and that its influence is only indirect, via possible mass loss from the system and carrying away of angular momentum with the outflowing matter. Therefore, the variation of the system's orbital angular momentum can be written

$$\frac{dJ}{dt} = \left(\frac{\partial J}{\partial t}\right)_{\mathrm{GWR}} + \left(\frac{\partial J}{\partial t}\right)_{\mathrm{MSW}} + \left(\frac{\partial J}{\partial t}\right)_{\mathrm{loss}}. \qquad (5)$$

Let us consider the various components of (5).

(1) *Angular Momentum Loss from the System via GWR*

The variations of the system's orbital angular momentum due to the radiation of gravitational waves can be written [25]

$$\left(\frac{\partial \ln J}{\partial t}\right)_{\mathrm{GWR}} = -\frac{32}{5}\frac{G^3}{c^5}\frac{M_1M_2(M_1+M_2)}{A^4}, \qquad (6)$$

where c is the speed of light. One characteristic feature of GWR is the very strong dependence of its intensity on the orbital semimajor axis and, accordingly, on the orbital period. GWR is substantial for short-period systems with orbital periods $P_{orb} \lesssim 10^{\mathrm{h}}$, since only in this

case does the characteristic time for momentum loss become shorter than the age of the Universe.

(2) *Angular Momentum Loss from the System via a MSW from the Donor*

A mechanism for angular momentum loss via a MSW from the donor was suggested in [13, 14]. If the donor possesses a convective envelope and, accordingly, a surface magnetic field, its intrinsic axial rotation is inhibited by the magnetic stellar wind, and the angular-momentum loss rate can be appreciable even when the mass loss rate is small. The subsequent synchronization of the donor axial rotation and the orbital rotation, due to tidal interactions between the components, results in a loss of orbital angular momentum from the system and the decrease of A. A semiempirical formula from [16], which is based on extrapolation of the dependence of rotation velocity on age for G main sequence stars found by Skumanich [26] to the K and M components of cataclysmic binaries is most frequently used to take this effect into account. The decrease of orbital angular momentum as a function of time given by this relation is

$$\left(\frac{\partial \ln J}{\partial t}\right)_{\rm MSW} = -0.5\times 10^{-28} k^2 C G \frac{(M_1+M_2)^2}{M_1}\frac{R_2^4}{A^5}. \quad (7)$$

Here, k is the gyroradius of the donor and C is a coefficient determined by comparing theoretical calculations with observations. Based on the observed magnetic-field decay for stars with masses smaller than $\sim 0.3M_\odot$, Spruit and Ritter [27] proposed that the total mixing that occurs in these stars when their masses decrease to this limit results in an abrupt "switch off" of the dynamo mechanism responsible for the generation of the stellar magnetic field. At that time, the time scale for angular-momentum loss determined by equation (7) is shorter than the thermal time scale for a star with mass $\sim 0.3M_\odot$, and the star is no longer in thermal equilibrium. In this case, the star's radius exceeds the radius of a star with the same mass in thermal equilibrium.[2] When the action of the MSW carrying away angular momentum from the system terminates, the rate of decrease of the orbital semimajor axis slows, the donor-star radius decreases to its equilibrium value, and the star shrinks within its Roche-lobe surface [27]. Since the binary continues to lose angular momentum via GWR, its components continue to approach each other slowly and, after some time, the main-sequence star again fills its Roche lobe. The further evolution of the system is determined by the loss of angular momentum via GWR.

It is currently thought that termination of the MSW after total mixing of the donor-star material can explain the so-called gap in the observed orbital periods of cataclysmic binaries. The theoretical width of this gap compared to its observed value determines the choice of the coefficient C in (7). In accordance with the results of [7], we adopted $C = 3.0$.

(3) *Angular-Momentum Loss by the System During Matter Outflow*

As a rule, the possibility of mass loss from the system has been treated as a parameter in theoretical studies of the evolution of cataclysmic binaries and related systems; for example, this parameter could be varied in order to reach consistency with observational estimates of the cataclysmic-binary minimum period [1]. More specific assumptions about the evolution of the system were made only in the following cases.

(a) The rate of capture of matter by the accretor (a white dwarf) is limited by the rate of hydrogen burning ($\sim 10^{-7}$–$10^{-6}\ M_\odot$/yr), while the donor mass-loss rate appreciably exceeds this limit, not exceeding, however, the Eddington limit for the dwarf, which is close to $1.5\times 10^{-5}\ M_\odot$/yr (see, for example, [28, 29]). The excess matter can be lost via stellar wind [30].

(b) Matter is lost in flares on the white dwarf (see, for example, [17, 31–33]).[3] In both cases, it is usually assumed that the specific momentum of the matter flowing from the system is equal to the specific momentum of the accretor.

To describe mass and angular-momentum loss from the system, it is convenient to use parameters characterizing the degree of nonconservation with respect to mass [34]

$$\beta = -\frac{\dot M_1}{\dot M_2} = -\frac{\partial M_1}{\partial M_2}$$

and angular momentum:[4]

$$\psi = \frac{\dot J}{\dot M}\Big/\frac{J}{M} = \frac{\partial \ln J}{\partial \ln M}, \quad (8)$$

where $M = M_1 + M_2$.

In this case, the loss of angular momentum carried from the system by outflowing matter assumes the form

$$\left(\frac{\partial J}{\partial t}\right)_{\rm loss} = (1-\beta)\dot M_2 \psi \frac{J}{M}.$$

In cataclysmic-binary evolution calculations, an equation for the orbital semimajor axis as a function of time is used rather than the time dependence of the angular momentum of the system; the former equation can be derived from the latter. Let us differentiate expression (4) for the orbital angular momentum of the

[2] For a discussion of the reaction of stars to mass loss on various time scales see, for example, [5, 9].

[3] In the two last studies, the angular momentum loss due to interactions between the donor star and the envelope ejected by a nova was also considered.

[4] The specific ψ angular momentum carried from the system in ΩA^2 units, where Ω is the angular velocity of the orbital rotation, is sometimes used instead:

$$\alpha = \frac{\dot J}{\dot M}\Big/\Omega A^2 = \frac{\dot J}{\dot M}\Big/\frac{J}{\mu} = \frac{q}{(1+q)^2}\psi, \quad \mu = \frac{M_1 M_2}{M}.$$

system and substitute the result into (5), making use of the relation $\dot{M}_1 = -\beta\dot{M}_2$. Then, the variation of the orbital semimajor axis can be written

$$\left(\frac{dA}{dt}\right) = \left(\frac{\partial A}{\partial t}\right)_{\text{trans}} + \left(\frac{\partial A}{\partial t}\right)_{\text{loss}} + \left(\frac{\partial A}{\partial t}\right)_{\text{GWR}} + \left(\frac{\partial A}{\partial t}\right)_{\text{MSW}}. \quad (9)$$

Here, the subscript "trans" reflects variation of A as a result of mass transfer between the components. Note that, if there is no "trans" term $\left(\frac{\partial J}{\partial t}\right)_{\text{trans}}$ in (5), the corresponding term $\left(\frac{\partial A}{\partial t}\right)_{\text{trans}}$ term is present in equation (9), as naturally follows from the dependence of the orbital angular momentum on both the orbital semimajor axis and the mass of the components. For the case of conservative mass transfer (with respect to mass and angular momentum), variation of the orbital semimajor axis is determined by the assumption that the mass transfer does not affect the orbital angular momentum of the system. During the mass transfer, matter with specific angular momentum from the donor is carried to the accretor, and eventually acquires specific momentum from the accretor. If the orbital angular momentum is constant and the donor is less massive than the accretor, the excess angular momentum of the accreted matter should increase the orbital momentum, so that the mass transfer increases the semimajor axis of the orbit. If the donor is more massive, the deficit angular momentum of the accreted matter should be taken from the orbital angular momentum, so that the mass transfer decreases the semimajor axis.

In our modeling of the evolution of a cataclysmic binary, we simultaneously calculated the evolution of the donor and the time variation of the orbital semimajor axis of the binary. We did not take into account the evolution of the accretor, except for variations in its mass. Let us consider the parameters determining the time evolution of the semimajor axis. Using the parameters β and ψ, we derive formulas for the components of equation (9), where mass is given in $M_\odot$, distance in $R_\odot$, and time in years:

$$\left(\frac{\partial A}{\partial t}\right)_{\text{trans}} = 2A\frac{M_2 - M_1}{M_1 M_2}\beta\dot{M}_2. \quad (10)$$

$$\left(\frac{\partial A}{\partial t}\right)_{\text{loss}} = -(1-\beta)A\frac{2M_1(1-q\psi) + M_2}{M_2(M_1+M_2)}M_2. \quad (11)$$

$$\left(\frac{\partial A}{\partial t}\right)_{\text{GWR}} = -1.65\times 10^{-9}\frac{M_1 M_2 (M_1+M_2)}{A^3}, \quad (12)$$

$$\left(\frac{\partial A}{\partial t}\right)_{\text{MSW}} = -6.06\times 10^{-7} C\frac{(M_1+M_2)^2}{M_1}\left(\frac{R_2}{A}\right)^4. \quad (13)$$

As we can see from (10)–(13), the mass ratio q is one of the main parameters determining the variation of R_{RL}. Since the variation of R_2 depends on M_2 and $\dot{M}_2$, the "mass ratio q—donor mass M_2" diagram is useful for determining the boundaries of the domain of stable mass transfer.

In a number of cases, expression (3) can be simplified and analytical formulae for the derivative of the Roche lobe radius can be obtained. In particular, in the absence of angular-momentum loss due to GWR and MSW, we can obtain the dependence of the distance between the components [the first term in (3)] on their mass ratio and the parameters β and ψ from (10) and (11):

$$\frac{\partial \ln A}{\partial \ln M_2} = \frac{2\psi(1-\beta)q + q\beta + 2q^2\beta - q - 2}{1+q}. \quad (14)$$

For the second term (3), using (2), as suggested by Paczynski [23], we obtain for R_{RL}

$$\frac{\partial \ln (R_{\text{RL}}/A)}{\partial \ln M_2} = \frac{1}{3} - \frac{1}{3}\frac{q(1-\beta)}{1+q}. \quad (15)$$

From (14) and (15), we have for totally conservative mass transfer without mass and angular-momentum loss by the system ($\beta = 1$)

$$\frac{\partial \ln R_{\text{RL}}}{\partial \ln M_2} = 2q - \frac{5}{3}. \quad (16)$$

In so-called Jeans mass loss, there is no mass transfer in the system, but the donor loses matter via its stellar wind, which leaves the system, carrying away specific momentum from the donor ($\beta = 0$, $\psi = 1/q$). We obtain in this case

$$\frac{\partial \ln R_{\text{RL}}}{\partial \ln M_2} = \frac{\frac{1}{3} - q}{1+q}. \quad (17)$$

For the case of a stellar wind from the accretor, when all the matter lost by the donor flows onto the accretor but some later leaves the system, carrying away specific angular momentum from the accretor (here, we must formally adopt $\beta = 0$ and $\psi = q$), we have

$$\frac{\partial \ln R_{\text{RL}}}{\partial \ln M_2} = \frac{2q^2 - q - \frac{5}{3}}{1+q}. \quad (18)$$

At any stage of evolution, a comparison of the rates of variation of the radii of the donor and the Roche lobe (3) determines the type of mass transfer (i.e., stable or instable). There are two methods for determining the boundary of the domain of stable mass transfer. We can directly calculate the derivatives of the donor radius with respect to mass for various $\dot{M}_2$ and compare them with derivatives of the average radius of the Roche lobe, which depend on M_1, M_2, and A, as was done, for example, in [35]. In this way, we can delineate the area of the $q - M_2$ diagram in which mass transfer is dynamically stable and identify areas in which mass transfer should occur on various time scales: the Kelvin, nuclear,

or momentum-loss time scale. Alternatively, we can adopt as a condition for stable mass transfer that the accretion rate immediately after the donor Roche lobe is filled not to exceed the Eddington limit for dwarfs. This approach is justified by the fact that evolution calculations often yield very high mass-loss rates immediately after the Roche lobe filling, after which $\dot{M}$ decreases rapidly. In essence, this approach limits the dynamical stability of the mass transfer but makes it possible for the star to lose mass on the thermal time scale.

3. DOMAIN OF STABLE MASS TRANSFER IN A MASS-CONSERVATIVE CATACLYSMIC-BINARY MODEL

Figure 1 presents the boundaries for the domain of stable mass transfer determined using standard mass-conservative models for cataclysmic-binary evolution. Boundary *1* was found in [35], and boundary *2* was presented in [36]. These are in good agreement in the area of low donor masses but differ somewhat at large masses. Since the technique used to calculate this boundary was not described in [36], we can only suppose that these discrepancies result from differences in the codes used, the ways in which possible attenuation of the donor's MSW at masses exceeding $\sim 1 M_\odot$ was taken into account, and the methods used to calculate the derivative of the stellar radius in this area.

Figure 1 also plots cataclysmic binaries with known component masses from the catalog [37]. Among the 80 systems plotted, 11 cataclysmic binaries are in the domain of unstable mass transfer. For eight of these 11 systems, the errors are known and marked in Fig. 1 with bars. We can clearly see that the location of these stars in the domain of unstable mass transfer cannot be explained solely by the errors in the component masses. The cataclysmic binaries whose parameters Smith and Dhillon [38] consider to be most accurately determined are also indicated in Fig. 1. For a number of systems, refined mass values are given in [38], which are somewhat different from those in [37]. Nonetheless, even for these well-studied cataclysmic binaries, the situation remains unchanged: Three of 22 systems fall in the forbidden area.

To explain this result, we will consider a model for cataclysmic-binary evolution in which we assume mass and momentum loss from the system. This assumption is grounded in the results of our previous three-dimensional gas dynamical calculations of matter flows in close binary systems.

4. CALCULATION OF THE ANGULAR-MOMENTUM LOSS RATE IN THREE-DIMENSIONAL GAS DYNAMICAL MODELS

The above analysis shows that evolution calculations critically depend on two parameters: the degree of nonconservation of the mass transfer with respect to mass β and angular momentum ψ. These parameters can be estimated only through three-dimensional gas dynamical modeling of the mass transfer in cataclysmic binaries. Such studies have been made for binary systems with mass ratio $q = 1/5$ [20] and $q = 1$ [21]. In addition, to study the effect of q on the flow pattern, we made numerical simulations for a system with $q = 5$.

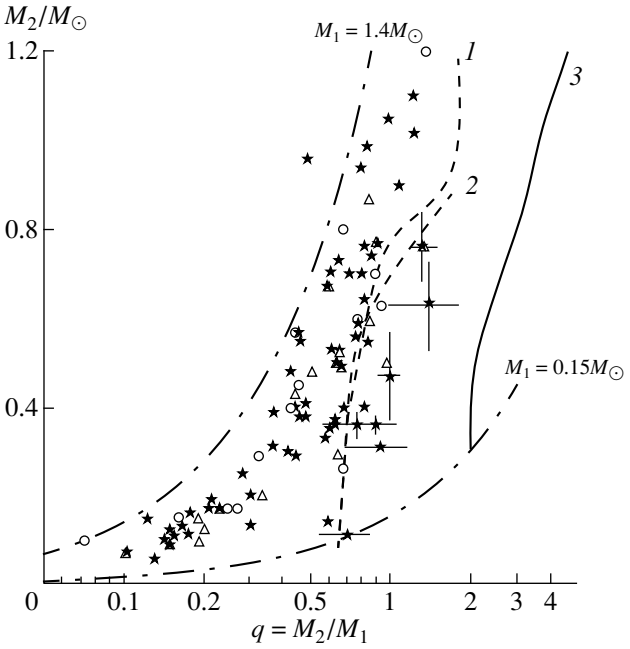

Fig. 1. Plot of donor-to-accretor mass ratio q versus donor mass M_2. Cataclysmic binaries from [37] are marked by asterisks and circles (the circles denote less reliable data). For some stars, errors are indicated. Cataclysmic binaries from [38] are marked with triangles. The dashed line *1* indicates the boundary of the domain of stable mass transfer according to [35], and the dashed line *2* shows the same boundary according to [36]. The solid line *3* delineates the domain of stable mass transfer derived in the present study. The dash–dot lines indicate the upper ($M_1 \lesssim 1.4\ M_\odot$) and lower ($M_1 \gtrsim 0.15\ M_\odot$) limits for the mass of the accretor, which is a white dwarf.

The calculations indicated that the mass transfer remains nonconservative for all q values, and the degree of nonconservation is $\beta \sim 0.4$–0.6. The typical flow patterns in three-dimensional numerical simulations also indicate that matter leaves the system with substantial angular momentum. However, determining the degree to which the mass transfer is nonconservative with respect to angular momentum proves to be more difficult. Let us consider the equations determining angular-momentum transfer in the system. Since viscosity plays an important role in redistributing angular momentum in the system, we must consider the Navier–Stokes equations. From the stationary gas dynamical equations for the x and y components of the velocity in a rotating coordinate system (here, $\mathbf{u} = (u, v, w)$

is the velocity vector, ρ the density, $\mathcal{P}$ the stress tensor, Φ the Roche potential, and Ω the orbital angular velocity)

$$u\frac{\partial u}{\partial x} + v\frac{\partial u}{\partial y} + w\frac{\partial u}{\partial z} + \frac{1}{\rho}\left(\frac{\partial \mathcal{P}_{xx}}{\partial x} + \frac{\partial \mathcal{P}_{xy}}{\partial y} + \frac{\partial \mathcal{P}_{xz}}{\partial z}\right) = -\frac{\partial \Phi}{\partial x} + 2\Omega v,$$

$$u\frac{\partial v}{\partial x} + v\frac{\partial v}{\partial y} + w\frac{\partial v}{\partial z} + \frac{1}{\rho}\left(\frac{\partial \mathcal{P}_{yx}}{\partial x} + \frac{\partial \mathcal{P}_{yy}}{\partial y} + \frac{\partial \mathcal{P}_{yz}}{\partial z}\right) = -\frac{\partial \Phi}{\partial y} - 2\Omega u,$$

we obtain the equation for angular-momentum transfer

$$u\frac{\partial \lambda}{\partial x} + v\frac{\partial \lambda}{\partial y} + w\frac{\partial \lambda}{\partial z} + \frac{1}{\rho}((\mathbf{r} - \mathbf{r}_{CM}) \times \mathrm{div}\mathcal{P})_z = -((\mathbf{r} - \mathbf{r}_{CM}) \times \mathrm{grad}\Phi)_z,$$

where $\mathbf{r}_{CM}$ is the radius vector for the center of mass of the system, and the angular momentum λ (in the laboratory coordinate frame) is determined by the expression

$$\lambda = (x - x_{CM})v - yu + \Omega((x - x_{CM})^2 + y^2)$$
$$= (x - x_{CM})(v + \Omega(x - x_{CM})) - y(u - \Omega y).$$

Let us write the equation for angular-momentum transfer in divergence form:

$$\mathrm{div}(\rho\lambda\mathbf{u}) + ((\mathbf{r} - \mathbf{r}_{CM}) \times \mathrm{div}\mathcal{P})_z = -\rho((\mathbf{r} - \mathbf{r}_{CM}) \times \mathrm{grad}\Phi)_z.$$

This yields an integral expression for variations in the angular momentum:

$$\int_\Sigma \rho\lambda\mathbf{u} \cdot d\mathbf{n} + \int_\Sigma ((\mathbf{r} - \mathbf{r}_{CM}) \times \mathcal{P}\, d\mathbf{n})_z = \int_V \rho((\mathbf{r} - \mathbf{r}_{CM}) \times \mathrm{grad}\Phi)_z dV = \Pi.$$

The value of Π describes angular-momentum variation due to the noncentral character of the force field determined by the Roche potential. The quantity

$$\mathbf{F} = \rho\lambda\mathbf{u} + \mathcal{P}\mathbf{r}' \quad (\mathbf{r}' = (-y, x - x_{CM}, 0)) \qquad (19)$$

represents the angular-momentum flux density λ. As a result, we obtain for the stationary case

$$-\int_{\Sigma_1} \mathbf{F} \cdot d\mathbf{n} = \int_{\Sigma_2} \mathbf{F} \cdot d\mathbf{n} + \int_{\Sigma_3} \mathbf{F} \cdot d\mathbf{n} - \Pi,$$

where Σ_1 is the boundary of the donor, Σ_2 is the boundary of the accretor, and Σ_3 is the outer boundary. By analogy with the mass flux from the system

$$\dot{M} = -\int_{\Sigma_3} \rho\mathbf{u} \cdot d\mathbf{n},$$

we can estimate the angular-momentum flux from the system

$$\dot{J} = -\int_{\Sigma_3} \mathbf{F} \cdot d\mathbf{n} \qquad (20)$$

and use this in our expression for the parameter specifying the degree to which the evolution is nonconservative with respect to angular momentum (8).

Note that, in our simulations, we solved the Euler equations for a nonviscous gas rather then the Navier–Stokes equations. Accordingly, to calculate the integral (20) in the expression for the momentum flux density $\mathbf{F}$ in the stress tensor $\mathcal{P}$, only the isotropic term corresponding to the gas dynamical pressure was taken into account: $\mathcal{P}_{\alpha\beta} = P\delta_{\alpha\beta}$. This substitution is completely justified, since viscosity does not play an appreciable role at the outer boundary of the domain where the integral (20) is calculated.

Applying expression (20) to the simulation of a system with $q = {}^1/_5$ [20], we obtain the value $\psi \sim 6$, which corresponds to $\alpha = 0.83$ (see the determination of α given above in Note 4), while we obtain $\psi \sim 5$ for a binary system with $q = 1$ [21], which corresponds to $\alpha = 1.25$. This latter value is consistent with the results of Sawada *et al.* [39], who obtained $\alpha = 1.65$ for a binary system with equal component masses.

However, applying these estimates to ψ in our evolution calculations indicated that the angular-momentum loss rates in binary systems are so high that, in most binaries, the mass transfer quickly becomes unstable and the donor mass-loss rate begins to increase without bound. Apparently, it is not entirely correct to use formula (20) to estimate the angular-momentum loss in cataclysmic-binary evolution calculations, since the gas dynamical and evolutionary models do not fit together well. The gas dynamical model does not take into account variations of the stellar positions in time (the distance between the components is assumed to be constant), so that variations in the angular momentum of the gas due to the noncentral character of the field Π are not compensated by corresponding variations in the angular momenta of the stars.

A more general gas dynamical model taking into account variations of the positions of the stars would enable correct estimation of the variations of the system angular momentum in the form of a momentum flux-density integral for the flux through the outer boundary of the closed "donor + accretor + gas" system. Due to difficulties in the gas dynamical calculations, however,

such estimations are possible only for a specific stage in the life of a binary. Moreover, the gas dynamical results cannot be directly used in standard evolutionary models, which do not take into account the presence of intercomponent matter in the system. Therefore, in the nearest future, an approach in which a simplified model for angular-momentum transfer in the system is developed on the basis of gas dynamical calculations is likely to be promising; the results of this simplified and parametrized model can then be used in evolution calculations.

5. A SIMPLIFIED MODEL FOR ESTIMATING THE ANGULAR-MOMENTUM LOSS RATE IN SEMI-DETACHED SYSTEMS

Gas dynamical modeling of mass transfer in semidetached systems suggests that the outflow from the donor's surface passes through a quite small area near L_1, so that the specific angular momentum of the outflowing matter can be estimated as $\lambda_{L_1} = \Omega\Delta^2$, where $\Delta = |x_c - x_{L_1}|$ is the distance from L_1 to the center of the mass of the system. Accordingly, the angular-momentum flux from the donor surface is

$$F_\lambda^2 = \lambda_{L_1}\dot{M}_2 = \Omega\Delta^2\dot{M}_2.$$

Since the mass transfer is nonconservative, only some fraction β of the matter flowing through L_1 is accreted, and the specific angular momentum of the accreted matter is equal to the specific angular momentum of the accretor (neglecting the finite radius of the accretor and/or the residual momentum of the matter, which is a reasonable approximation for cataclysmic binaries). In this case, the accreted matter possesses zero angular momentum relative to the accretor in the rotating coordinate frame. Consequently, it does not spin up the accretor; i.e., the problem of the efficiency of the transfer of momentum from the axial rotation of the accretor to the orbital motion of the system need not be considered. As a result, the flux of angular momentum onto the accretor is

$$F_\lambda^1 = \lambda_{accr}\beta\dot{M}_2 = \Omega\left(\frac{M_2}{M}\right)^2 A^2\beta\dot{M}_2.$$

The expressions for the flux of angular momentum from the donor to the accretor correspond to the general formula for the angular-momentum flux density **F** (19). As at the outer boundary, viscosity does not play an important role near the surfaces of the donor or accretor, where the matter has already lost its angular momentum completely, and the flow is radial in the rotating coordinate frame. Consequently, in this case, the stress tensor reduces to an isotropic pressure, which does not contribute to the integral of the angular-momentum flux density.

These considerations enable us to write the momentum flux lost by the system in the form

$$F_\lambda^{loss} = \eta(F_\lambda^2 - F_\lambda^1) = \eta\left(\Omega\Delta^2\dot{M}_2 - \Omega\left(\frac{M_2}{M}\right)^2 A^2\beta\dot{M}_2\right),$$

where η is a parameter determining the fraction of intercomponent-envelope momentum carried away by the matter leaving the system. Then, $1 - \eta$ is the fraction of the angular momentum of the intercomponent envelope that returns to the system via tidal interactions. From this point on, we will assume that $\eta = 1$; i.e., all the momentum of the intercomponent envelope is carried away with matter leaving the system.

In this case, the specific angular momentum of the matter leaving the system is

$$\lambda_{loss} = F_\lambda^{loss}/\dot{M}_{loss} = \frac{\Omega\Delta^2\dot{M}_2 - \beta\left(\frac{M_2}{M}\right)^2\Omega A^2\dot{M}_2}{(1-\beta)\dot{M}_2}$$

or, in units of the specific angular momentum of the system ($\lambda_{syst} = \Omega A^2 M_1 M_2/M^2$),

$$\psi = \lambda_{loss}/\lambda_{syst} = \frac{\left(f(q) - \frac{1}{1+q}\right)^2 - \beta\left(\frac{q}{1+q}\right)^2}{1-\beta}\frac{(1+q)^2}{q}, \quad (21)$$

where $f(q) = x_{L_1}/A$ is the dimensionless distance from the donor center of mass to L_1.

Note that (21) was derived assuming coaxial synchronous rotation of the binary components. The angular-momentum loss due to matter outflow through the vicinity of L_1 can make the intrinsic rotation of the donor star and the orbital rotation of the system become noncoaxial [40]. Although the flow structure in systems with noncoaxial, asynchronous rotation was treated previously in [41], we will not consider this effect here, due to the simplified form of the evolutionary models under study.

Figure 2 presents a plot of the relation $\psi(q)$ for various degrees of nonconservation β. This figure also presents the values $\psi = 0$ and $\psi = 1$, marked with dashed lines. In the domain $\psi > 1$, the angular momentum carried out per gram of matter leaving the system exceeds the average specific momentum of the system, resulting in a decrease of the binary's specific momentum:

$$\frac{\partial}{\partial t}\left(\frac{J}{M}\right) < 0.$$

In the domain $0 < \psi < 1$, the angular momentum carried out per gram of matter leaving the system is smaller than the average specific momentum of the system, so that

$$\frac{\partial}{\partial t}\left(\frac{J}{M}\right) > 0.$$

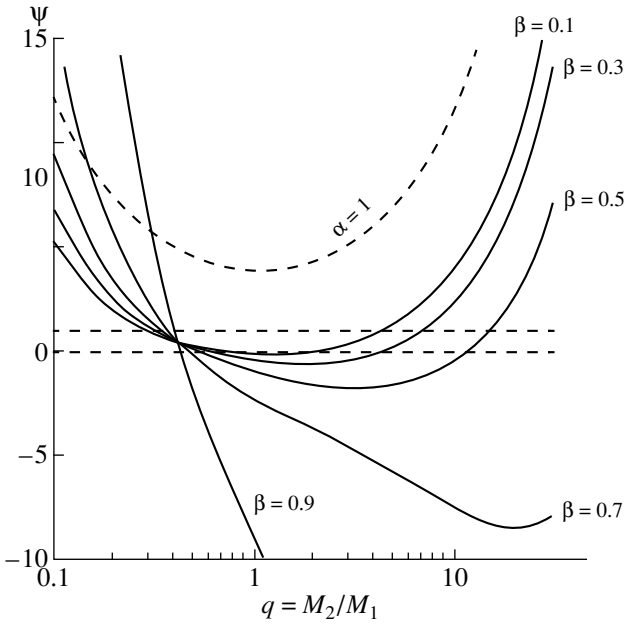

Fig. 2. Dependence of the degree of nonconservation with respect to angular momentum ψ on the mass ratio q for various degrees of nonconservation with reference to mass β [see (21)]. The dashed lines correspond to ψ = 0 and ψ = 1. The thick dashed curve shows the dependence $\psi = (1+q)^2/q$, corresponding to α = 1.

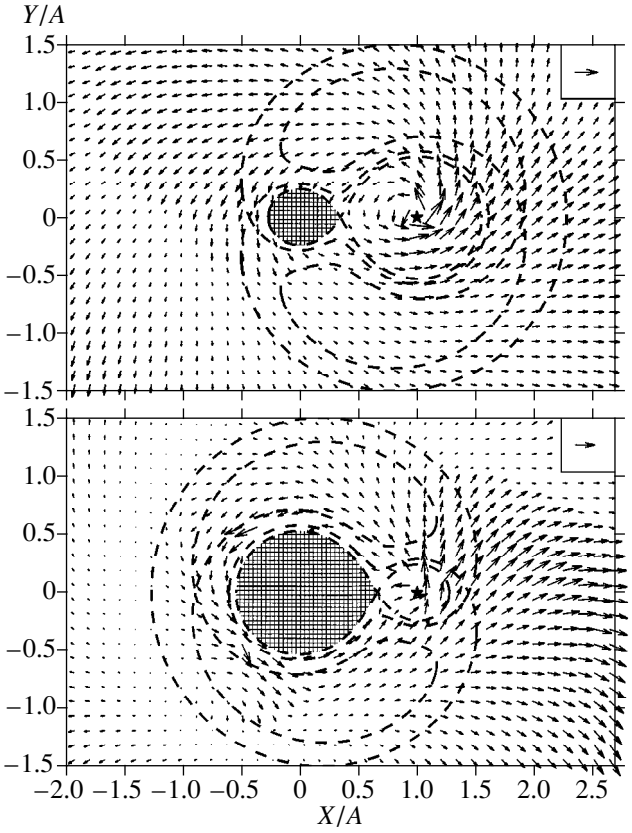

Fig. 3. Velocity vectors in the equatorial plane for three-dimensional gas dynamical calculations for a binary with $M_2/M_1 = 1:5$ ($q = 1/5$, top) and with $M_2/M_1 = 5:1$ ($q = 5$, bottom). The position of the accretor is marked by an asterisk. The shaded area shows the donor, and the dashed curves its Roche equipotentials. The vector in the upper right corner corresponds to a velocity $3A\Omega$.

As we can see from Fig. 2, for most cases of nonconservative mass transfer (with the exception of $\beta \sim 0$), ψ becomes negative for some range of q. In this case, the redistribution of angular momentum in the closed "donor + accretor + gas" system, due to the outflow of matter to infinity, increases the total momentum of the binary: $\dot{J} > 0$. It is obvious that such "pumping" of angular momentum into the system can stabilize the mass transfer in cataclysmic binaries. For example, a qualitative examination of variations in the orbital semimajor axis resulting from mass transfer indicates that, in conservative models, the mass transfer tends to increase the semimajor axis only when $q < 1$. In "nonconservative" models, the interval of q in which both mass transfer and mass loss from the system tend to increase the semimajor axis is considerably broader: When β = 0.5, this occurs for $0 < q < 2.8$.

The dependence $\psi(q, \beta)$ [see Fig. 2 and (21)] displays the following interesting peculiarity: The $\psi(q)$ curves for different values of β go through a common point. The position of this point corresponds to the case when the center of mass of the system is exactly between L_1 and the accretor, since, in this case, ψ does not depend on β. Fortunately, this does not affect the solution.

Three-dimensional simulations of the gas dynamics of matter flows in cataclysmic binaries confirm that, depending on the component mass ratio q, the matter outflow from the system can either decrease or increase the total angular momentum of the system. The typical flow patterns for systems with $M_2/M_1 = 1:5$ and $M_2/M_1 = 5:1$ (Fig. 3) indicate that, in the laboratory coordinate frame, the gas flowing out of the system rotates in different directions relative to the orbital motion (in both Figs. 3a and 3b, the orbital motion is counterclockwise). Accordingly, in the solutions, the variation of the total angular momentum of the binary system displays opposite signs: For $q = 1/5$, the momentum of the system decreases, while for $q = 5$, it increases.

A reasonable physical explanation for the different types of gas dynamical solutions obtained is provided by the following qualitative picture.

(1) The flux of matter leaving the system through the vicinity of the outer Lagrangian point L_2 is made up of intercomponent gas whose angular momentum is sufficient for it to overcome the gravitation of the accretor. The initial velocity of this matter (in the rotating coordinate frame) coincides with the direction of the orbital motion.

(2) The velocity of gas leaving the system varies depending on the gravitation of both components of the

system, the centrifugal force, the Coriolis force, and the pressure force. Variations in the azimuthal velocity of the gas are determined primarily by the Coriolis and gravitational forces, since the centrifugal force is centrally symmetric and the deviation of the pressure from central symmetry is also small. The action of the Coriolis force deflects the flux in the direction opposite to the orbital motion. In turn, the initial flux of matter leaving the vicinity of L_2 can be divided into two parts: The first maintains the direction of its initial motion, while the second, being deflected by the Coriolis force, assumes the opposite direction. The predominance of one or the other flux determines the final direction for the gas motion in the stationary solution.

(3) In a centrally symmetric gravitational field, the effect of the Coriolis force obviously cannot result in a solution where the direction of gas rotation does not coincide with the orbital rotation in the laboratory coordinate frame. The situation is fundamentally different when the field of the binary is not central. In this case, the gravitation of the donor star can additionally accelerate the matter of the flow, resulting in a solution with the opposite direction of gas rotation in the laboratory coordinate frame.

(4) It follows from (21) and Fig. 3 that there exists an interval of q for which the gas in the system moves opposite to the orbital rotation. This corresponds to the case when the gravitation of the donor star becomes sufficient to accelerate the gas to the extent required (the left boundary of the interval) but is not so high that it leads to inverse accretion back onto the donor (the right boundary of the interval). For all other values of q, the flux in the direction of the orbital rotation prevails.

The presence of an additional interval of q where nonconservative mass transfer is accompanied by an increase in the momentum of the binary expands the domain of stable mass transfer. This can be displayed with a $q-\zeta$ plot, frequently used to qualitative illustrate the problem of mass-transfer stability in cataclysmic binaries. Curves corresponding to analytical formulas for the derivative of the Roche-lobe radius with respect to the donor mass ζ_{RL} can be drawn, together with lines corresponding to the derivative of the star's radius with respect to the mass ζ_*, which is known from studies of their internal composition (see, for example, [35]). The mass transfer will be stable for the interval of q where the ζ_{RL} curve passes below the line ζ_* for the donor star of the corresponding type. Such a plot is presented in Fig. 4, which contains the derivative of the Roche-lobe radius $\zeta_{RL} = \dfrac{\partial \ln R_{RL}}{\partial \ln M_2}$ as a function of the mass ratio q for the case when the momentum loss is described by (21) for various values of the mass nonconservation parameter β. Figure 4 also shows the dependences $\zeta_{RL}(q)$ for mass transfer that is completely conservative with respect to mass and momentum and for cases when matter leaves the system and carries away specific angular momentum from the donor or accretor. The derivative $\zeta_* = \dfrac{\partial \ln R_2}{\partial \ln M_2}$ for totally convective and degenerate stars ($\zeta_* = -1/3$), roughly solar-mass main-sequence stars in thermal equilibrium ($\zeta_* = 0.6$), and subgiants with degenerate low-mass helium nuclei ($\zeta_* = 0$) are also plotted. We can see that, in accordance with (21), mass loss from the system is able to stabilize the mass transfer from the donor over a substantially broader interval of q than in the case of conservative transfer. Note that, in the case of conservative mass transfer for a star with mass of the order of $M_\odot$, the transfer time scale is determined by the momentum-loss or nuclear time scale for $q \lesssim 1.2$ [35], but, in the case considered, the corresponding boundary for q is also appreciably higher.

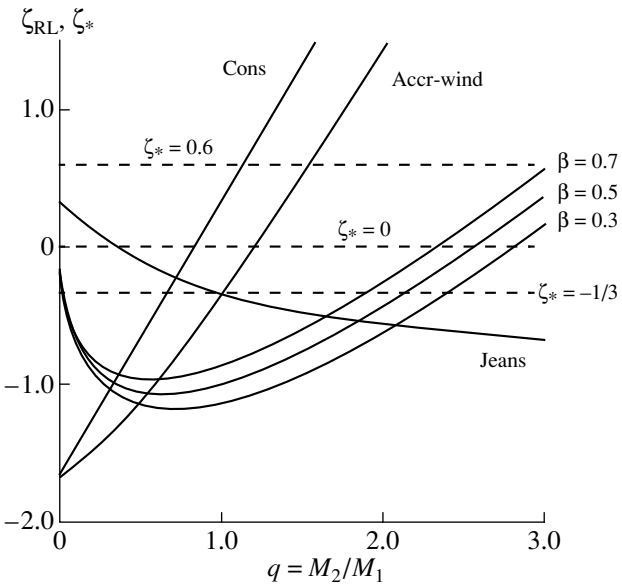

Fig. 4. Dependence of the logarithmic derivative of the Roche-lobe radius with respect to donor mass $\zeta_{RL} = \dfrac{\partial \ln R_{RL}}{\partial \ln M_2}$ on the mass ratio q (thick curves) for various degrees of mass nonconservation β [(3) and (21)]; dependence of the logarithmic derivative of the donor radius with respect to $\zeta_* = \dfrac{\partial \ln R_2}{\partial \ln M_2}$ on q (thin curves) for the case of mass-conservative transfer ["cons," equation (16)], a Jeans mass-loss regime ["Jeans," equation (17)], and a stellar wind ["accr-wind," equation (18)]. The dashed curves indicate ζ_* values for totally convective and degenerate stars ($\zeta_* = -1/3$), roughly solar-mass main-sequence stars in thermal equilibrium ($\zeta_* = 0.6$), and subgiants with degenerate low-mass helium cores ($\zeta_* = 0$).

We note again that, in the case under study, there is a region of unstable mass transfer for small q. The instability—i.e., the failure to satisfy condition (1)—results

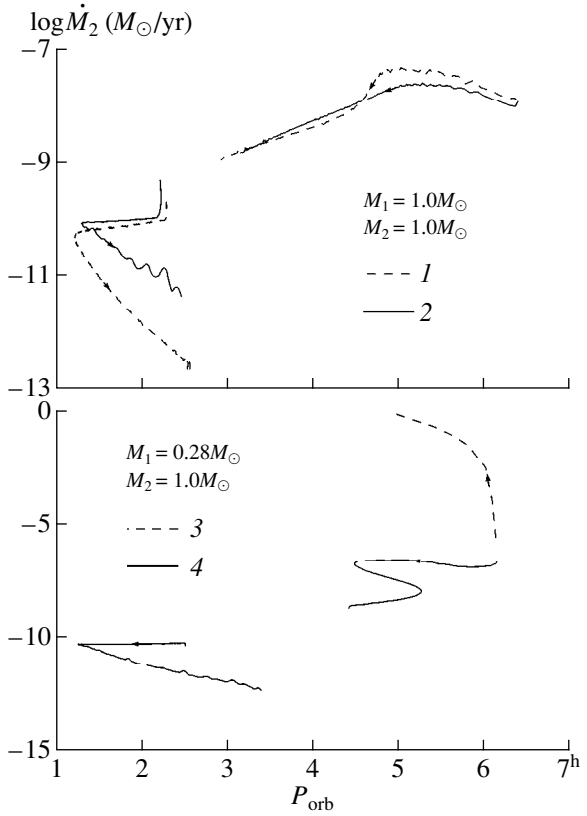

Fig. 5. Evolutionary tracks in the "orbital period–logarithm of the donor mass-loss rate" plane for systems with initial component masses $M_1 = 1.0\ M_\odot$, $M_2 = 1.0\ M_\odot$ (top) and $M_1 = 0.28\ M_\odot$, $M_2 = 1.0\ M_\odot$ (bottom). Tracks *1* and *3* (dashed) are "conservative," and tracks *2* and *4* (solid) are "nonconservative."

from the rapid increase of the ratio of the lost to the average specific momentum of the system [see (14) and (21)]. This can lead to the destruction of a donor with very low mass.[5] Thus, it is possible that some cataclysmic binaries that start their evolution as stable stars end with the catastrophic destruction of the donor when q decreases below some lower limit.

6. EVOLUTION OF CATACLYSMIC BINARIES LOSING MASS AND MOMENTUM

In order to take into account the results of three-dimensional gas dynamical calculations of mass transfer in cataclysmic binaries and corresponding estimates of the loss of momentum from the system via matter outflow, we have studied the evolution of cataclysmic binaries with various assumptions about the extent to which it is conservative.

[5] Another case of mass-transfer instability for small q is known, brought about by low efficiency of the tidal interaction between the accretion disk and orbital motion (see, for example, [42, 43]).

We calculated the evolution of the donor using a modified version of a code designed for studies of low-mass stars, used previously in [7, 10, 44–48]. The code uses the opacity tables compiled by Hebner *et al.* [49], supplemented at low temperatures with the tables of Alexander *et al.* [50], and the equation of state derived by Fontaine *et al.* [51], with the corrections of Denisenkov [52]. We adopted nuclear reaction rates in accordance with [53, 54].

All calculations assumed that the donor fills its Roche lobe immediately after the star reaches the zero-age main sequence. The donor mass was taken to be between 0.1 and $1.2M_\odot$, with various mass ratios q. We assumed the donor had a chemical composition $X = 0.70$, $Y = 0.28$, $Z = 0.02$. In calculations for the convective temperature gradient, we took the mixing length parameter l/H_p to be 1.8. We used the method suggested by Kolb and Ritter [55] to calculate the mass-loss rate of the donor for a given donor radius and average Roche-lobe radius. Based on the earlier results of gas dynamical calculations, when considering nonconservative evolution, we assumed that the fraction of matter accreted by the dwarf β was 0.5 and that the momentum carried away by matter leaving the system was determined by (21). We did not take into consideration possible mass and momentum loss due to the ejection of matter in flares.

Let us consider the evolution of cataclysmic binaries with stable mass transfer in a mass-conservative model. Figure 5 (a plot of orbital period vs. the logarithm of the donor mass-loss rate) presents two tracks, one calculated in the "conservative" approximation (track *1*) and the other in the "nonconservative" approximation (track *2*). The initial masses of both the donor and accretor are $1.0\ M_\odot$. We can see that there are no fundamental differences between tracks *1* and *2*. In the initial stage of evolution of the cataclysmic binary, the predominant factor is the loss of momentum from the system via a MSW from the donor. As a result of this momentum loss, the orbital semimajor axis and period decrease in the course of the system's evolution. With the decrease of the donor mass and radius, $\left(\frac{\partial A}{\partial t}\right)_{MSW}$ the MSW also decreases [see (13)], which, after some time, results in a gradual decrease of the donor mass-loss rate $\dot{M}_2$. $\dot{M}_2$ is appreciably smaller for the nonconservative track than for the conservative track, since ψ is negative at this stage of the evolution (Fig. 2), and the total loss of orbital angular momentum in the nonconservative system is smaller than in the conservative system. At later stages of evolution, after q decreases enough that the loss of momentum for the nonconservative evolution increases sharply, the situation is reversed.

After the star becomes totally convective, the MSW from the donor terminates. The stellar mass for which total mixing occurs depends on the extent of deviation from

thermal equilibrium. Equilibrium models for main-sequence stars become totally convective at masses $\sim 0.36 M_\odot$; stars in binary systems losing mass become totally convective at smaller masses, close to 0.25–$0.30 M_\odot$ (for our assumptions about the chemical composition and opacity of the stellar matter).

For the conservative track, mixing occurs when $M_2 = 0.265 M_\odot$ (at this time, $P_{\rm orb} = 3^{\rm h}.27$), while, for the nonconservative track, mixing occurs when $M_2 = 0.249 M_\odot$ ($P_{\rm orb} = 3^{\rm h}.54$).[6] Thus, the donor mass and orbital period corresponding to the upper boundary of the gap in the cataclysmic-binary periods differ little for the conservative and nonconservative tracks.

After the donor MSW ceases, the momentum loss rate in the system decreases dramatically, and the approach of the two components decelerates. As a result, the donor is no longer able to fill its Roche lobe, and its mass loss terminates. Since the radius of the donor exceeds the radius of a main sequence star in thermal equilibrium when the MSW ceases, the donor radius decreases to its equilibrium value [27]. Consequently, the ratio of the radii of the donor and its Roche lobe decreases even further. The only factor determining the evolution of the system during this detached stage of evolution is GWR, which causes the stars to slowly approach until the donor again fills its Roche lobe and the mass transfer resumes. During the detached stage, the system is not manifest as a cataclysmic binary, so that it "disappears" during some interval of periods. This provides an explanation for the observed gap in the periods of cataclysmic binaries.

The observed period gap is between $2^{\rm h}.1$ and $3^{\rm h}.1$ [37]. The edges of the theoretical period gap depend on the rate of momentum loss via the MSW and the initial physical parameters of the evolution code, which determine the theoretical radii of the stars. The code we used overestimates the lower boundary to some extent. The edges of the gap for the conservative track were $2^{\rm h}.5$–$3^{\rm h}.3$, while those for the nonconservative track were $2^{\rm h}.4$–$3^{\rm h}.5$. The discrepancy is due to the different rates of momentum loss before the gap and also to the different masses of the accretors after termination of the first semidetached stage of evolution.

Note that a pronounced deficiency of cataclysmic binaries is observed in the period gap, rather than their total absence [37]. The presence of cataclysmic binaries in the gap can be understood as follows:

(a) For cataclysmic binaries with donor masses 0.25–0.4 $M_\odot$, mass transfer starts immediately within the gap.

(b) If the donor fills its Roche lobe at a later stage of core hydrogen burning rather than at the zero age main sequence, total mixing does not occur when its mass decreases to $\sim 0.3\ M_\odot$, due to the presence of a helium core (see, for example, [46, 47]; note, however, that such systems are very rare).

The stage of evolution after the period gap is characterized by substantially lower rates of mass loss by the donor, since the main factor determining the evolution is the radiation of gravitation waves by the system. In this case, the loss of momentum from the system is substantially smaller than at earlier stages, when momentum is lost via MSW from the donor. The other characteristic feature of this stage of evolution is the presence of a minimum period. This is related to the increase in the degeneracy of the matter in the donor and the corresponding variation of the radius–mass dependence of the star [56, 57]: When the donor mass decreases to $\sim 0.05\ M_\odot$, its radius begins to increase as its mass decreases, and the exponent of the mass–radius relation tends to –1/3. The minimum period corresponds to the exponent +1/3. The minimum periods for the conservative and nonconservative tracks are $75^{\rm m}$ and $81^{\rm m}$, respectively. This discrepancy in $P_{\rm min}$ is due to differences in the total masses of the systems and in the extent to which the donor radii deviate from the values corresponding to thermal equilibrium, due to differences in their mass-loss rates. After passing the minimum period, the orbital period begins to increase. At this stage, the rate of mass loss by the donor decreases rapidly as the period increases. We can see from Fig. 5 that the difference between the conservative and nonconservative tracks increases at this stage. This is due to the fact that the orbital angular-momentum loss rate rapidly increases as q decreases in the nonconservative case.

The mass-transfer rates for the conservative and nonconservative tracks become considerably different after the passage of the minimum orbital period. The probability of observing a semidetached binary in a given interval of orbital periods is

$$p(\log P) \propto \frac{(-\dot{M}_2)^\gamma}{\dot{P}/P}, \qquad (22)$$

where γ is a positive constant. For apparent-magnitude limited samples, $\gamma \simeq 1$ [58].

After the minimum period is passed, in the period interval $2^{\rm h}$–$2^{\rm h}.5$, the average probability for observing a cataclysmic binary on the nonconservative track is approximately a factor of 1.2 larger than the probability for a binary on the conservative track. Thus, in spite of the appreciable difference in mass-transfer rates, the probabilities of observing cataclysmic binaries in the two cases only slightly differ, since a nonconservative

[6] Since we are interested in the details of cataclysmic-binary evolution related to possible nonconservation of mass and momentum, we formally continued our calculations after the accretor reached the Chandrasekhar mass, despite the fact that the evolution of real systems is interrupted at this time by thermonuclear explosion of the white dwarf. In principle, our extension of the calculations for $M_1 > M_{Ch} \approx 1.4\ M_\odot$ is justified by the fact that, in reality, the accretion may spin up the accretor and that the critical mass for rapidly rotating dwarfs can substantially exceed M_{Ch}.

system passes through the corresponding interval of periods more rapidly.

Since the characteristic variability of cataclysmic binaries depends on their mass-transfer rates, the differences in $\dot{M}_2$ predicted for conservative and nonconservative evolution could be reflected in the distribution of cataclysmic binaries according to variability type.

Figure 5 presents tracks for cataclysmic binaries that should undergo dynamically unstable mass transfer in a standard mass-conservative evolutionary model. The initial masses for the donor and accretor are equal to 1.0 $M_\odot$ and 0.28 $M_\odot$, respectively. We have chosen such an extreme mass ratio purely for the purpose of demonstration.

Track *3* was calculated under the standard assumption of momentum loss only due to GWR and MSW. It represents a typical case of unstable mass transfer with unlimited increase of the mass-loss rate of the donor and rapid approach of the mass-loss time scale to the dynamical time scale. Strictly speaking, this can only be considered a qualitative illustration of this type of evolution, since the calculation did not take into account the formation of a common envelope in the system, which should increase the orbital angular-momentum loss rate even more.

Track *4*, calculated assuming a loss of mass and momentum from the system in accordance with (21), is similar to tracks for the stable evolution of cataclysmic binaries, with all their typical features. It differs from track *2* in the higher mass-loss rate of the donor in the initial stage of evolution, due to the substantial increase in the $\left(\frac{\partial A}{\partial t}\right)_{\rm MSW}$ for large q [see (13)]. This results in a larger deviation of the donor from equilibrium and, accordingly, in variations in the upper edge of the period gap: This edge is at $4^{\rm h}.4$ for track *4*, whereas it is $3^{\rm h}.5$ for track *2*. The minimum period for track *4* is $76^{\rm m}$, which is nearly the same as that for track *1*, but somewhat smaller than that for track *2*.

7. BOUNDARIES OF THE DOMAIN OF STABLE MASS TRANSFER

We determined the boundary of the domain of stable mass transfer in the non-mass-conservative model as follows. We calculated a series of tracks for a given donor mass with different q values in steps of 0.1. We took the boundary to be the maximum q value for which the accretion rate onto the white dwarf remained below the Eddington limit in the course of evolution, i.e., such that, when q was increased by 0.1, the accretion rate exceeded the Eddington limit. Note that, upon further increase of q, an unlimited increase in the mass-loss rate of the donor arises in the calculated tracks when q becomes 0.2–0.3 larger than the limiting value. Note that the results of this method for determining the domain of stable mass transfer are in good agreement with those based on comparing the derivatives of the donor and Roche-lobe radii.

The new boundary for the stable mass-transfer domain (assuming nonconservative evolution) is presented in Fig. 1. We can see that this domain includes all observed cataclysmic binaries with estimated component masses. Thus, in the transition to a nonconservative model for the evolution of cataclysmic binaries, the problem of observed binaries being outside the domain of stable mass transfer disappears.

In the $q - M_2$ diagram, all observed cataclysmic binaries are concentrated toward $q \lesssim 1$, whereas the nonconservative model predicts considerably higher q values. To study the origin for this discrepancy, we calculated a number of tracks for nonconservative systems with initial donor masses from $M_2^{init} = 0.1\ M_\odot$ to $M_2^{init} = 1.2\ M_\odot$ in steps of 0.1 $M_\odot$ and q values such that these tracks originate in the immediate vicinity of the new boundary for the domain of stable mass transfer. These tracks are presented in the $q - M_2$ diagram in Fig. 6. We used these tracks to derive the isochrones presented in Fig. 6, corresponding to times of 10^5, 10^6, 10^7, 10^8, 10^9, and 10^{10} yrs, calculated from the onset of the mass transfer between the components.[7] We chose this "extreme" group of tracks since these systems spend the most time between the new and old boundaries for the stable mass-transfer domain. It is obvious that systems with smaller initial q, whose tracks originate to the left of the new boundary, will spend a shorter time there. Therefore, cataclysmic binaries with initial parameters close to these "extreme" values have the highest probability to fall in this area.

According to the locations of the isochrones in Fig. 6, the tracks can be divided into two distinct groups:

(1) Tracks for systems with massive donors (0.4–1.2 $M_\odot$), for which the specifics of evolution before the period gap are primarily determined by the loss of momentum from the system via the donor's MSW.

(2) Tracks with low-mass donors (0.1–0.3 $M_\odot$), for which this stage is absent, since their donors are completely convective from the very beginning.

The tracks for the first group are characterized by a high (~10^{-6}–10^{-9} $M_\odot$/yr) donor mass-loss rate before the period gap and, consequently, a rapid decrease of the donor mass and the component mass ratio. This results in the rapid evolution of the system in the $q - M_2$ diagram, so that the system passes through the section near the new boundary of the stable mass-transfer domain over a time not exceeding 10^7 yrs. This explains the absence of observed cataclysmic binaries in the vicinity of this boundary. The evolution of tracks in the second

[7] Note that the isochrone corresponding to 10^9 yrs merges with the 10^8-yr isochrone for tracks with initial donor masses of $M_2^{init} \geq 0.4 M_\odot$, since both times fall in the period gap.

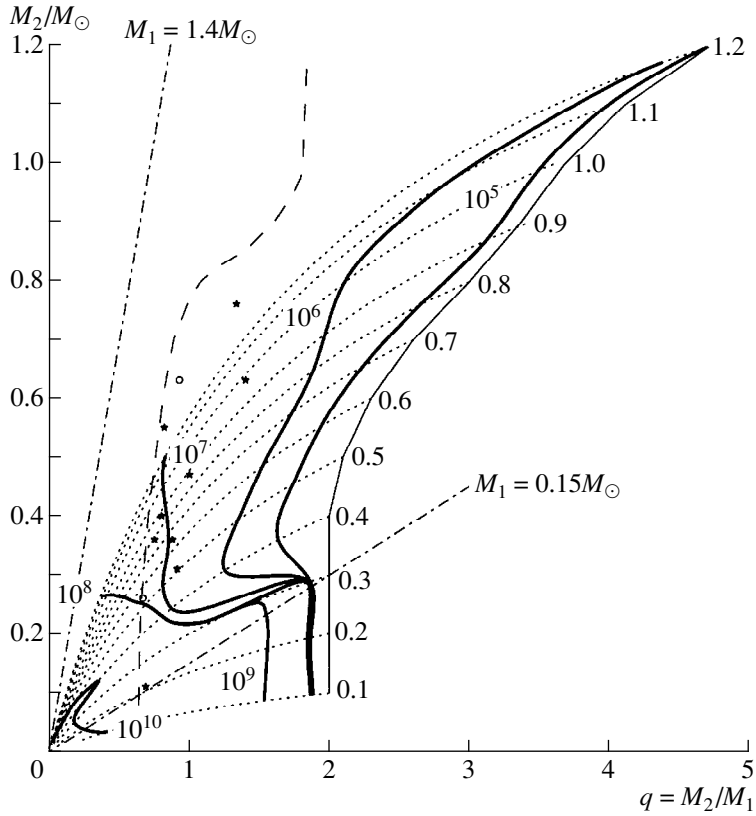

Fig. 6. Cataclysmic binary evolutionary tracks in the "qM_2" plane for a nonconservative model (dotted; the number next to the origin of the track denotes the initial donor mass in $M_\odot$). The thick curves are isochrones; the numbers near them denote time in years. The dashed line indicates the boundary for the domain of stable mass transfer according to [35]. The solid line indicates the corresponding boundary derived in the present study. Other notation is the same as in Fig. 1.

group, excluding a short initial stage with a high mass-transfer rate, is characterized by a low ($\sim 10^{-10}$ $M_\odot$/yr) donor mass-loss rate, which remains nearly constant over an extended period of time (until the minimum period is reached). Accordingly, in the course of evolution, the donor mass and the component mass ratio vary very slowly. Consequently, systems starting their evolution near the new stable mass-transfer boundary should, in principle, remain near it for a fairly long time. The absence of cataclysmic binaries in this area is due to the fact that the masses of dwarfs in zero-age cataclysmic systems cannot exceed ~0.15 $M_\odot$—the minimum mass for the helium core of a star leaving the main sequence. All the observed cataclysmic binaries in Fig. 6 are located in the area delineated by the lines corresponding to the maximum and minimum masses of a white dwarf—1.4 and 0.15 $M_\odot$.

8. CONCLUSION

Results of three-dimensional gas dynamical calculations indicate that, in the course of a cataclysmic binary's evolution, a considerable fraction of the matter lost by the donor should leave the system. At the same time, a number of observed cataclysmic binaries have combinations of donor and accretor masses that are "forbidden" under the standard assumptions for variations of the angular momentum of the system, since the mass transfer should be unstable in these cases. This problem is resolved by the model proposed in our study, which takes into account the loss of mass and angular momentum from the system, in accordance with the results of the gas dynamical calculations. We have shown that the observations can be satisfactorily explained if we estimate the momentum loss using an approximation in which the specific angular momentum of the matter flowing out of the system is determined by the difference between the specific momentum of the matter of the donor at the Lagrangian point L_1 and the specific momentum of the accretor. In this case, the fraction of matter lost by the donor that leaves the system can be of the order of 50%. It is important that, in our evolution calculations, the transition to a nonconservative model does not result in appreciable variations of such evolutionary-track parameters as the boundaries of the period gap or the minimum period of the system.

ACKNOWLEDGMENTS

This work was supported by the Russian Foundation for Basic Research (project no. 99-02-17619 and 99-02-16037) and a Presidential grant of the Russian Federation (99-15-96022).

REFERENCES

1. S. Rappaport, P. C. Joss, and R. F. Webbink, Astrophys. J. **254**, 616 (1982).
2. S. Rappaport, F. Verbunt, and P. C. Joss, Astrophys. J. **275**, 713 (1983).
3. I. Iben, Jr., and A. V. Tutukov, Astrophys. J. **284**, 719 (1984).
4. J. Patterson, Astrophys. J., Suppl. Ser. **54**, 443 (1984).
5. R. F. Webbink, in *Interacting Binary Stars*, Ed. by W. H. G. Lewin, J. van Paradijs, and E. P. J. van den Heuvel (Cambridge University Press, Cambridge, 1985), p. 39.
6. U. Kolb, Astron. Astrophys. **271**, 149 (1993).
7. A. V. Fedorova and A. V. Tutukov, Astron. Zh. **71**, 431 (1994).
8. H. Ritter, in *Evolutionary Processes in Close Binary Stars*, Ed. by R. A. M. J. Wijers, M. B. Davies, and C. A. Tout (Kluwer, Dordrecht, 1992), p. 307.
9. M. Politano, Astrophys. J. **465**, 338 (1996).
10. A. V. Fedorova, in *Double Stars*, Ed. by A. G. Masevich (Kosmoinform, Moscow, 1997), p. 179.
11. R. P. Kraft, J. Mathews, and J. L. Greenstein, Astrophys. J. **136**, 312 (1962).
12. B. Paczyński, Acta Astron. **17**, 267 (1967).
13. E. Schatzman, Ann. Astrophys. **25**, 18 (1962).
14. L. Mestel, Mon. Not. R. Astron. Soc. **138**, 359 (1968).
15. P. P. Eggleton, in *Structure and Evolution of Close Binary Stars*, Ed. by P. P. Eggleton, S. Mitton, and J. Whelan (Reidel, Dordrecht, 1976), p. 209.
16. F. Verbunt and C. Zwaan, Astron. Astrophys. **100**, L7 (1981).
17. L. R. Yungel'son, Nauchn. Inform. Astron. Soveta **26**, 71 (1973).
18. K. H. Kieboom and F. Verbunt, Astron. Astrophys. **395**, L1 (1981).
19. A. King and U. Kolb, Astrophys. J. **439**, 330 (1995).
20. D. V. Bisikalo, A. A. Boyarchuk, V. M. Chechetkin, *et al.*, Mon. Not. R. Astron. Soc. **300**, 39 (1998).
21. D. V. Bisikalo, A. A. Boyarchuk, O. A. Kuznetsov, *et al.*, Astron. Zh. **75**, 706 (1998).
22. P. P. Eggleton, Astrophys. J. **268**, 368 (1983).
23. B. Paczyński, Ann. Rev. Astron. Astrophys. **9**, 183 (1971).
24. O. A. Kuznetsov, Astron. Zh. **72**, 508 (1995).
25. L. D. Landau and E. M. Lifshitz, *The Classical Theory of Fields* (Pergamon, Oxford, 1975; Fizmatgiz, Moscow, 1962).
26. A. Skumanich, Astrophys. J. **171**, 565 (1972).
27. H. C. Spruit and H. Ritter, Astron. Astrophys. **124**, 267 (1983).
28. I. Hachisu, M. Kato, and K. Nomoto, Astrophys. J. **470**, L97 (1996).
29. L. Yungelson and M. Livio, Astrophys. J. **497**, 168 (1998).
30. M. Kato and I. Hachisu, Astrophys. J. **437**, 802 (1994).
31. L. Yungelson, M. Livio, J. Truran, *et al.*, Astrophys. J. **466**, 890 (1996).
32. M. Livio, A. Govarie, and H. Ritter, Astron. Astrophys. **246**, 84 (1991).
33. K. Schenker, U. Kolb, and H. Ritter, Mon. Not. R. Astron. Soc. **297**, 633 (1998).
34. A. V. Tutukov and L. R. Yungel'son, Nauchn. Inform. Astron. Soveta **20**, 88 (1971).
35. A. V. Tutukov, A. V. Fedorova, and L. R. Yungel'son, Pis'ma Astron. Zh. **8**, 365 (1982).
36. M. de Kool, Astron. Astrophys. **261**, 188 (1992).
37. H. Ritter and U. Kolb, Astron. Astrophys., Suppl. Ser. **129**, 83 (1998).
38. D. A. Smith and V. S. Dhillon, Mon. Not. R. Astron. Soc. **301**, 767 (1998).
39. K. Sawada, I. Hachisu, and T. Matsuda, Mon. Not. R. Astron. Soc. **206**, 673 (1984).
40. J. J. Matese and D. P. Whitmire, Astrophys. J. **266**, 776 (1983).
41. D. V. Bisikalo, A. A. Boyarchuk, O. A. Kuznetsov, *et al.*, Astron. Zh. **76**, 270 (1999).
42. M. A. Ruderman and J. Shaham, Nature **304**, 425 (1983).
43. P. Hut and B. Paczyński, Astrophys. J. **284**, 675 (1984).
44. A. V. Fedorova and L. R. Yungelson, Astrophys. Space Sci. **103**, 125 (1984).
45. A. V. Tutukov, A. V. Fedorova, É. V. Érgma, *et al.*, Pis'ma Astron. Zh. **11**, 123 (1985).
46. A. V. Tutukov, A. V. Fedorova, É. V. Érgma, *et al.*, Pis'ma Astron. Zh. **13**, 780 (1987).
47. A. V. Fedorova and É. V. Érgma, Astrophys. Space Sci. **151**, 125 (1989).
48. A. V. Tutukov and A. V. Fedorova, Astron. Zh. **66**, 1172 (1989).
49. W. F. Huebner, A. L. Merts, N. H. Magee, *et al.*, *Astrophysical Opacity Library: Los Alamos Sci. Lab. Rep. LA-6760-M* (Los Alamos, 1977).
50. D. R. Alexander, H. R. Johnson, and R. L. Rypma, Astrophys. J. **272**, 773 (1983).
51. G. Fontaine, H. C. Graboske, and H. M. van Horn, Astrophys. J., Suppl. Ser. **35**, 293 (1977).
52. P. A. Denisenkov, Nauchn. Inform. Astron. Soveta **67**, 145 (1989).
53. M. J. Harris, W. A. Fowler, G. R. Caughlan, *et al.*, Ann. Rev. Astron. Astrophys. **21**, 165 (1983).
54. G. R. Caughlan, W. A. Fowler, M. J. Harris, *et al.*, At. Data Nucl. Data Tables **32**, 197 (1985).
55. U. Kolb and H. Ritter, Astron. Astrophys. **236**, 385 (1990).
56. J. Faulkner, Astrophys. J. (Lett.) **170**, L99 (1971).
57. B. Paczyński, Acta Astron. **31**, 1 (1981).
58. U. Kolb, A. R. King, and H. Ritter, Mon. Not. R. Astron. Soc. **298**, L29 (1998).

Translated by K. Maslennikov

Astronomy Reports, Vol. 44, No. 5, 2000, pp. 323–333. Translated from Astronomicheskiĭ Zhurnal, Vol. 77, No. 5, 2000, pp. 373–384.

Intercombinational Line Profiles in the UV Spectra of T Tauri Stars and Analysis of the Accretion Zone

S. A. Lamzin

Sternberg Astronomical Institute, Universitetskiĭ pr. 13, Moscow, 119899 Russia

Received May 5, 1999

Abstract—We have analyzed for the first time profiles of the SiIII 1892 Å and CIII 1909 Å intercombinational lines in HST spectra of the stars RY Tau and RU Lup. The widths of these optically thin lines exceeded 400 km/s, ruling out formation in the stellar chromosphere. Since the intensity of the Si line exceeds that of the C line, it is unlikely that a large fraction of the observed line flux is formed in a stellar wind. The observed profiles can be reproduced in the framework of an accretion shock model if the velocity field in the accretion zone is appreciably nonaxisymmetric. In this case, the line profiles should display periodic variations, which can be used to determine the accretion zone geometry and the topology of the magnetic field near the stellar surface; corresponding formulas are presented. In addition, periodic variations of the 0.3–0.7 keV X-ray flux should be observed. *© 2000 MAIK "Nauka/Interperiodica".*

1. INTRODUCTION

The activity of classical T Tauri stars is usually interpreted as the result of protoplanetary disk accretion onto a magnetized young star. It is thought that material from the inner regions of the disk is frozen in the star's magnetic-field lines and then slides along the field lines to the stellar surface. When the gas reaches a velocity of ~300 km/s, it decelerates sharply in a shock and is heated; the radiation of this gas is responsible for the observed line and short-wavelength continuum emission.

In this picture, the profiles and intensities of emission lines should vary as a result of nonstationary accretion and/or of displacements of the accretion zone relative to the observer due to the star's rotation. Both regular and quasiperiodic variations of emission-line parameters are observed in classical T Tauri stars (see, for example, [1–3]).

Information about the shape and extent of the accretion zone on the surface of a classical T Tauri star would offer a unique possibility to investigate the topology of the magnetic fields of young stars and interactions between the accretion disk and magnetosphere, making studies of the accretion-zone geometry very important. The application of Doppler tomography for this purpose using the rich observational data available for optical lines [4] is very promising but still premature. The main problem is that this technique is based on comparisons of observed profiles with those obtained using corresponding theoretical models. However, all the optical emission lines in classical T Tauri stars are optically thick, and it is not known how the intensities of these lines depend on the parameters of the accreted gas or the angular coordinates in shock models. The situation is complicated by the fact that almost every optical line could be formed not only in the shock, but also in the stellar wind.

This problem can be substantially simplified if optically thin lines, which are obviously formed in the shock, are used to study the accretion-zone geometry. The SiIII 1892 Å and CIII 1909 Å intercombinational lines (ICL) observed in the UV spectra of classical T Tauri stars [5] probably provide one example of such lines. We will show that even single observations of the profiles for these lines make it possible to draw some important conclusions.

2. OBSERVATIONAL DATA

Among the large number of UV spectra of T Tauri stars in the Hubble Space Telescope Archive Database (http://archive.stsci.edu/hst/target_descriptions.html), only two spectra clearly display SiIII 1892 Å and CIII 1909 Å intercombinational lines. These are the spectra of RU Lup (z10t0109m) and RY Tau (zle70108t) obtained with the GHRS spectrograph on August 24, 1992, and December 31, 1993, respectively. Each spectrum has a width of 40 Å, a resolution of ≃13 km/s, and consists of five consecutive exposures with a total duration of ≃1500 s. The spectra were processed using the IRAF package v2.11 (http://iraf.noao.edu/iraf) and STSDAS/TABLES code v2.0.2 (http://ra.stsci.edu/STSDAS.html), following the standard technique described in Section 36 of the "HST Data Handbook" (http://www.stsci.edu/documents/data_handbook.html). We adopted the calibration files recommended in the Archive Database for each star. Figure 1a presents the spectrum of RU Lup averaged over all exposures, and Fig. 1b shows the same spectrum smoothed with a five-point sliding average. Figure 2 presents the same information for RY Tau.

1063-7729/00/4405-0323$20.00

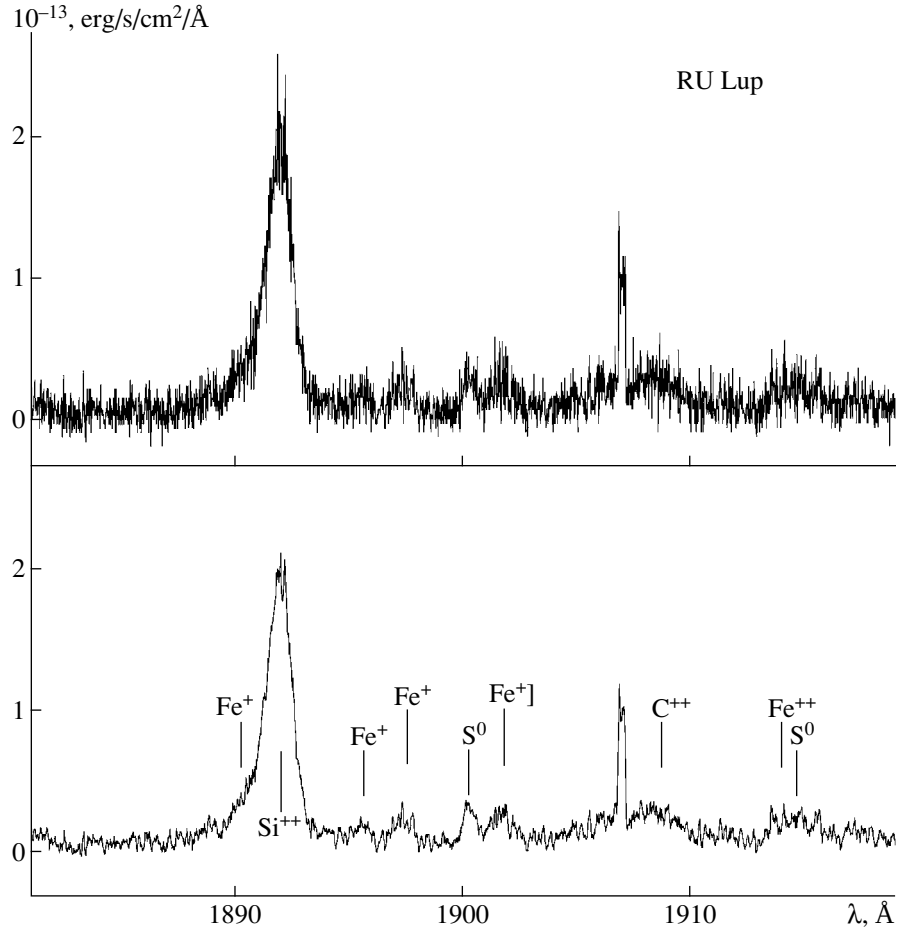

Fig. 1. Spectrum of RU Lup obtained with the Hubble Space Telescope. See the text for more details.

For RU Lup, only the SiIII 1892.03 Å line can be identified confidently. One characteristic feature of this line is the presence of extended wings, with the short-wavelength wing almost twice as broad as the long-wavelength wing: $\Delta V \simeq 400$ and 250 km/s, respectively. We suggest that the profile asymmetry is due to the presence of blending emission lines at wavelengths 1890–1891 Å.

Among spectral lines of the most abundant elements with a low excitation potential $E_i < 4$ eV, we believe that only the FeII 1890.24 Å line (Fig. 1b)—which belongs to the $b^2P_{3/2}$–$w^2D^0_{5/2}$ multiplet, with $E_i = 3.19$ eV (see the Atomic Line List v2.01 database (http://www.pa.uky.edu/peter/atomic))—is suitable for this role. The FeII 1897.55 Å ($^2P_{3/2}$–$^2D^0_{3/2}$) line, which can be identified with a corresponding emission feature in the spectrum of RU Lup (Fig. 1b), belongs to this same multiplet. Using the values of A_{ij} for FeII [6], we find that, if the upper levels of the multiplet are populated in proportion to their statistical weights and the lines are optically thin, the 1890.24 Å line should be nearly an order of magnitude more intense than the 1897.55 Å line; however, this is not observed. Note that emission around 1897.5 Å is also seen in the spectrum of RY Tau (Fig. 2); however, the 1890.24 Å line is not observed there. Nonetheless, we cannot exclude the possibility that the FeII line contributes to the short-wavelength wing of the SiIII] 1892 Å line in RU Lup. This could be tested by searching for the 1939.70 Å line ($^2P_{3/2}$–$^2D^0_{3/2}$ transition), which, under the same conditions, should be roughly a factor of five more intense than the 1897.55 Å line. Unfortunately, the 1892 Å line does not fall in the range of available spectrograms.

Is it possible to relate the SiIII] 1892 Å line to matter outflow from RU Lup? The profiles of the OI 6300 and 5577 Å and the SII 4069 and 6731 Å forbidden lines in the spectrum of this star, indeed, have broad short-wavelength wings extending to ≈300 km/s [7]. However, the wings of these lines from the red side the extension are a factor of five smaller than in the case of the SiIII] 1892 Å line. In addition, in the spectra of Herbig–Haro objects—i.e., in regions of stellar wind, where the lines of highly ionized ions are formed—the CIII] 1909 Å line is an order of magnitude more intense than the SiIII 1892 Å line (see [8] and references therein), in contrast to the situation observed in

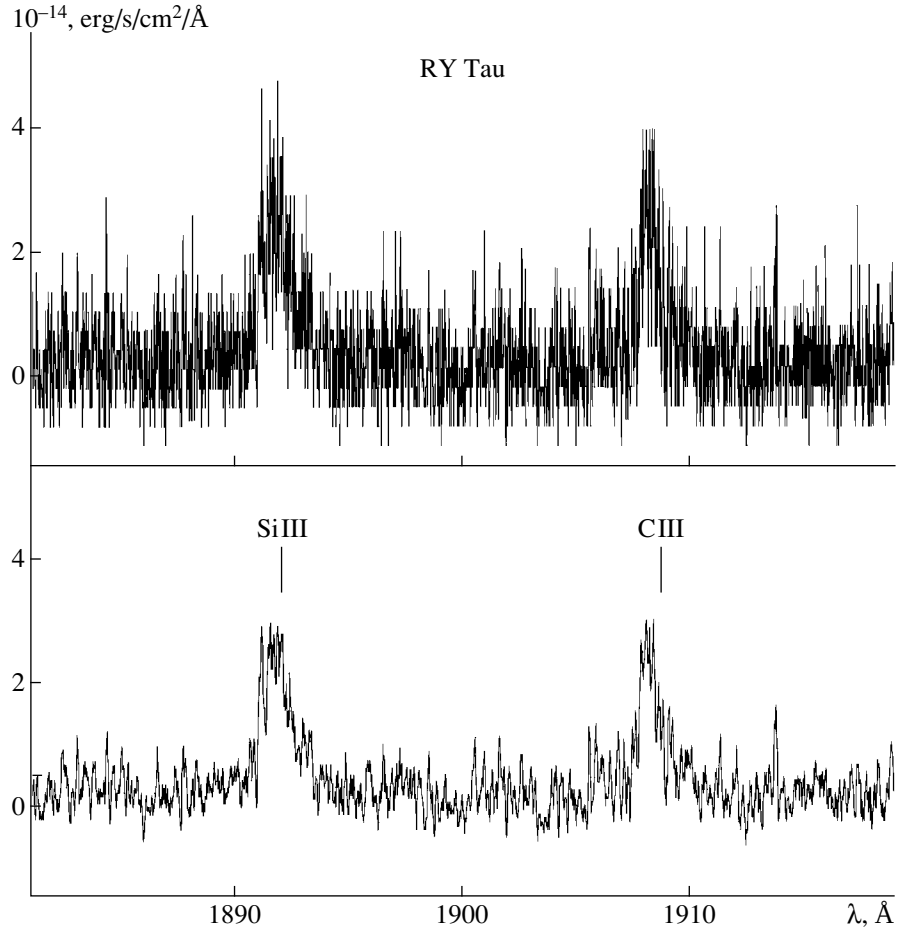

Fig. 2. Spectrum of RY Tau obtained with the Hubble Space Telescope. See the text for more details.

RU Lup. We, therefore, conclude that the bulk of the SiIII] 1892 Å line emission is not formed in the stellar wind. On the other hand, the large width of the line rules out the possibility that it is formed in a region similar to the solar chromosphere.

However, these arguments do not exclude the possibility that roughly 5% of the observed flux in the SiIII] 1892 Å line forms in material in the stellar wind, which primarily distorts the shape of the short-wavelength wing. In this connection, note the narrow peak displaced –280 km/s from the expected position of the CIII] 1909 Å line. It is tempting to interpret this peak as a line associated with the stellar wind: The star of RU Lup is probably viewed nearly pole-on [9], so that a line formed in a jet perpendicular to the disk should be displaced toward the blue. The only problem is that a feature with similar shape and intensity can be seen in the z10t0107m spectrogram, which was obtained at 1622–1657 Å 25 minutes before the spectrogram under consideration, and this feature falls on the same photodiodes of the receiving matrix (342–345). Since no other spectra of the star display any feature of this kind, it is reasonable to assume that both features resulted from a temporary defect in the detector. At the same time, these photodiodes were not marked defective in service files for these spectra. Therefore, the nature of the emission featire near 1907 Å remains unclear.

The CIII] 1908.73 Å line can be identified with confidence, but due to its low intensity, we can only say that the extent of its long-wavelength wing is roughly the same as that of the SiII] 1892 Å line, while its flux is about an order of magnitude lower. This last fact implies that the density of the accreted gas is much larger than derived in [10] on the basis of IUE spectra with resolution 6 Å and is closer to 3×10^{12} cm^{-3} [9]. The relatively small signal-to-noise ratio of the RU Lup spectrum also prevents accurate determination of the structure of the SiIII] 1892 Å line around its maximum; i.e., we do not know if it really displays two peaks or if this is the effect of noise or the contribution of weak lines of other elements.

In connection with the question of faint lines, based on the above criteria, we suggest that the remaining emission features in Fig. 1 can be identified as follows: FeII 1895.69 Å ($a^2H_{11/2}$–$w^2G^0_{9/2}$); SI] 1900.29 Å

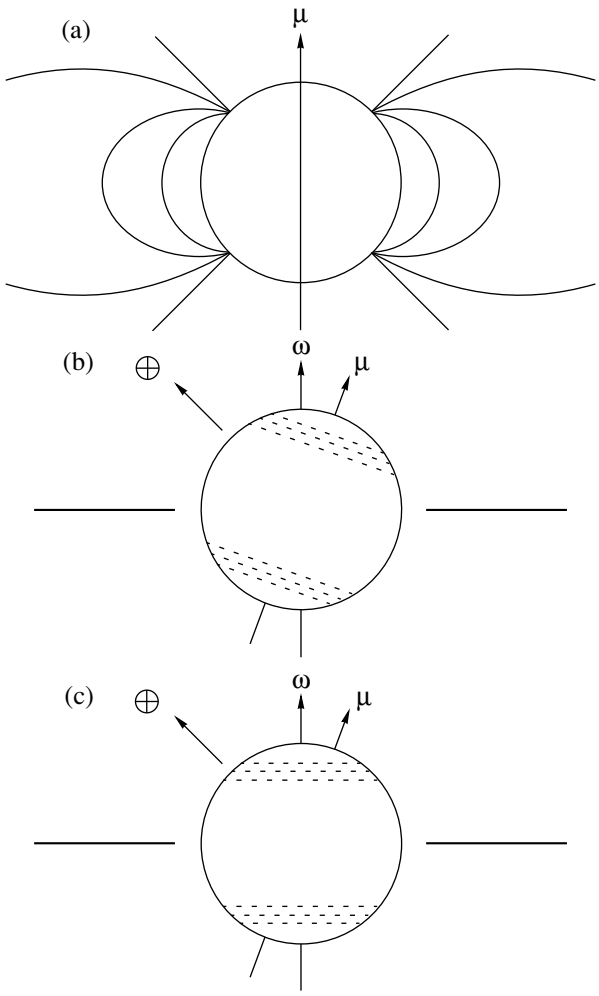

Fig. 3. (a) Shape of "quasi-dipole" field lines for $n = 1$ (inner curve), 2, 4, and ∞ (straight lines); accretion zone geometry for (b) Model 2 and (c) Model 3. See the text for more details.

$3p^4\,{}^3P_2$–$3p^3 4s5\,S_2^0$; note that the second component of this doublet ${}^3P_1$–$5S_2^0$ with λ = 1914.70 Å should have half the intensity, consistent with the observations); and FeII] 1901.77 Å ($a^6D_{9/2}$–$z^8G_{7/2}^0$). We especially note the possible presence of the FeIII 1914.06 Å line, which corresponds to the ${}^7S_3$–${}^7P_3^0$ transition of the $3d^5 4s$ configuration: The upper level of this transition could be excited due to absorption of photons from the short-wavelength wing (more exactly, with ΔV = –265 km/s) of the hydrogen L_α line. Judging from the presence of strong H_2 lines in the UV spectrum of RU Lup, which originate due to fluorescent excitation by the L_α line [11], this is very likely.

In the studied spectrum of RY Tau, both intercombinational lines (SiIII 1892 Å and CIII 1909 Å) can be identified with confidence (Fig. 2; see also Fig. 8 below). We can see that the lines have roughly the same intensity and total widths exceeding 350 km/s, which, as in the case of RU Lup, makes their formation in the stellar wind or the chromosphere unlikely. However, the quality of the spectrum makes it impossible to judge about the presence of other lines or the similarity of the profile shapes for the two ICLs.

3. METHOD FOR CALCULATING ICL PROFILES IN A SHOCK WAVE

If we assume, based on the above discussion, that the ICLs are formed neither in the stellar wind nor in the chromosphere, it makes sense to check whether their profiles can be understood as a consequence of accretion, given that accretion shock models can probably adequately reproduce both the absolute and relative intensities of ICLs in the UV spectra of other T Tauri stars [9]. In this case, the ICL radiation by the Si^{++} and C^{++} ions should form essentially completely at the shock front, in the region where the gas is highly ionized by X-rays from behind the shock front. (The basis for this and all following statements concerning the shock structure is given in [12].) It is essential that these regions be small in extent ($\Delta r \ll R_*$) and that both the density and velocity of the infalling gas be virtually constant (N_0 and $\simeq V_0$, respectively). Therefore, to model the ICL profiles, we need specify only the velocity field as a function of the coordinates of points on the stellar surface. The region itself can be taken to be plane-parallel.

Let us take an arbitrary point A at the surface of the accretion zone and calculate the flux dF_λ reaching the Earth from a region around this point with area dS in the wavelength interval from λ to λ + $d\lambda$. If $I_\lambda(\gamma)$ is the intensity of optically thin ICL radiation in the direction making an angle γ with the normal, then $I_\lambda(\gamma) = I_\lambda^0 \cos\gamma$, where I_λ^0 is the intensity of the radiation in the normal direction. Therefore,

$$dF_\lambda = \frac{I_\lambda(\gamma)\cos\gamma dS}{d^2} = \frac{I_\lambda^0 dS}{d^2},$$

where d is the distance to the star.

Let us introduce spherical coordinates with their origin at the center of the star and the polar axis coinciding with the star's rotation axis. The position of a point A will be described by the polar angle θ and the azimuth angle φ, with $dS = R_*^2 \sin\theta d\theta d\varphi$, where R_* is the radius of the star. Then, the total flux from the accretion zone will be

$$F_\lambda = \frac{R_*^2}{d^2}\iint I_\lambda^0 \sin\theta d\theta d\varphi. \qquad (1)$$

Due to the comparatively low temperature of the gas in the line formation region ($T < 2 \times 10^4$ K), the local

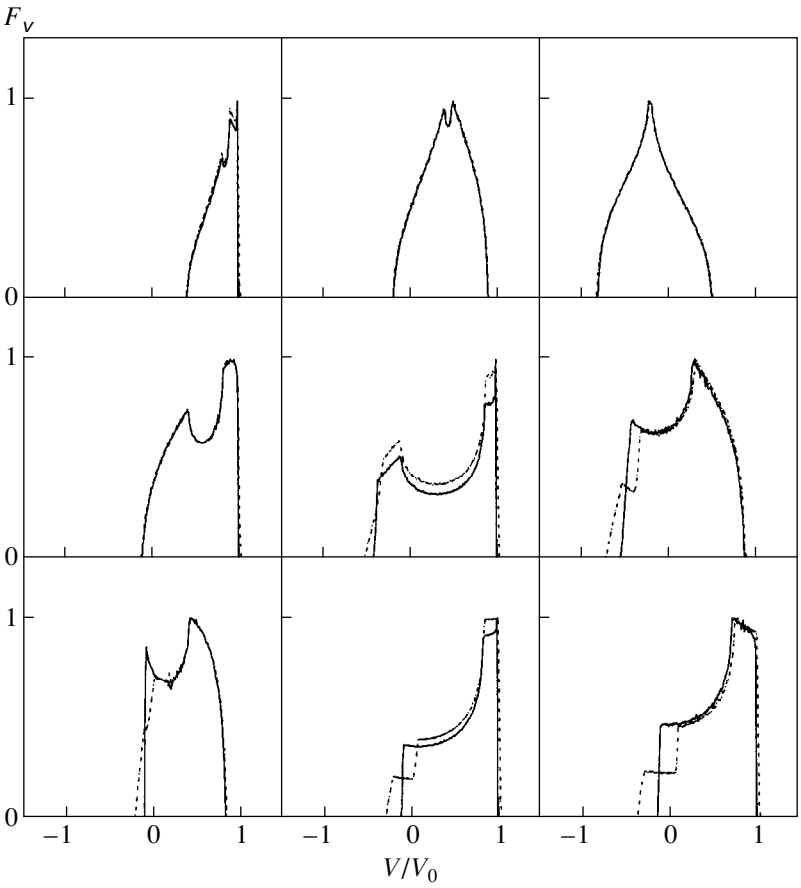

Fig. 4. ICL profiles for a coaxial quasi-dipole with $n = 2$ (Model 1). The left row of profiles corresponds to a zone with $\theta_1 = 10°$, $\theta_2 = 30°$ for inclination angles of the rotation axis to the line of sight (from top to bottom) $i = 20°$, 50°, and 70°; the middle row corresponds to a zone with $\theta_1 = 30°$, $\theta_2 = 50°$ and the right row to a zone with $\theta_1 = 50°$, $\theta_2 = 70°$ for the same inclination angles.

width of the ICL, which is determined by thermal motions, should not exceed 5 km/s, which is much lower than the velocity of the infalling gas, $V_0 \sim 300$ km/s. Therefore, the local line profile can be represented to good accuracy as a δ function. In this approximation, each point of the accretion zone emits towards the observer monochromatic radiation at the wavelength $\lambda = \lambda_0(1 + V_{rad}/c)$, where λ_0 is the laboratory wavelength of the ICL and $V_{rad}(\theta, \varphi)$ is the projection of the velocity of the infalling gas onto the line of sight at this point.

Let us assume that the velocity V_0 and the gas density N_0 are the same at all points of the accretion zone (the accretion is uniform). In this case, the observed flux inside a finite wavelength interval λ–$\lambda + \Delta\lambda$ (or the corresponding velocity interval V–$V + \Delta V$) is proportional to the area of the accretion zone in which the radiation in this wavelength interval originates. In order to determine the ICL profile, we adopt the following procedure:

(1) Specify the velocity field within the accretion zone and the zone geometry.

(2) Divide the largest possible interval for variations in V_{rad} in the accretion zone ($V_{\min}$–$V_{\max}$) into a sufficient number of equal subintervals.

(3) Divide the zone of interest into cells of equal size $\Delta\theta \times \Delta\varphi$ and calculate the value of V_{rad} in each of them (see formulae (A.6) and (A.7) in the Appendix).

(4) For each interval V_i–V_{i+1}, sum the values for $\sin\theta$ for cells whose radial velocity V_{rad} falls in the given interval and which are situated in the hemisphere facing the observer (see inequality (A.5) in the Appendix).

Then, by dividing the resulting sums by their maxima, we obtain ICL profiles normalized to unity as a function of radial velocity.

4. RESULTS FOR ICL PROFILE MODELING

Let us consider several simple accretion zone geometries and the corresponding velocity fields. For T Tauri stars, the velocity of the infalling gas cannot appreciably exceed 400 km/s, whereas the ICL in the spectrum of RU Lup is considerably broader. This implies that the accretion occurs in such an extended area that the

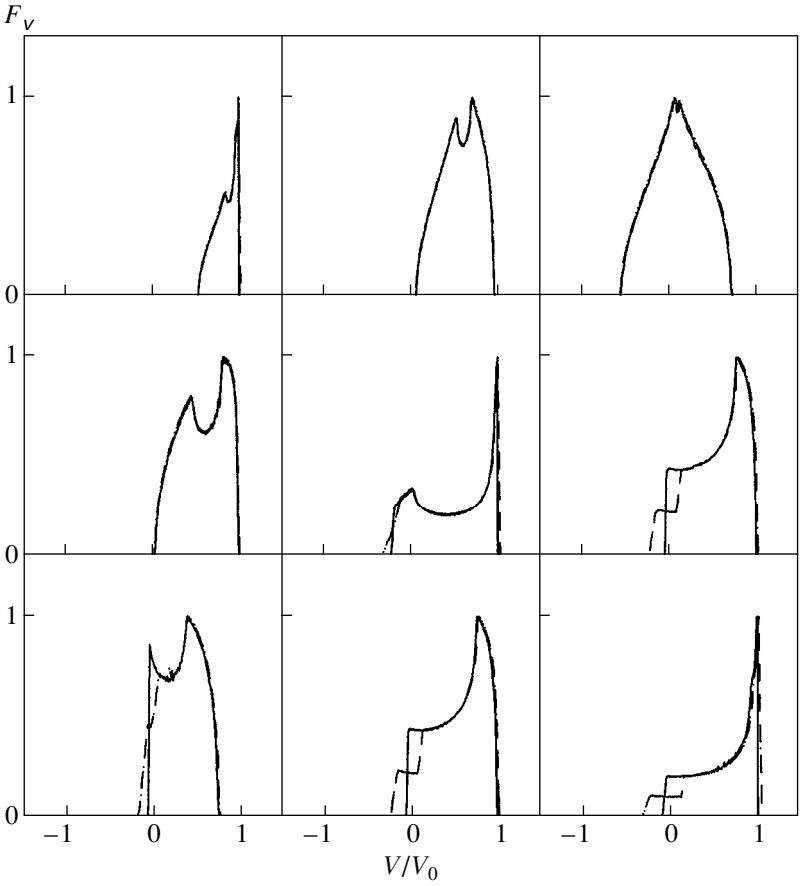

Fig. 5. Same as Fig. 4 for a quasi-dipole with $n = 4$.

effect of variation of the angle between the line of sight and the streamlines (due to the sphericity of the star) plays a substantial role. However, in this case, the accretion flux cannot be in the shape of a quasi-cylindrical gas stream occupying ~10% of the stellar surface, as suggested in [13].

In the accretion shock, the SiIII] 1892 Å and CIII] 1909 Å lines are formed essentially at the stellar surface so that these lines can only be seen from points in the accretion zone in the hemisphere facing the observer. It follows that, if the gas falls inward along the radius of the star, the radial velocity of visible emitting points should be positive, given that the lines are optically thin and have very narrow local profiles. Thus, the presence of extended short-wavelength wings in the observed ICLs implies that the velocity field of the infalling gas is appreciably nonradial.

Let us suppose that the gas infall occurs along the star's magnetic-field lines, whose shape near the stellar surface bears at least a qualitative resemblance to a dipole field. Let the field lines be described in polar coordinates r, Θ, Φ by the expression $r = R_*(\sin\Theta/\sin\Theta_*)^n$, where Θ_* is the polar angle at which a force line crosses the stellar surface and n is a parameter of the problem. When $n = 2$, we obtain a purely dipolar field, while for $n \longrightarrow \infty$, the force lines become straight lines (Fig. 3a).

Let us first consider the case when the "quasi-dipole" axis coincides with the rotation axis (Model 1). Due to the axial symmetry, the accretion zone should have the shape of two belts $\theta_1 \le \theta \le \theta_2$ and $\pi - \theta_2 \le \theta \le \pi - \theta_1$, with $0 \le \varphi < 2\pi$, where θ, φ are polar coordinates related to the rotation axis of the star. It follows from the calculations of [14] that the field of the star is strongly distorted in the case of disk accretion onto a coaxial dipole; however, we are interested only in the field in the immediate vicinity of the stellar surface, where the distortions are not so large. In fact, we chose the "quasi-dipole" approximation specifically to take these distortions into account; for the sake of simplicity, we will assume that both the velocity and density of the accreted plasma are equal at all points in the accretion belts. Another specific feature stemming from the calculations of [14] is that the field and velocity vector of the infalling material acquire a toroidal component, whose value reaches ~1/3 of the meridional component. In order to qualitatively take this into account, we will assume the presence of a toroidal component of the

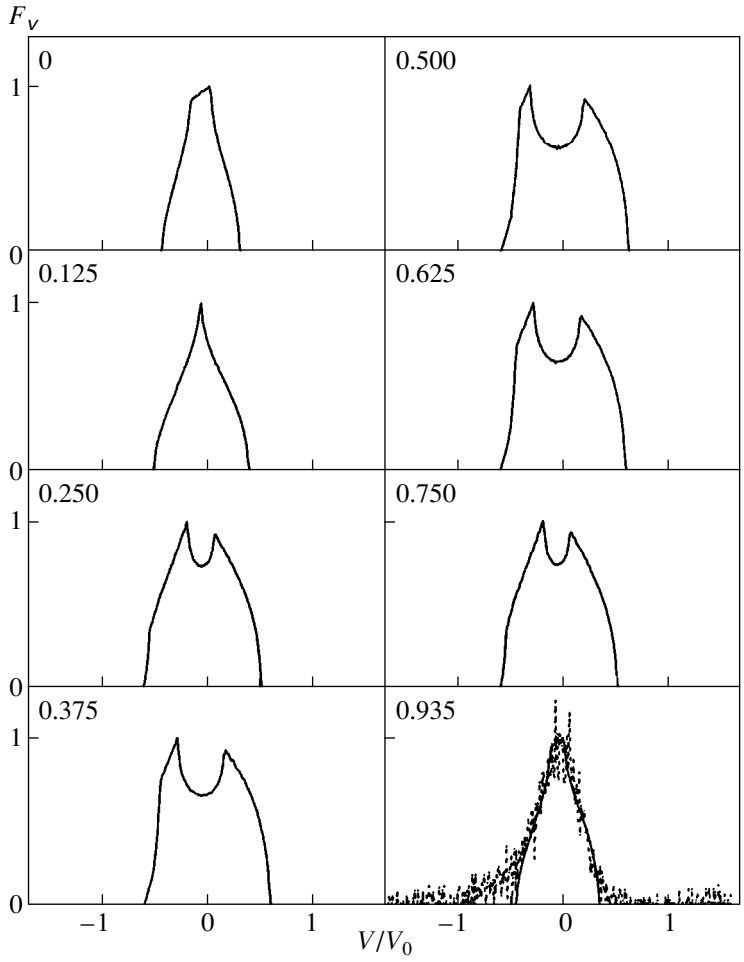

Fig. 6. Variation of the ICL profile shape in Model 2 as a function of rotation period phase, which is indicated for each curve. The observed profile of the SiIII] 1892 Å line from the spectrum of RU Lup is presented for phase $\psi = 0.935$. See the text for more details.

infall velocity that everywhere constitutes a constant fraction ξ of the meridional component V_0.

In the Appendix, we outline a procedure for deriving the radial velocity in the quasi-dipole case. In the situation considered here, we calculated V_{rad} using (A.6) and (A.7) for $\theta_m \equiv \theta$, $\varphi_m \equiv \varphi$, and $\alpha = \psi = 0$. Figure 4 presents the ICL profiles calculated using the technique described in the previous section, for the dipole-field geometry under consideration ($n = 2$). Inspection of the top-to-bottom sequence of plots indicates that the ICL profile depends on the location of the accretion belts on the stellar surface ($\theta_1, \theta_2 = 10°, 30°; 30°, 50°; 50°, 70°$); the left-to-right sequence of plots shows the dependence of the profile on the angle i between the stellar rotation axis and the line of sight ($i = 20°; 50°; 80°$). The solid curves show profiles calculated without taking into account the toroidal component of the velocity ($\xi = 0$), and the dashed curves show profiles for the case $\xi = 0.25$. Figure 5 presents the analogous dependences of the ICL profiles on the parameters of the problem for $n = 4$. We performed these calculations assuming only one accretion belt is visible (the one closer to the observer), since the other belt is obscured by the disk. The discontinuities of the derivative visible in the calculated profiles are due to the assumption that the local ICL profile has a δ-function shape.

We can see that the shape of the calculated profiles differs qualitatively from the ICL profiles in the spectra of RU Lup and RY Tau. It is obvious that taking into account the dependence of V_0 and ξ on θ will not enable us to substantially improve the agreement between the theory and observations. In other words, the origin for the disagreement must be the initial hypothesis that the quasi-dipole and rotation axes of the star are coincident.

We now assume that the magnetic axis makes an angle α with the rotation axis and that the field near the stellar surface resembles a quasi-dipole. Let us first consider the situation when α is not so large that the difference between the parameters of the infalling gas at different points of the accretion zone must be taken into account. In this case, it is reasonable to suppose that the accretion zone is made up of two belts perpendicular to the quasi-dipole axis (Model 2; Fig. 3b). In a

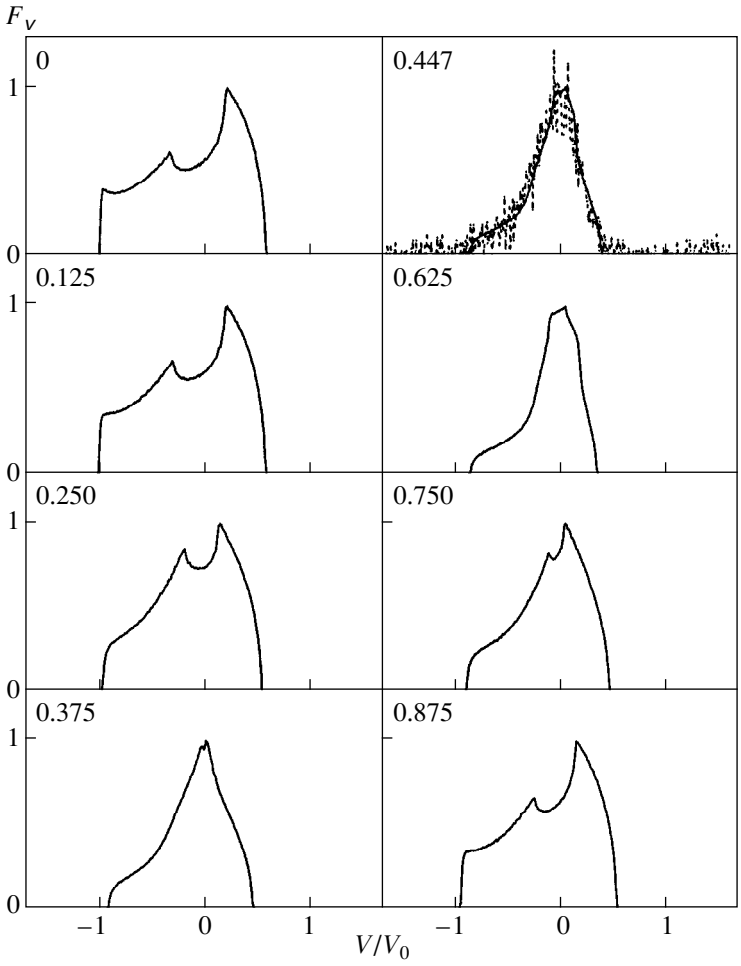

Fig. 7. Same as Fig. 6 for Model 3 and the set of free parameters indicated in the text. The observed SiIII] 1892 Å line profile from the spectrum of RU Lup is shown for phase $\psi = 0.447$.

coordinate frame fixed to the quasi-dipole axis, the accretion region is determined by the conditions $\theta_{m1} \le \theta_m \le \theta_{m2}$ and $\pi - \theta_{m2} \le \theta_m \le \pi - \theta_{m1}$, with $0 \le \varphi_m < 2\pi$. As before, we will take into account radiation only from a single accretion belt (the one closer to the observer).

The orientation of the accretion belt relative to the observer will periodically vary due to the movement of the magnetic pole on the surface of the star during its rotation. For this reason, the ICL profiles should undergo periodic variations, unlike the situation when $\alpha = 0$. Mathematically, this implies that the expression for the radial velocity V_{rad} (formulas (A.6) and (A.7) in the Appendix) does not depend only on the angle α, but also on the rotation phase ψ. We calculated the variations of the ICL profiles for the given geometry during the rotation of the star for various values of i, α, θ_{m1}, θ_{m2}, ξ, and n. For $\alpha \le 10°$, we were not able to obtain reasonable consistency between the calculated profiles and the ICL profiles in the observed spectrum of RY Tau. For RU Lup, we were able to obtain a better agreement between the calculated profiles and the SiIII] 1892 Å line profile; however, the corresponding model cannot provide a sufficiently extended short-wavelength wing. Figure 6 presents the expected variations of the ICL profile as a function of the phase of the axial rotation for $i = 18°$, $\alpha = 10°$, $\theta_{m1} = 58°$, $\theta_{m2} = 71°$, $\xi = 0.15$, and $n = 4$. For phase $\psi = 0.935$, we have plotted the observed profile assuming $V_0 = 400$ km/s. Note that, in both Model 1 and Model 2, the velocity field is symmetrical about the magnetic axis.

What will happen if the angle between the magnetic and rotation axes of the star becomes fairly large, say, appreciably greater than 10°? We can see from Fig. 3b that, in this case, points with the same θ_m but different φ_m will be located at considerably different distances from the accretion disk. In this situation, it is very unlikely that the accretion zone is made up of belts symmetrically placed relative to the magnetic axis, inside of which the velocity and density of the infalling gas are uniform. There do not exist any reliable calculations for the magnetic-field topology for the case of disk accretion onto an inclined rotator that we could use to calculate the ICL profiles for this case. Remaining in

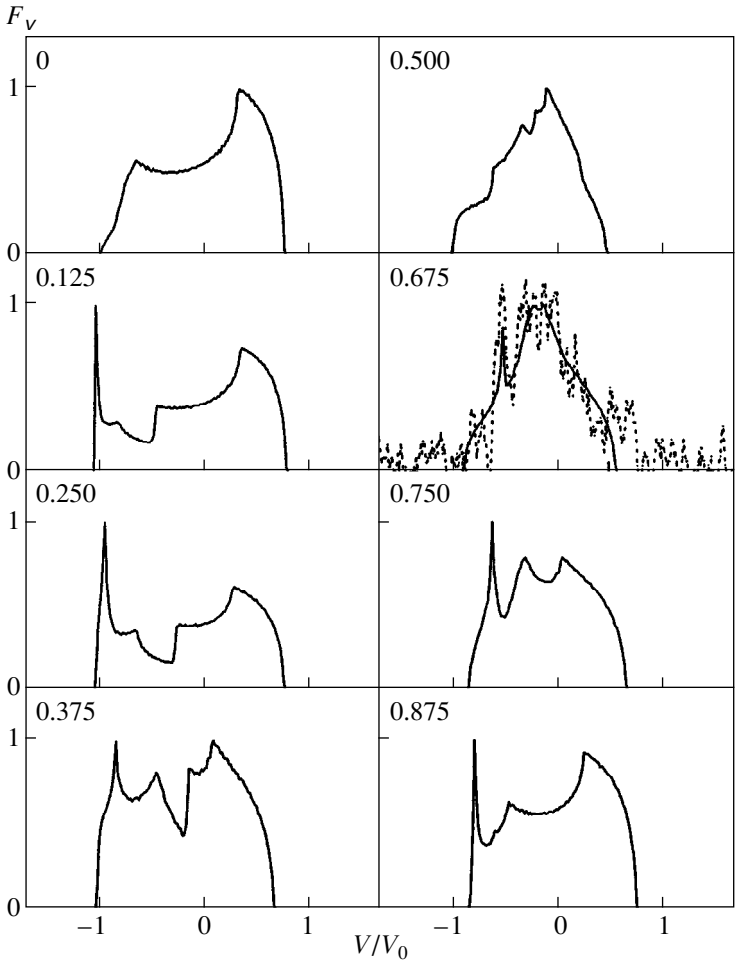

Fig. 8. Same as Fig. 7 for another set of free parameters. The observed SiIII] 1892 Å line profile from the spectrum of RY Tau is shown for phase $\psi = 0.675$. See the text for more details.

the framework of the uniform-accretion hypothesis, we can make the model more realistic by assuming that the field topology near the stellar surface does not differ too much from the field of an inclined quasi-dipole with a toroidal component (Model 2) but that the accretion zones are symmetrically placed relative to the rotation axis (Fig. 3c). This Model 3 represents a combination of the two preceding models; however, in contrast to Models 1 and 2, its appropriateness for the situation at hand is far from obvious.

Surprisingly, it was this model that was able to reproduce the observed SiIII] 1892 Å line profiles. For RU Lup, we were able to reach a good agreement for $i = 12°$, $\alpha = 18°$, $\theta_1 = 56°$, $\theta_2 = 72°$, $\xi = 0.15$, $V_0 = 400$ km/s, and $n = 4$. Figure 7 presents the observed profile for phase $\psi = 0.447$. Figure 8 presents a series of calculated profiles for $i = 36°$, $\alpha = 18°$, $\theta_1 = 60°$, $\theta_2 = 80°$, $\xi = 0.25$, $V_0 = 280$ km/s, and $n = 4.25$. We can see that, for $\psi = 0.675$, the theoretical profile approximates the SiIII] 1892 Å line profile in the spectrum of RY Tau with reasonable accuracy, provided the two-humped profile shape is real.

We stress that our ability to reproduce the observed profiles using Model 3 does not imply that this model, indeed, provides an adequate description of the physical situation. The consistency obtained only demonstrates the fundamental possibility of interpreting observed ICL profiles using shock models in which the velocity field in the accretion zone is appreciably nonaxisymmetric.

5. CONCLUSIONS

Our analysis of the SiIII] 1892 Å and CIII] 1909 Å line profiles in the spectra of RY Tau and RU Lup indicates that these lines cannot form in regions similar to the solar chromosphere. It is also unlikely that a large fraction of the line flux is formed in shock waves due to interactions between the stellar wind and the surrounding medium (i.e., in Herbig–Haro objects).

If we assume that the SiIII] 1892 Å and CIII] 1909 Å lines are formed in an accretion shock, the observed profile shapes can be used to impose some restrictions on the character of accretion in low-mass young stars: (1) The velocity field of the infalling gas is substantially

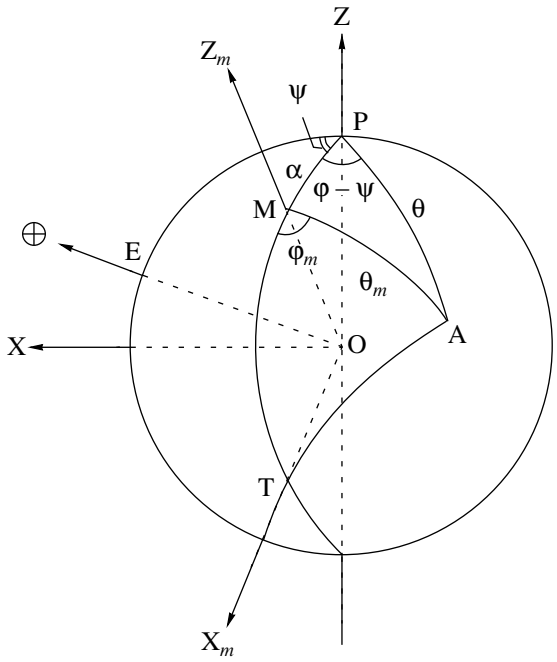

Fig. 9. A scheme clarifying the derivation of formulas (A.1)–(A.7). See text for more detail.

nonradial, (2) the accretion zone must be appreciably extended along the stellar disk, (i.e., accretion in the form of an isolated quasi-cylindrical stream is excluded), and (3) the structure of the magnetic field directing the infalling gas must be considerably nonaxisymmetric.

This last circumstance suggests there should be periodic variations of the profiles of line formed in the shock, due to variations in the orientation of the accretion zone relative to the observer. For the same reason, the 0.3–0.7 keV X-ray flux from T Tauri stars should also vary periodically. In this case, nonstationary accretion will distort the periodicity of the X-ray flux variations much less than it will the line-profile variations, since the X-ray flux depends only weakly on the density of the infalling gas [15].

Since only one spectrum is available for each star and it is not of very high quality, it does not make sense to try to reconstruct the velocity field and geometry of the accretion zone. We wished only to demonstrate that the observed ICL profiles could be reproduced in the framework of an accretion shock theory, which is not at all obvious *a priori*. As a result, it is now clear that it is a reasonable goal to investigate ICL profile variations in the UV spectra of T Tauri stars, then apply Doppler tomography to reconstruct the accretion zone geometry and velocity field. In the theoretical model, expression (1) should be used for the dependence of the intensity on the angular coordinates, together with the relation between the intensity and N_0 and V_0 for the infalling gas from [9]. Naturally, the local ICL profile should be described as a Gaussian rather than a δ function, whose width is determined by the thermal motion of gas with temperature $\simeq 1.5 \times 10^4$ K.

ACKNOWLEDGMENTS

The author is grateful to the Hubble Space Telescope Science Institute for permission to access the Space Telescope Archive. He also thanks A.I. Gomez de Castro for useful discussions and comments and A.Yu. Zaĭtsev for assistance with the IRAF-STSDAS package, as well as with the Atomic Line List v.2 database.

APPENDIX

Figure 9 presents a star whose center is marked by the O; the line OE indicates the direction towards the Earth. Let us introduce a rectangular (right-handed) coordinate frame with its origin at O, its Z axis coinciding with the rotation axis of the star and its X axis in the plane determined by the lines OE and OZ. We will name EOP the inclination angle *i*. Let us relate the spherical coordinate system to this rectangular system in the standard way, so that, for some point A on the stellar surface, the arc PA will serve as the polar angle θ and the dihedral angle between the arcs EP and PA will be the azimuthal angle φ. The θ, φ coordinates of the point A obviously do not depend on time.

If the magnetic quasi-dipole axis forms an angle $\alpha > 0$ with the rotation axis of the star, the magnetic pole M will move on the surface of the star. In so doing, its polar angle $\theta_M = \alpha$ does not vary, unlike the azimuthal coordinate $\varphi_M \equiv \psi$ of the dihedral angle between the arcs EP and PM (Fig. 9). Let us introduce another right-sided rectangular coordinate frame with its origin at O, its Z_m axis directed along the quasi-dipole axis, and its X_m axis directed as shown in the diagram (Fig. 9), so that $\angle MOT = \pi/2$. As in the previous case, let us relate the spherical coordinate system with this rectangular system. As we can see from Fig. 9, the large circular arc MA is the polar angle θ_m of the point A in the new coordinate system, while the dihedral angle between arcs MA and MT is its azimuthal angle φ_m. The coordinates θ_m, φ_m vary periodically due to the rotation of the star about its axis.

Let us derive relations between the coordinates θ, φ and θ_m, φ_m of the point A. Applying spherical trigonometry to the triangles PMA, MTA, and PTA [16], we obtain the relations

$$\cos\theta = \cos\alpha\cos\theta_m - \sin\alpha\sin\theta_m\cos\varphi_m, \quad (A.1)$$

$$\cos\theta_m = \cos\alpha\cos\theta + \sin\alpha\sin\theta\cos(\varphi - \psi), \quad (A.2)$$

and also

$$\begin{cases} \sin\theta\sin(\varphi - \psi) = \sin\theta_m\sin\varphi_m \\ \cos\alpha\sin\theta\cos(\varphi - \psi) = \sin\theta_m\cos\varphi_m + \sin\alpha\cos\theta. \end{cases}$$

After corresponding transformations, we obtain

$$\begin{cases} \sin\theta\sin\varphi = \sin\theta_m\sin\varphi_m\cos\psi + f_0\sin\psi \\ \sin\theta\cos\varphi = f_0\cos\psi - \sin\theta_m\sin\varphi_m\sin\psi, \end{cases} \quad (A.3)$$

where $f_0 = \sin\alpha\cos\theta_m + \cos\alpha\sin\theta_m\cos\varphi_m$, and

$$\begin{cases} \sin\theta_m\sin\varphi_m = \sin\theta\sin(\varphi-\psi) \\ \sin\theta_m\cos\varphi_m = \sin\theta\cos(\varphi-\psi)\cos\alpha - \sin\alpha\cos\theta. \end{cases} \quad (A.4)$$

Relations (A.1) and (A.3) make it possible to make a unique transformation from coordinates in the rotating system to coordinates in the fixed system, while formulas (A.2) and (A.4) provide the inverse transformation.

The observer will see the point A if the angle between the vectors OE and OA does not exceed $\pi/2$. Since these unit vectors have coordinates $(\sin i; 0; \cos i)$ and $(\sin\theta\cos\varphi; \sin\theta\sin\varphi; \cos\theta)$, respectively, in the rectangular system OXYZ the condition that point A be visible can be written

$$\cos(\angle\mathrm{EOA}) = \cos i\cos\theta + \sin i\sin\theta\cos\varphi \geq 0. \quad (A.5)$$

Let the shape of the magnetic field lines of the star $r = r(\Theta)$ be described in the "magnetic" coordinate system by the equation $r = R(\sin\Theta_m/\sin\theta_m)^n$, where R is the radius of the star and θ_m is the polar angle of the point A, where a line of force crosses the stellar surface. This field possesses only a meridional component. Let $\mathbf{e}_\mathrm{M}$ be a unit vector in the meridional plane, tangent to the force line at the point A and directed towards the star. It is easy to show that the projections of this vector onto the coordinate axes of the $\mathrm{OX}_m\mathrm{Y}_m\mathrm{Z}_m$ system are equal to $w_1\cos\varphi_m$, $w_1\sin\varphi_m$, and w_2, where $w_1 = -(n+1)\sin2\theta_m/w_0$, $w_2 = 2(\sin^2\theta_m - n\cos^2\theta_m)/w_0$, and $w_0 = 2[n^2\cos^2\theta_m + \sin^2\theta_m]^{1/2}$.

If gas moves near the surface of the star along magnetic field lines, with the velocity of infall V_0 equal at all points of the accretion zone, then $\mathbf{V} = V_0\mathbf{e}_\mathrm{M}$. At an arbitrary point A, the component of the velocity V^M_{rad} along the line of sight is $\mathrm{EO}\cdot V$. Expressing the coordinates of the vector EO in the rotating frame using relations (A.2) and (A.4), we obtain

$$\frac{V^\mathrm{M}_{rad}}{V_0} = w_1(f_1\cos\varphi_m + f_2\sin\varphi_m) - w_2(\cos i\cos\alpha + \sin\alpha\sin i\cos\psi), \quad (A.6)$$

where $f_1 = \sin\alpha\cos i - \sin i\cos\alpha\cos\psi$ and $f_2 = \sin i\sin\psi$.

Assume now that, in addition to the meridional "quasi-dipole" component, the stellar magnetic field also possesses a toroidal φ_m component. In this case, the total velocity of the infalling gas can be represented as a sum of meridional $V_0\mathbf{e}_\mathrm{M}$ and toroidal $\chi V_0\mathbf{e}_T$ components, where $\mathbf{e}_T$ is the unit φ_m vector for the point A and ξ is the ratio of the amplitudes of the toroidal and meridional velocities. The projections of the vector $\mathbf{e}_T$ onto the axes of the rotating coordinate system are $-\sin\varphi_m$, $\cos\varphi_m$, and 0. As above, we find that the component of the radial velocity relative to the gas motion in the toroidal direction and the total radial velocity are equal to

$$\frac{V^T_{rad}}{V_0} = \xi(f_2\cos\varphi_m - f_1\sin\varphi_m), \qquad V_{rad} = V^M_{rad} + V^T_{rad}. \quad (A.7)$$

REFERENCES

1. E. Gullbring, P. P. Petrov, I. Ilyin, *et al.*, Astron. Astrophys. **314**, 835 (1996).
2. A. I. Gómez de Castro and M. Franqueira, Astrophys. J. **482**, 465 (1997).
3. K. W. Smith, G. F. Lewis, I. A. Bonnell, *et al.*, Mon. Not. R. Astron. Soc. **304**, 367 (1999).
4. Y. C. Unruh, A. Collier Cameron, and E. Guenther, Mon. Not. R. Astron. Soc. **295**, 781 (1998).
5. A. I. Gómez de Castro and M. Franqueira, *ULDA Access Guide to T Tauri Stars Observed with IUE* (ESA, Noordwijk, 1997b).
6. S. N. Hahar, Astron. Astrophys. **293**, 967 (1995).
7. F. Hamann, Astrophys. J., Suppl. Ser. **93**, 485 (1994).
8. C. L. Imhoff and I. Appenzeller, in *Exploring the Universe with IUE Satellite*, Ed. by Y. Kondo (Reidel, Dordrecht, 1989), p. 295.
9. S. A. Lamzin, G. S. Bisnovatyĭ-Kogan, L. Érrico, *et al.*, Astron. Astrophys. **306**, 877 (1996).
10. A. I. Gómez de Castro and S. A. Lamzin, Mon. Not. R. Astron. Soc. **304**, L41 (1999).
11. S. A. Lamzin, Pis'ma Astron. Zh., 2000 (in press).
12. S. A. Lamzin, Astron. Zh. **75**, 367 (1998).
13. P. F. C. Blondel, A. Talavera, A. Tjin, *et al.*, Astron. Astrophys. **268**, 624 (1993).
14. K. A. Miller and J. M. Stone, Astrophys. J. **489**, 890 (1997).
15. S. A. Lamzin, Pis'ma Astron. Zh. **25**, 505 (1999).
16. K. A. Kulikov, *A Course in Spherical Astronomy* (Nauka, Moscow, 1978).

Translated by K. Maslennikov

Astronomy Reports, Vol. 44, No. 5, 2000, pp. 334–337. Translated from Astronomicheskiĭ Zhurnal, Vol. 77, No. 5, 2000, pp. 385–389.

G0–G5V Stars and the Sun in the *uvby* System

L. N. Knyazeva and A. V. Kharitonov

Fesenkov Astrophysical Institute, Kazakh Academy of Sciences, Kamenskoe Plato, Almaty, 480068 Kazakhstan

Received April 30, 1999

Abstract—The color indices of the Sun in the *uvby* system are calculated using the spectral energy distribution of Lockwood, Tug, and White. This allows errors in the absolute calibration to be excluded from the calculated color indices. The normal position of the Sun on the $(v-b)$–$(b-y)$ and $(v-y)$–$(b-y)$ color–color diagrams for early G stars testifies to the absence of any significant peculiarities in the Sun compared to other stars of similar spectral type. These diagrams can provide a useful tool in searches for candidate solar analogues among faint stars. © *2000 MAIK "Nauka/Interperiodica".*

1. INTRODUCTION

The *uvby* photometric system [1] is very promising for searches for candidate solar analogues [2]. An extensive *uvby* catalog containing a large number of stars with spectral types close to that of the Sun has been compiled [3]. This system was originally created for A–F stars, and proved to be a useful tool for studies of stars of these spectral types. The $b-y$ color index is similar to the $B-V$ index of the *UBV* system ($b-y$ is a temperature parameter), $m_1 = (v-b)-(b-y)$ reflects the blanketing effect near $\lambda \sim 4100$ Å, and $c_1 = (u-v)-(v-b)$ is a measure of the Balmer discontinuity. Later, this system was extended to early G stars (G0–G5).

We are interested in the question of which indices or color indices in the *uvby* system could be useful in searches for candidate solar analogues. The c_1 index is of little interest for this purpose, since it displays no correlation with $b-y$ [4] or other color indices for early G stars. A comparison of the m_1–$(b-y)$ and $(v-y)$–$(b-y)$ color–color diagrams (Figs. 1, 2) for F0–G5 main-sequence stars based on the data of [3] indicates that using $v-b$ instead of m_1 affects only the behavior of early F stars. For late F and early G stars, $v-b$ and m_1 show identical $b-y$ dependences. However, since the accuracy of a color index is higher than that of a quantity constructed from the difference of two color indices, we prefer to use $v-b$. The $v-y$ color index for early G stars also displays a good dependence on $b-y$ (Fig. 3). These diagrams can be used in searches for candidate solar analogues once we determine the color indices for the Sun in this photometric system.

There are a number of indirect determinations of $b-y$ for the Sun in the literature. Some of these are based on the relationship between $b-y$ and $B-V$; because of uncertainties in *UBV* for Sun, these have a relatively large scatter, from 0.395^m to 0.425^m [5–9]. Other indirect determinations are based on the dependence of $b-y$ on $T_{\rm eff}$ [10–12]; these studies yield $b-y = 0.407^m$, 0.402^m, and 0.404^m, respectively. We have calculated the color indices of the Sun in the *uvby* system, based on the observed solar spectral energy distribution and the response curves of this photometric system.

2. SYNTHETIC COLOR INDICES

The color indices of a star can be calculated in any photometric system if a reliable spectral energy distribution (SED) and the response curves of the system are available. A formula modeling photometric observations in the system (either in the absence of or taking into account atmospheric extinction) is used:

$$m_i - m_j = -2.5\log\left(\int E_*(\lambda)\varphi_i(\lambda)d\lambda \Big/ \int E_*(\lambda)\varphi_j(\lambda)d\lambda\right) + C_{ij}. \quad (1)$$

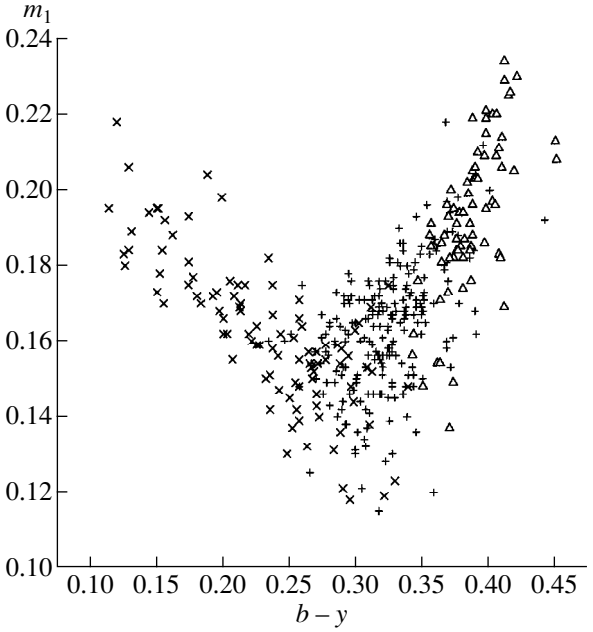

Fig. 1. $(b-y)$–m_1 color–color diagram for F0–G5 main-sequence stars. Crosses: F0–F4 stars; pluses: F5–F9 stars; triangles: G0–G5 stars.

1063-7729/00/4405-0334$20.00 © 2000 MAIK "Nauka/Interperiodica"

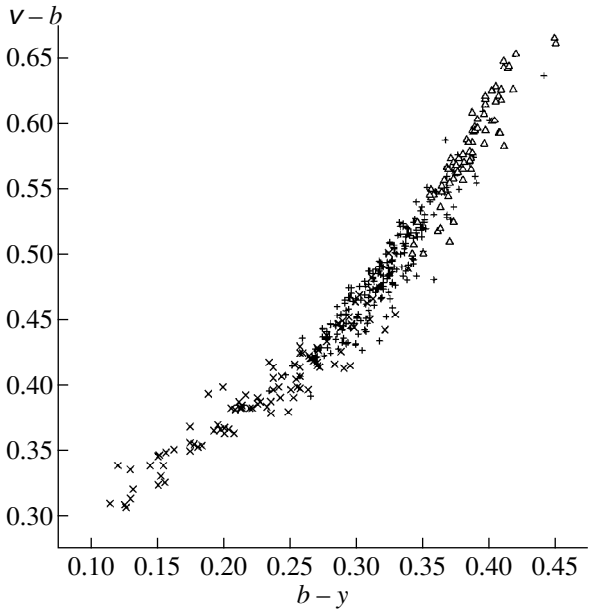

Fig. 2. $(b-y)$–$(v-b)$ color–color diagram for F0–G5 main-sequence stars. Crosses: F0–F4 stars; pluses: F5–F9 stars; triangles: G0–G5 stars.

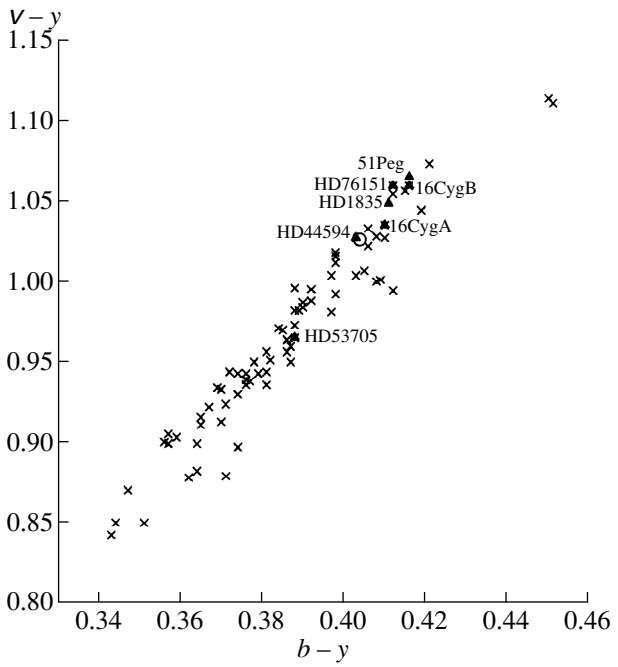

Fig. 3. $(b-y)$–$(v-y)$ color–color diagram for G0–G5 main-sequence stars. Crosses: G0–G5 stars, open circle: the Sun; triangles: stars from the list of solar analogues [12].

Here, $E_*(\lambda)$ is the SED of the star in the interval covered by the system response curve, $\varphi_i(\lambda)$ and $\varphi_j(\lambda)$ are the response curves of the photometric system in the i and j filters, and $C_{ij} = (m_i - m_j)_H - (m_i - m_j)_B$ is a constant defining the zero point of the calculated color indices. This constant is determined using a star with a known SED, based on the difference between the observed color index and the index for the photometric system considered calculated using the known SED and the first term of (1).

We estimated the accuracy of our calculated color indices by comparing them with the observed indices for stars in three photometric systems: *uvby* [3], *WBVR* [13], and the Vilnius system [14]. For this purpose, we selected groups of single, nonvariable, main-sequence stars of spectral types F0–G5 from the catalog [15] for which observations in these systems are available. The three lists of stars substantially overlap. The accuracy of the SEDs of these stars is 1.5–2% from 4000 to 6000 Å, falling to 2–3% at the violet and red edges. The response curves were taken from [16] (*uvby*), [13] (*WBVR*), and [17] (Vilnius).

We fixed the zero point using two sources of data on the energy distribution in the integrated spectrum of Vega [15, 18]. The absolute calibration at continuum points free of absorption was identical in both cases, but blanketing due to the Balmer lines was taken into account differently. The resulting differences of the constants defining the zero point in the three photometric systems was 0.02^m. The constants determined using the Vega data from [15] yield color indices that are in better agreement with the observed indices (within 1–1.5%) in all three systems. Using the data of [18] to fix the zero point worsens this agreement. We conclude that the SED for Vega presented in [15] better accounts for blanketing, which plays an important role when calculating color indices, and precisely these data should be used to establish the zero point.

The table lists a comparison of the observed and calculated color indices in the three photometric systems; n is the number of stars used, Δ is the mean difference between the observed and calculated color indices, and $\sigma = \sqrt{\Sigma}\,(\Delta_{mean} - \Delta_i)^2/n$. This table shows that the accuracy of the calculated color indices can be comparable to the accuracy of the observed indices if (1) the response curves for the photometric systems are well known, (2) the SEDs of the stars are known to no worse than 2%, and (3) we have reliable data on the SED of the star determining the zero point of the calculated color indices. The good agreement between the observed and calculated color indices of the stars in the three photometric systems confirms the trustworthiness of the response curves used. All these considerations are also relevant for calculation of the solar color indices.

3. COLOR INDICES OF THE SUN IN THE *uvby* SYSTEM

The solar SED can be derived from comparisons with standard sources, which are calibrated against a primary standard—a model blackbody. The procedure for calibrating data for the Sun is rather laborous, and,

Comparison of calculated and observed color indices in three photometric systems

UPXYZVS (n = 35)	
$\Delta(U–P)_{mean}$	0.015
$\sigma\{\Delta(U–P)\}$	0.031
$\Delta(P–X)_{mean}$	0.003
$\sigma\{\Delta(P–X)\}$	0.030
$\Delta(X–Y)_{mean}$	0.000
$\sigma\{\Delta(X–Y)\}$	0.018
$\Delta(Y–Z)_{mean}$	0.011
$\sigma\{\Delta(Y–Z)\}$	0.018
$\Delta(Z–V)_{mean}$	−0.015
$\sigma\{\Delta(Z–V)\}$	0.041
uvby (n = 47)	
$\Delta(b–y)_{mean}$	−0.006
$\sigma\{\Delta(b–y)\}$	0.013
$\Delta(v–b)_{mean}$	0.001
$\sigma\{\Delta(v–b)\}$	0.012
$\Delta m1_{mean}$	0.007
$\sigma\{\Delta m1\}$	0.019
WBVR (n = 64)	
$\Delta(W–B)_{mean}$	0.014
$\sigma\{\Delta(W–B)\}$	0.034
$\Delta(B–V)_{mean}$	−0.009
$\sigma\{\Delta(B–V)\}$	0.015

in many respects, the quality of the result depends on how reliably the energy scale has been transferred from the primary standard to the Sun. When calibrating data for the Sun, different authors have used different standard sources calibrated in different laboratories, and no mutual comparison has been performed. There are considerable discrepancies among the best known determinations of the solar SED [19–22], which increase in the ultraviolet (to 10%) and red (up to 6%), possibly due to the effect noted above. We decided to use the data of Lockwood *et al.* [21], since these were the only data for which it was possible to eliminate errors associated with the absolute calibration. Lockwood *et al.* [21] calibrated the solar spectrum against Vega, using the absolute energy distribution they had obtained earlier [23]. The advantage of these data is that by fixing the zero-point using data for Vega presented in the same energy scale as the Sun, we can exclude the error introduced by the absolute calibration, since these errors will appear in the two terms of formula (1) with opposite signs.

Below, we present the calculated solar color indices based on the data of [21] and the response curves [16].

$$u - v = 0.994,$$
$$b - y = 0.404,$$
$$m_1 = 0.217,$$
$$c_1 = 0.373,$$
$$v - b = 0.621,$$
$$v - y = 1.025.$$

The constants were obtained for Vega using the SED from [15], reduced to the absolute calibration of Tug *et al.* [23]. The calculated value of $b - y$ is consistent with that derived from the dependence of T_{eff} on $b - y$ from [12], with T_{eff} for the Sun taken to be 5777 K. If we can be confident of the reliability of the $T_{eff} - (b - y)$ relationship derived in [12], this suggests that the relative behavior for the solar SED obtained by Lockwood *et al.* [21] in the spectral region we have considered is close to the true distribution. However, the error of $b - y$ given in [12] (0.005^m) seems to be underestimated, and the good coincidence may be accidental.

The Sun's calculated color indices are shown in the color–color diagrams in Figs. 3 and 4, constructed for G-star data together with data for candidate solar analogues approved by the working group [2]. There is only one star near the Sun, HD 44594 (BS 2290), whose effective temperature is equal to the solar value [12]. This suggests that the solar color indices we have obtained are quite trustworthy. The Sun lies on both sequences in a natural way, testifying to the absence of any significant peculiarities in the Sun compared to other early G stars.

The anomalous position of the solar color indices on the $(U - B)$–$(B - V)$ color–color diagram is most likely associated with errors in the observed solar color indices; these were derived from direct comparisons of the Sun and other stars, require a large number of reductions, and depend on the choice of comparison stars. In the *WBVR* system [24], we plotted solar indices calculated from the mean energy distribution of [25] on a color–color diagram constructed using the observational data for other stars. The error of the zero-point shifts the Sun in one or the other direction in both coordinates. We discussed this problem in [26]. We calculated new solar color indices in the *WBVR* system using the procedure described above. We obtained the values $W - B = -0.025^m$ and $B - V = 0.656^m$, which shift the former position of the Sun on the $(W - B)$–$(B - V)$ color–color diagram blueward. Note that the normal color indices of G2V stars calculated using the normal energy distribution for stars of this spectral subtype [27] are perfectly consistent with these values ($W - B = -0.025^m$, $B - V = 0.663^m$).

Based on the $b - y$ color index for the Sun, we have selected stars from catalog [3] that have $b - y$ values close to the solar value (±0.005). This yields a rather

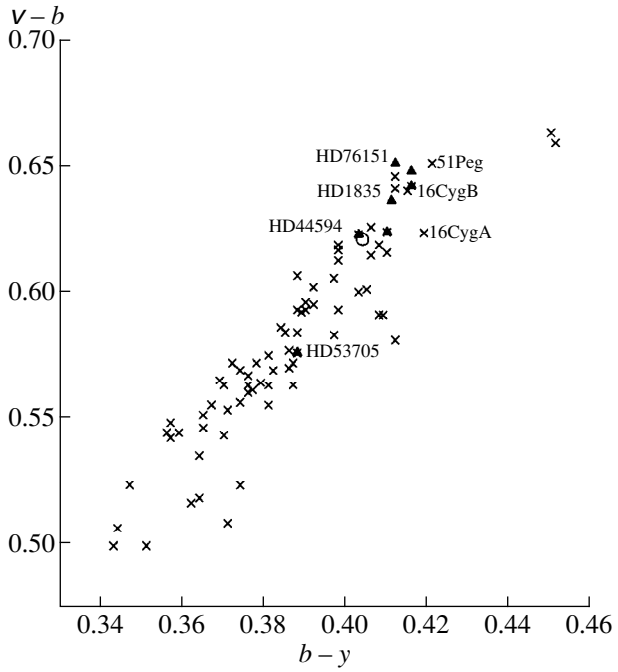

Fig. 4. $(b-y)$–$(v-b)$ color–color diagram for G0–G5 main-sequence stars. Crosses: G0–G5 stars; open circle: the Sun; triangles: stars from the list of solar analogues [12].

long list of candidates, which we will analyze in a future paper. We believe that, in combination with $b-y$, the $v-b$ and $v-y$ color indices can provide a good tool for searches for candidate solar analogues among faint G stars, as well as for constructing an effective-temperature scale for stars of this type.

4. CONCLUSION

The main results of the work are the following:

(1) It is possible to obtain accuracies in calculated color indices that are comparable to those of the observed magnitudes if we have (1) accurate response curves for the photometric system under consideration, (2) trustworthy SEDs for the stars studied, and (3) accurate data on the SED of the star used to determine the zero point of the calculated color indices. This last point, in particular, is a very important factor.

(2) We have calculated color indices and the indices m_1 and c_1 for the Sun in the *uvby* system by convolving its SED [21] with the response curves for this system. Using this solar SED allows us to eliminate errors in the absolute calibration from the calculated color indices.

(3) The position of the Sun on the $(v-b)$–$(b-y)$ and $(v-y)$–$(b-y)$ color–color diagrams for early G stars is quite normal, testifying to the absence of any significant peculiarities in the Sun compared to these stars. These diagrams can provide a useful tool for searching for candidate solar analogues among faint stars.

ACKNOWLEDGMENTS

We express our sincere gratitude to V.M. Tereshchenko for useful comments made during discussions of this work.

REFERENCES

1. D. L. Crawford and J. V. Barnes, Astron. J. **75**, 978 (1970).
2. *Proc. Second Annual Lowell Fall Workshop*, Ed. by J. C. Hall (Flagstaff, 1998).
3. B. Hauck and M. Mermilliod, Astron. Astrophys. Suppl. Ser. **86**, 107 (1990).
4. V. Straižhis, *Multicolor Stellar Photometry* (Mokslas, Vilnius, 1977).
5. E. H. Olsen, Astron. Astrophys. **50**, 117 (1976).
6. Y. Chmielevski, Astron. Astrophys. **93**, 334 (1981).
7. T. Gehren, Astron. Astrophys. **100**, 97 (1981).
8. A. Ardeberg, H. Lindgren, and P. E. Nissen, Astron. Astrophys. **128**, 194 (1983).
9. D. F. Gray, Publ. Astron. Soc. Pacif. **104**, 1035 (1992).
10. M. Saxner and G. Hammarback, Astron. Astrophys. **151**, 372 (1985).
11. P. Magain, Astron. Astrophys. **181**, 323 (1987).
12. G. Cayrel de Strobel, Ann. Rev. Astron. Astrophys. **7**, 243 (1996).
13. V. G. Kornilov, I. M. Volkov, A. I. Zakharov, *et al.*, Tr. Gos. Astron. Inst. im. P. K. Shternberga **63**, 3 (1991).
14. V. Straižys and A. Kazlauskas, Balt. Astron. **2**, 1 (1993).
15. A. V. Kharitonov, M. M. Tereshchenko, and L. N. Knyazeva, *Spectrophotometric Star Catalogue* (Nauka, Alma-Ata, 1988).
16. K. Kodaĭra, in *Problems in Stellar Atmospheres and Envelopes*, Ed. by Baschek *et al.* (1975), p. 155.
17. V. Straižhis and K. Zdanavichus, Byull. Vil'n. Obs. **29**, 15 (1970).
18. D. S. Hayes, in *IAU Symp. 111: Calibration of Fundamental Stellar Quantities*, Ed. by D. S. Hayes *et al.* (Reidel, Dordrecht, 1985), p. 225.
19. H. Neckel and D. Labs, Solar Phys. **90**, 245 (1984).
20. J. C. Arvesen, R. N. Griffin, and B. D. Pearson, Appl. Opt. **8**, 2215 (1969).
21. G. M. Lockwood, H. Tug, and N. M. White, Astrophys. J. **390**, 668 (1992).
22. K. A. Burlov-Vasilijev, E. A. Gurtovenko, and Yu. B. Matvejev, in *Proc. Workshop on Solar Electromagnetic Radiation Study for Solar Cycle*, Ed. by R. F. Donnelly (NOOAA ERL, 1992), p. 49.
23. H. Tug, N. M. White, and G. M. Lockwood, Astron. Astrophys. **61**, 679 (1977).
24. L. N. Knyazeva and A. V. Kharitonov, Izv. Ross. Akad. Nauk, Ser. Fiz. **59**, 176 (1995).
25. E. A. Makarova, A. V. Kharitonov, and T. V. Kazachevskaya, *The Solar Radiation Flux* (Nauka, Moscow, 1991).
26. L. N. Knyazeva and A. V. Kharitonov, in *Proc. Second Annual Lowell Fall Workshop* (Flagstaff, Arizona, 1998), p. 113.
27. L. N. Knyazeva and A. V. Kharitonov, Astron. Zh. **71**, 458 (1994).

Translated by G. Rudnitskiĭ

Astronomy Reports, Vol. 44, No. 5, 2000, pp. 338–347. Translated from Astronomicheskiĭ Zhurnal, Vol. 77, No. 5, 2000, pp. 390–400.

Photodissociative Absorption by H_2^+ in the Solar Photosphere

V. S. Lebedev, L. P. Presnyakov, and I. I. Sobel'man

Lebedev Physical Institute, Russian Academy of Sciences,
Leninskiĭ pr. 53, Moscow, 117924 Russia

Received April 30, 1999

Abstract—Photoabsorption by systems of hydrogen atoms and protons in the solar photosphere is studied. Analytical formulas for the partial cross sections for photodissociation of the H_2^+ molecular ion are derived for the cases of fixed vibrational–rotational energy levels and averaging over a Boltzmann distribution for a given temperature. The photoabsorption coefficients for bound–free and free–free transitions of H–H$^+$ in the solar photosphere are calculated. These are compared with the absorption coefficients for photo-ejection of an electron from a negative hydrogen ion H$^-$ and free–free transitions of an electron in the field of a hydrogen atom H. Results can be applied to the Sun and hotter stars. © *2000 MAIK "Nauka/Interperiodica".*

1. INTRODUCTION

The largest contribution to the Sun's radiation is made by the negative hydrogen ion H$^-$, whose density in the photosphere is of the order of 10^{-8} of the density of neutral hydrogen atoms H [1]. Computations of the spectrum and total intensity of the solar emission usually assume that the optical depth of the photosphere at visual and near-infrared wavelengths is determined by photoabsorption via bound–free transitions, with the ejection of an electron from an H$^-$ ion,

$$H^-(1s^2\ {}^1S) + \hbar\omega \longrightarrow H(1s) + e \qquad (1)$$

and via free–free transitions

$$H(1s) + e + \hbar\omega \longrightarrow H(1s) + e. \qquad (2)$$

The effective cross sections for the photoabsorption processes (1) and (2) have been calculated in a number of studies. The calculations in [2, 3] are probably the most trustworthy. The accuracy of the results of [2] should be at least 1%. The cross section for photoabsorption by an H$^-$ ion (1) is of the order of 10^{-17} cm^2 in the energy range $1 < \hbar\omega < 5$ eV and reaches a maximum of $\sigma_{max} \approx 4 \times 10^{-17}$ cm^2 when the photon energy is 1.4 eV.

In connection with the accurate calculations [2, 3], it is interesting to analyze in detail the role of other possible photoabsorption processes. The contribution of such processes to the optical depth of the photosphere at visual and near-infrared wavelengths could be as large as 1–10% of the contribution from (1) and (2). One such process is absorption by the H_2^+ molecular ion during its photodissociation:

$$H_2^+({}^2\Sigma_g^+) + \hbar\omega \longrightarrow H_2^+({}^2\Sigma_u^+) \longrightarrow H(1s) + H^+ \qquad (3)$$

with the formation of a proton and a neutral hydrogen atom. A photon is absorbed as a result of an electron transition between the even (bound) ${}^2\Sigma_g^+$ and odd (repulsive) ${}^2\Sigma_u^+$ terms of the H_2^+ ion, which are split by the exchange interaction between the hydrogen atom and proton (see figure). We emphasize that precisely H_2^+ is of interest here, although the concentration of H_2 molecules is a factor of ~10^4–10^5 higher. The ground term ${}^1\Sigma_g^+$ and first excited (repulsive) term ${}^3\Sigma_u^+$ for these molecules have different multiplicities. Therefore, the intercombination transition between them is strongly suppressed, since a spin must be exchanged.

Process (3), which describes photoabsorption via bound–free transitions of the H–H$^+$ system, must be supplemented by free–free transitions of the same system:

$$\begin{aligned} H(1s) + H^+ + \hbar\omega &\longrightarrow (H + H^+)_{^2\Sigma_g^+} + \hbar\omega \\ &\longrightarrow (H + H^+)_{^2\Sigma_u^+} \longrightarrow H(1s) + H^+. \end{aligned} \qquad (4)$$

As for photodissociation (3), the process (4)—absorption of a photon during a collision between H and H$^+$ particles—takes place as a result of a ${}^2\Sigma_g^+ \longrightarrow {}^2\Sigma_u^+$ transition, during which there is a change in the symmetry of the electron wave function.

The possible role of bound–free and free–free transitions (3) and (4) in the H–H$^+$ system in some stellar atmospheres was first noted in [4]. H_2^+ is the simplest diatomic molecule and has been the subject of many theoretical studies. Perhaps the largest contribution to the theory of the H_2^+ ion and ${}^2\Sigma_g^+ \longrightarrow {}^2\Sigma_u^+$ radiative transitions has been made by Bates and his coworkers ([5] and references therein). These studies were concerned with calculations of energy-level splitting for

the H_2^+ system and of oscillator strengths for $^2\Sigma_g^+ \longrightarrow {}^2\Sigma_u^+$ radiative electron transitions, which were later also calculated in [6].

The first quantitative treatment of processes (3) and (4) was performed by Bates in [7], where he calculated the integrated absorption coefficient $K_T(\omega)$ for a wide range of transition frequencies ω and temperatures T = 2500–12000 K. He derived a simple analytic formula for $K_T(\omega)$ [7], based on quantum calculations of the oscillator strengths assuming a fixed internuclear distance R and treating the H and H^+ nuclei as classical particles, with the coordinates R distributed according to the probability $W_T(R) \propto 4\pi R^2 \exp[-U(R)/kT]$ in the bound $U_g(R)$ and repulsive $U_u(R)$ terms. By using a model with fixed H and H^+ centers and a classical distribution function for the internuclear distance R in a diatomic system with a given interaction potential $U(R)$ (see, for example, [8], p. 167), Bates completely avoided calculating the photodissociative absorption cross sections for particular vibrational–rotational states vK and summing over these states.

Later, the influence of the quantum character of the nuclear motions during the photodissociation (3) of H_2^+ ions was studied in [9] for short wavelengths ($2.7 < \hbar\omega < 14.3$ eV) and relatively low temperatures (T = 1000 and 2500 K), and the results for the absorption coefficients were compared with the data of [7]. Further, the calculations of [7] were used to compile tables and derive approximation formulas for bound–free and free–free transitions $^2\Sigma_g^+ \longrightarrow {}^2\Sigma_u^+$ in the H_2^+ ion [10].

Quantum-mechanical calculations of cross sections for photodissociation (3) from fixed vibrational levels v were conducted in [11, 12] for the case of small rotational quantum numbers K = 0 and 1. The data of Bates cited above were used for the electron matrix elements of the $^2\Sigma_g^+ \longrightarrow {}^2\Sigma_u^+$ transition. In [12], the resulting cross sections were summed over v using a Franck–Condon distribution, which is characteristic of the formation of H_2^+ ions during the photoionization of neutral hydrogen molecules H_2 or the ionization of H_2 by electron bombardment (the temperature of the H_2 molecules was assumed to be low, equal to room temperature). The conditions assumed in calculations such as those of [11, 12] are obviously far from those in the solar photosphere.

The aim of the present paper is to analyze absorption by molecular (quasi-molecular) H_2^+ ions at visual, near-infrared, and near-ultraviolet wavelengths at fairly high temperatures (T = 4500–10000 K). Under these conditions, a large number of vibrational and rotational levels of the ground electron state $^2\Sigma_g^+$ are simultaneously excited. We adopted a self-consistent approach to calculate the cross sections of the radiative processes (3) and (4) together with the integrated photoabsorption coefficient, taking into account a realistic Boltzmann distribution over the vibrational–rotational levels and the contribution of the continuum of the H–H^+ system. We also transform our results to simple analytic expressions corresponding to the semiclassical limit of Bates [7]. Special attention is paid to comparing the roles of these processes and of photoabsorption by bound–free (1) and free–free (2) transitions in the H–e system (i.e., the H^- ion) in the photospheres of the Sun and hotter stars.

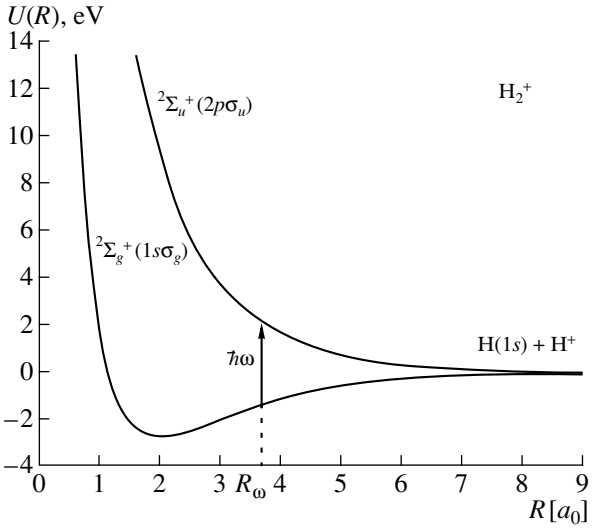

A diagram of light absorption via photodissociation of the H_2^+ molecular ion during an electron transition between its ground (even) $^2\Sigma_g^+$ and first excited (odd) $^2\Sigma_u^+$ terms.

2. PHOTODISSOCIATION OF THE H_2^+ ION AND FREE–FREE TRANSITIONS IN THE H–H^+ SYSTEM

2.1. Equilibrium Density of H_2^+ *Ions*

The number density of H_2^+ in the solar photosphere is of the same order of magnitude as that of H^- ions. The law of mass action specifying the equilibrium conditions (see [8]) leads to the relations

$$\frac{N_{H_2^+}}{N_H N_{H^+}} = \frac{g_{H_2^+}}{g_H g_{H^+}}\left(\frac{2\pi\hbar^2}{\mu kT}\right)^{3/2} Z^{(g)}_{v-r}\exp\left(\frac{D_0}{kT}\right) \approx \frac{8I}{\Omega_e}\left(\frac{\pi}{M_p}\right)^{3/2}\sqrt{kT}\exp\left(\frac{D_0}{kT}\right), \quad (5)$$

$$\frac{N_{H^-}}{N_H N_e} = \frac{g_{H^-}}{g_H g_e}\left(\frac{2\pi\hbar^2}{m_e kT}\right)^{3/2}\exp\left(\frac{|E_{H^-}|}{kT}\right), \quad (6)$$

$$g_{H_2^+} = 2, \quad g_{H^-} = 1, \quad g_H = 2,$$
$$g_e = 2, \quad g_{H^+} = 1. \tag{7}$$

Here, $g_{H_2^+}$ and g_{H^-} are the statistical weights of the electron states for the $H_2^+ (^2\Sigma_g^+)$ and $H^-(1s^2\ ^1S)$ ions; g_H is the statistical weight of a hydrogen atom in its 1*s* ground state; m_e, N_e, g_e and M_p, N_{H^+}, g_{H^+} are the masses, number densities, and statistical weights of the electrons and protons H^+, respectively; $|E_{H^-}| = 0.754$ eV is the binding energy of the electron in an H^- ion; $D_0 = 2.65$ eV is the energy of dissociation of an H_2^+ ion from the ground vibrational–rotational state $v = 0$, $K = 0$ ($\mu = M_p/2$ is its reduced mass); $I = \mu R_e^2$ is the moment of inertia; $R_e = 2.0a_0$ is the equilibrium internuclear distance ($a_0 = 0.529 \times 10^{-8}$ cm is the Bohr radius); and $\Omega_e = 4.37 \times 10^{14}$ s^{-1} is the oscillation frequency for the lowest level $v = 0$, $K = 0$ (see [13]). Expression (5) contains the vibrational–rotational statistical sum for the even ground term $^2\Sigma_g^+(1s\sigma_g)$ of H_2^+, which is equal to

$$Z_{v-r}^{(g)} = \frac{1}{2} Z_{v-r}$$
$$= \frac{1}{2}\sum_{vK}(2K+1)\exp\left(-\frac{\epsilon_{vK}}{kT}\right) \approx \frac{(kT)^2}{2B_e\hbar\Omega_e}, \tag{8}$$

where Z_{v-r} is the vibrational–rotational statistical sum for a diatomic molecule with arbitrary nuclei (which can, in general, be different from each other, as distinct from the H_2^+ ion), ϵ_{vK} is the energy of the vibrational–rotational level vK measured from the zero level $v = 0$, $K = 0$ (so that $\epsilon_{vK} > 0$), and $B_e = \hbar^2/2I$ is the rotational constant in energy units. Relation (8) specifies the quantity Z_{v-r} in the temperature range $\hbar\Omega_e/3 \ll kT \ll D_0$ (see [8], pp. 157–167). The equilibrium values of the relative number densities $N_{H_2^+}/N_H N_{H^+}$ and $N_{H^-}/N_H N_e$ calculated using (5) and (6) and the ratio $N_{H_2^+}/N_{H^-}$ are presented in Table 1. We took the number densities of the electrons N_e and protons N_{H^+} to be equal. The number densities N are expressed in cm^{-3}.

Table 1. Dependence of relative number densities of H_2^+ and H^- on temperature ($T = 4500$–10000 K)

T [K]	$N_{H_2^+}/N_H N_{H^+}$, 10^{-21}cm^3	$N_{H^-}/N_H N_e$, 10^{-21} cm^3	$N_{H_2^+}/N_{H^-}$
4500	3.20	2.34	1.37
5000	1.70	1.68	1.01
5500	1.02	1.24	0.82
5800	0.79	1.06	0.74
6000	0.67	0.96	0.70
6500	0.47	0.76	0.62
8000	0.21	0.43	0.50
10000	0.11	0.25	0.45

2.2. Cross-Section for Photodissociation from an Excited Vibrational–Rotational State

The figure shows potential-energy curves for the ground $^2\Sigma_g^+(1s\sigma_g)$ and first excited (repulsive) $^2\Sigma_u^+(2p\sigma_u)$ electron terms of H_2^+. In the case of large internuclear distances $R \longrightarrow \infty$, these terms are correlated with the $H(1s) + H^+$ state of the isolated hydrogen atom and proton; i.e., they tend to the same dissociation limit—the electron energy of the 1*s* level of the hydrogen atom. The minimum $U_g(R_e) = -D_e = -2.79$ eV in the potential energy curve $U_g(R)$ of the $^2\Sigma_g^+$ state corresponds to the internuclear distance $R_e = 2.0a_0$. The corresponding electron-term splitting energy is $\Delta U_{ug}(R_e) = 11.84$ eV.

Therefore, $^2\Sigma_g^+, v, K \longrightarrow {}^2\Sigma_u^+, E, K \pm 1$ phototransitions from low vibrational–rotational levels vK ($v = 0$, 1, 2) near the bottom of the potential well $R_\omega \approx 1.6$–$2.6\ a_0$ of the $U_g(R)$ term correspond to very large energies ($\hbar\omega \approx 8$–16 eV) and small wavelengths ($\lambda \approx 800$–1600 Å). In the visual (and the adjacent near-ultraviolet and near-infrared, with photon energies $0.25 < \hbar\omega < 6$ eV; i.e., $0.2 < \lambda < 5$ μm), the process (3) of photodissociative absorption by H_2^+ is primarily realized from excited levels vK. Phototransitions at these wavelengths take place in the attraction region ($R_\omega > R_e$) of the potential-energy curve $U_g(R)$ of the lowest electron state at internuclear distances $3 < R_\omega < 7\ a_0$. Table 2 presents the potential energies $U_g(R)$ in the $1s\sigma_g$ ground state, the splitting energies $\Delta U_{ug}(R)$ for even (g) and odd (u) terms, and the oscillator strengths $f_{ug}(R)$ of the $1s\sigma_g \longrightarrow 2p\sigma_u$ electron transition as functions of R for the above range of distances, $R \geq 3a_0$.

The cross section for photodissociation from a given vibrational–rotational energy level vK of the ground electron term $^2\Sigma_g^+$ to the continuum of the repulsive term $^2\Sigma_u^+$ with energy $E = \hbar^2 q^2/2\mu$ is determined by the expression [14, 15]

$$\sigma_{vK}^{ph.d}(\omega) = \frac{4\pi^2\omega}{3c}\sum_{K'=K\pm1}\frac{\max(K', K)}{(2K+1)}\left|d_{EK', vK}^{(u,g)}\right|^2, \tag{9}$$
$$E = \hbar\omega - |E_{vK}|.$$

Here, c is the speed of light, $|E_{vK}|$ is the bonding energy of the $H_2^+ (^2\Sigma_g^+)$ molecular ion at the level vK, and q is the wave number of H and H^+ particles separated by $R \longrightarrow \infty$. We will measure the potential energies $U_g(R)$ and $U_u(R)$ from the ion dissociation edge; i.e., $U_g(\infty) = U_u(\infty) = 0$ and $E_{vK} < 0$, whereas $E > 0$ (the vibrational–rotational energy E_{vK} of level vK is related to the energy $\epsilon_{vK} > 0$ in (8), measured from the level $v = 0$, $K = 0$, by the expression $|E_{vK}| = D_0 - \epsilon_{vK}$).

The matrix element $d^{(u,g)}_{EK',vK}$ of the dipole moment of the $^2\Sigma_g^+$, $v, K \longrightarrow {}^2\Sigma_u^+$, E, K' transition in the radial wave functions $\chi(R)$ for the relative motion of the H and H^+ in the discrete spectrum of the initial bound electron state $^2\Sigma_g^+$ of the H_2^+ ion and the continuum of the final repulsive state $^2\Sigma_u^+$ takes the form:

$$d^{(u,g)}_{EK',vK} = \left\langle \chi^{(u)}_{EK'}(R)|d_{ug}(R)|\chi^{(g)}_{vK}(R)\right\rangle = \int_0^\infty (\chi^{(u)}_{EK'}(R))^* d_{ug}(R)\chi^{(g)}_{vK}(R)R^2dR. \quad (10)$$

Here, $d_{ug}(R)$ is the electron matrix element for the transition between the $^2\Sigma_g^+ \longrightarrow {}^2\Sigma_u^+$ terms:

$$\mathbf{d}_{ug}(\mathbf{R}) = \langle \phi_u(\mathbf{r}, \mathbf{R})|e\mathbf{r}|\phi_g(\mathbf{r}, \mathbf{R})\rangle = \int \phi_u^*(\mathbf{r}, \mathbf{R})(e\mathbf{r})\phi_g(\mathbf{r}, \mathbf{R})d\mathbf{r} \quad (11)$$

in the adiabatic wave functions $\phi_g(\mathbf{r}, \mathbf{R})$ and $\phi_u(\mathbf{r}, \mathbf{R})$ for the electron in the axially symmetric two-proton field, H^+ and H^+, where $\mathbf{d}_{ug} \parallel \mathbf{R}$ (see [5] and [16], pp. 362–364) and $\mathbf{r}$ is the electron radius vector measured from the center of mass of the H_2^+ ion.

The electron-transition dipole matrix element (11) is related to the corresponding oscillator strength $f_{ug}(R_\omega)$ of the transition at frequency $\omega = \Delta U_{ug}(R_\omega)/\hbar$ by the expression

$$f_{ug}(R_\omega) = \frac{2}{3}\frac{m_e\omega}{\hbar e^2}|d_{ug}(R_\omega)|^2. \quad (12)$$

The nuclear wave functions in (10) are normalized as follows:

$$\int_0^\infty \left|\chi^{(g)}_{vK}(R)\right|^2 R^2dR = 1, \qquad \int_0^\infty (\chi^{(u)}_{E'K}(R))^*\chi^{(u)}_{EK}(R)R^2dR = \delta(E - E'). \quad (13)$$

When calculating the partial photodissociation cross section (9) for the case of high vibrational–rotational levels vK, we should bear in mind that the main contribution to the integral over internuclear distance (10) for a given transition frequency ω is made by a small neighborhood of the point R_ω where the $H_2^+ (^2\Sigma_g^+) + \hbar\omega$ and $H_2^+ (^2\Sigma_u^+)$ potential-energy curves intersect; i.e.,

$$U_g(R_\omega) + \hbar\omega = U_u(R_\omega), \qquad \Delta U_{ug}(R_\omega) = U_u(R_\omega) - U_g(R_\omega) = \hbar\omega. \quad (14)$$

Therefore, we can calculate the radial matrix element of the dipole moment (10) using the quasi-classical method of Landau ([16], pp. 399–401) or using an approach based on a quantum solution for the nonadiabatic transitions in a model with linearly intersecting terms. This type of approach enables us to correctly account for the contribution to the photodissociative absorption coefficient $k^{\text{ph.d}}_{H_2^+}(\omega)$, summed over all vK, of all excited vibrational–rotational levels of the potential-energy curves (14) whose classical turning points $R = a_{vK}$ are both far from and near the intersection point R_ω.

Exact solutions for the one-dimensional motion of nuclei in a uniform field (which, apart from normalization coefficients, reduce to Airy functions $\mathbf{\Phi}(x)$; see

Table 2. Splitting of terms $\Delta U_{ug}(R)$, potential energy $U_g(R)$ of the lowest state $^2\Sigma_g^+$ of the H_2^+ ion (measured from the dissociation edge $U_g(\infty) = U_u(\infty) = 0$), and oscillator strengths $f_{ug}(R)$ of the $^2\Sigma_g^+ \longrightarrow {}^2\Sigma_u^+$ electron transition according to [5, 6]

R [a_0]	U_g, eV	ΔU_{ug}, eV	$f_{ug}(R)$
3.0	−2.110	5.701	0.289
3.2	−1.925	4.925	0.281
3.4	−1.744	4.256	0.271
3.6	−1.570	3.676	0.261
3.8	−1.407	3.173	0.250
4.0	−1.254	2.736	0.238
4.2	−1.113	2.356	0.226
4.4	−0.984	2.027	0.213
4.6	−0.866	1.744	0.201
4.8	−0.760	1.497	0.188
5.0	−0.664	1.282	0.175
5.5	−0.469	0.865	0.144
6.0	−0.326	0.580	0.116
6.5	−0.226	0.385	0.090
7.0	−0.152	0.253	0.070
7.5	−0.103	0.166	0.052
8.0	−0.070	0.109	0039
8.5	−0.047	0.070	0.028
9.0	−0.033	0.046	0.021

[16], Para 24) should be taken for the nuclear wave functions of the discrete $\chi_{vK}^{(g)}(R)$ and continuum $\chi_{EK}^{(u)}(R)$. Thus, instead of the widely used quasi-classical formula (see [16], p. 401) for the transition probability at the point R_ω, we use a more general method to calculate the nonadiabatic transitions between two different electron terms (this method is similar to that in Exercise 3 of Para 90 [16] in connection with collisions of the second kind). Applying this approach to radiative transitions between the electron terms of the H_2^+ ion leads to the following expression for the cross section for photodissociation from a given vibrational–rotational level vK:

$$\sigma_{vK}^{\text{ph.d}}(\omega) = \frac{8\pi^2\omega}{3cT_{vK}}\frac{|d_{ug}(R_\omega)|^2}{\Delta F_{ug}(R_\omega)} \times \frac{A_{vK}}{\sqrt{(2/\mu)[E_{vK} - U_g(R_\omega) - \hbar^2(K+1/2)^2/2\mu R_\omega^2]}}. \quad (15)$$

Here, $T_{vK} = 2\pi\hbar/|E_{vK} - E_{v\pm1,K}|$ is the period of the vibrational–rotational motion of the nuclei in the state vK, and $\Delta F_{ug}(R_\omega)$ is the difference between the slopes of the potential-energy curves $U_g(R)$ and $U_u(R)$ at their point of intersection R_ω:

$$\Delta F_{ug}(R_\omega) = \Delta F_{ug}^{(K)}(R_\omega) = \left|\frac{dU_u(R)}{dR} - \frac{dU_g(R)}{dR}\right|_{R=R_\omega}. \quad (16)$$

The quantity A_{vK} in (15) can be expressed in terms of the square of an Airy function

$$A_{vK} = 2|\xi|^{1/2}\mathbf{\Phi}^2(-\xi), \qquad \mathbf{\Phi}(x) = \frac{1}{\sqrt{\pi}}\int_0^\infty \cos\left(\frac{u^3}{3} + ux\right)dx, \quad (17)$$

where

$$\xi = \left(\frac{2\mu}{\hbar^2}\right)^{1/3}\left(E_{vK} - U_g(R_\omega) - \frac{\hbar^2(K+1/2)^2}{2\mu R_\omega^2}\right) \times \left|\frac{\Delta F_{ug}(R_\omega)}{F_u^{(K)}(R_\omega)F_g^{(K)}(R_\omega)}\right|^{2/3}, \quad (18)$$

and $F_g^{(K)}(R_\omega)$ and $F_u^{(K)}(R_\omega)$ are the slopes of the even and odd terms taking into account the centrifugal energy:

$$F_g^{(K)}(R_\omega) = -\frac{d}{dR}\left(U_g + \frac{\hbar^2(K+1/2)^2}{2\mu R_\omega^2}\right)\Bigg|_{R=R_\omega}, \quad (19)$$

$$F_u^{(K)}(R_\omega) = -\frac{d}{dR}\left(U_u + \frac{\hbar^2(K+1/2)^2}{2\mu R_\omega^2}\right)\Bigg|_{R=R_\omega}. \quad (20)$$

In accordance with [16], we use the definition of the Airy function $\mathbf{\Phi}(x)$ introduced by Fock (which differs from that presented in some handbooks by a factor of $\pi^{1/2}$). Note that, throughout the paper, we give only a qualitative physical basis for the approximations used and the final formulas and will publish detailed calculations in a separate article.

Further, we use the well-known asymptotic of the Airy function $\mathbf{\Phi}(x)$ in the classically permitted region of motion for the H and H^+ nuclei ($\xi > 0$), average the result (15) over the period of the rapidly oscillating part of the function $\mathbf{\Phi}^2(-\xi)$ in this region, and neglect its exponentially small decrease in the classically forbidden region ($\xi < 0$). Then, we can see from (17) and (18) that $A_{vK} \longrightarrow 1$ far from the inflection point (i.e., for sufficiently large values of the energy difference $E_{vK} - U_g(R_\omega) - \hbar^2(K+1/2)^2/2\mu R_\omega^2$). In this case, a simple, quasi-classical expression for the cross section for photodissociation of H_2^+ ($^2\Sigma_g^+$) from a fixed vibrational–rotational level vK follows immediately from the quantum formula (15). Note that this asymptotic of (15), which corresponds to $A_{vK} = 1$, can also be derived directly from the initial expression (9), if the results of Landau's [16, pp. 399–401] quasi-classical theory are used to calculate the dipole matrix element for transitions in the H–H^+ system at the intersection point of the potential-energy curves.

We can see from (15)–(18) that the quantum calculation of the partial photodissociation cross section differs from the quasi-classical calculation only at small values for the difference $[E_{vK} - U_g(R_\omega) - \hbar^2(K+1/2)^2/2\mu R_\omega^2]$. In particular, taking account of the factor A_{vK} in (15) leads to a finite value for the cross section at $E_{vK} - U_g(R_\omega) - \hbar^2(K+1/2)^2/2\mu R_\omega^2 = 0$ and describes its rapid decrease in the classically forbidden region for nuclear motion.

2.3. Averaging over the Boltzmann Distribution and the Photodissociative Absorption Coefficient

A large number of vibrational–rotational levels vK are excited simultaneously at temperatures $kT > \hbar\Omega_e \gg B_e$ ($\hbar\Omega_e = 0.288$ eV, $B_e = 3.74 \times 10^{-3}$ eV [13]), present in the solar photosphere ($kT \sim 0.5$ eV). In this situation, if we wish to find the photodissociative absorption coefficient $k_{H_2^+}^{\text{ph.d}}(\omega)$

$$k_{H_2^+}^{\text{ph.d}}(\omega) = \sigma_T^{\text{ph.d}}(\omega)N_{H_2^+}, \quad (21)$$

it is of the most interest to calculate the cross section $\sigma_{H_2^+}^{\text{ph.d}}(\omega)$ averaged over v and K and normalized to the

total number density of H_2^+ in the photosphere at temperature T:

$$\sigma_T^{\text{ph.d}}(\omega) = \sum_{vK} \sigma_{vK}^{\text{ph.d}}(\omega) \frac{N_{H_2^+}^{(vK)}}{N_{H_2^+}} = \sum_{vK} \sigma_{vK}^{\text{ph.d}}(\omega) \frac{(2K+1)}{Z_{v-r}} \exp\left(-\frac{E_{vK}+D_0}{kT}\right), \quad (22)$$

where the statistical sum Z_{v-r} is determined from formula (8).

When calculating the photodissociation cross section $\sigma_T^{\text{ph.d}}(\omega)$ averaged over a Boltzmann distribution, the summation over the vibrational–rotational levels vK in (22) can be replaced by integration over dv and dK, and carried out using a method similar to that of [17] This corresponds to replacing the discrete spectrum of the vibrational–rotational energy levels with a quasi-continuum.

Further, numerical computations demonstrate that, at temperatures T = 4500–10000 K and for all transition frequencies ω in the range $0.25 < \hbar\omega < 5.7$ eV under consideration, the energy interval E_{vK} where the classical inflection points $R = a_{vK}$ are near the intersection point R_ω of the potential-energy curves (14) (i.e., where the factor $[E_{vK} - U_g(R_\omega) - \hbar^2(K+1/2)^2/2\mu R_\omega^2]$ in (15) is close to zero) does not make an important contribution to the integral over dv and dK. This enables us to restrict our treatment to a quasi-classical approximation when calculating the averaged cross section $\sigma_T^{\text{ph.d}}(\omega)$ [cm^2] and the corresponding absorption coefficient $k_{H_2^+}^{\text{ph.d}}(\omega)$ [cm^{-1}]; in other words, we can use the value $A_{vK} = 1$ in (15) and (17) in the classically permitted region and neglect the exponentially small decrease of the partial cross section $\sigma_{vK}^{\text{ph.d}}(\omega)$ in the classically forbidden region. The integration over the rotational quantum numbers in (22) is conducted over the range $0 \le K \le K_{\max}$ (where $\hbar^2 K_{\max}^2/2\mu R_\omega^2 = E_{vK} - U_g(R_\omega)$); the integration over the energy of the H_2^+ ion in the discrete spectrum is conducted over the range $E_{\min} \le E \le 0$ (where $E_{\min} = U_g(R_\omega) < 0$).

The calculation result obtained using the above approximations can be written

$$\sigma_T^{\text{ph.d}}(\omega) = \frac{16\pi^3}{3c} \frac{\omega R_\omega^2 |d_{ug}(R_\omega)|^2}{\Delta F_{ug}(R_\omega) Z_{v-r}} \left(\frac{\mu kT}{2\pi\hbar^2}\right)^{3/2} \times \exp\left(-\frac{D_0 + U_g(R_\omega)}{kT}\right) \frac{\gamma(3/2, |U_g(R_\omega)|/kT)}{\Gamma(3/2)}. \quad (23)$$

Here, $\gamma(3/2, z)$ is an incomplete gamma function of order 3/2 (see, for example, [18]):

$$\gamma(3/2, z) = \int_0^z t^{1/2} e^{-t} dt, \quad \Gamma(3/2) = \sqrt{\pi}/2. \quad (24)$$

The average cross section $\sigma_T^{\text{ph.d}}(\omega)$ determined by formula (23) is a function of the frequency ω and gas temperature T and enables us, using (21), to calculate the photodissociative absorption coefficient for a given value of the total number density of H_2^+ in the discrete spectrum. During specific calculations, it is convenient to express the total number density of H_2^+ in the bound state $^2\Sigma_g^+$ in terms of the number densities of neutral hydrogen atoms H(1s) and protons H^+ in the continuum using relation (5). Then, with relation (12) for the electron-transition oscillator strengths, the corresponding result for the absorption coefficient $k_{H_2^+}^{\text{ph.d}}(\omega)$ [cm^{-1}] (21) for photodissociation (3) takes the form

$$k_{H_2^+}^{\text{ph.d}}(\omega) = 4\pi^3 \alpha \left(\frac{\hbar^2}{m_e}\right) \frac{R_\omega^2 f_{ug}(R_\omega)}{\Delta F_{ug}(R_\omega)} \times \exp\left(-\frac{U_g(R_\omega)}{kT}\right) \frac{\gamma(3/2, |U_g(R_\omega)|/kT)}{\Gamma(3/2)} N_H N_{H^+}, \quad (25)$$

where $\alpha = e^2/\hbar c = 1/137$ is the fine-structure constant.

2.4. Contribution of the Continuous Spectrum and the Resulting Photoabsorption Coefficient

Let us consider now the contribution of (4) to photoabsorption resulting from free–free transitions of the H–H^+ system. The initial quantum expression for the absorption coefficient for collisions of H(1s) and H^+ particles during transitions from a continuum state with energy E for the initial term $U_g(R)$ to a continuum state with final repulsive term $U_u(R)$ with energy $E' = E + \hbar\omega$ takes the form [14, 15]

$$k_{H^+-H}^{\text{fr–fr}}(\omega) = \langle V \sigma_{E',E}^{(u,g)} \rangle_T \text{ [cm}^{-1}\text{]}, \quad E = \frac{\hbar^2 q^2}{2\mu}, \quad E' = \frac{\hbar^2 (q')^2}{2\mu}, \quad (26)$$

$$\sigma_{E',E}^{(u,g)}(\omega) = \left\{\frac{1}{2}\frac{g_{H_2^+}}{g_H g_{H^+}}\right\} \frac{8\pi^4\hbar\omega}{3cq^2} \times \sum_K [(K+1)|d_{E',K+1;EK}^{(u,g)}|^2 + K|d_{E',K-1;EK}^{(u,g)}|^2]. \quad (27)$$

Here, $\sigma_{E',E}^{(u,g)}$ [cm^4 s] is the effective cross section for the photoabsorption process (4), $V = (2E/\mu)^{1/2}$ is the relative velocity of the colliding H(1*s*) and H$^+$ particles at $R \longrightarrow \infty$, and K is the orbital quantum number of these particles (in the quasi-classical limit, $K = q\rho$, where ρ is the impact parameter). The averaging in (27) is carried out over a Maxwell distribution for the velocities V. The matrix element of the dipole moment of the free–free transition differs from (10) only in the exchange of the initial nuclear wave function of the discrete spectrum $\chi_{vK}^{(g)}(R)$ with the corresponding wave function of the continuum $\chi_{EK}^{(g)}(R)$, normalized to an energy δ function.

The factor of one-half in the braces in (27) is due to the symmetry of process (4) with respect to permutation of the H and H$^+$ nuclei, similar to the factor of one-half in the statistical sum (8) for the discrete spectrum. Collisions of the H and H$^+$ can occur with equal probabilities via the two channels

$$\mathrm{H} + \mathrm{H}^+ \longrightarrow \begin{cases} (\mathrm{H} + \mathrm{H}^+)_{^2\Sigma_g^+} \\ (\mathrm{H} + \mathrm{H}^+)_{^2\Sigma_u^+}. \end{cases} \tag{28}$$

We can calculate the absorption coefficient (26) for free–free transitions (4) using the same approximation as for (23) and (25). The result is

$$k_{\mathrm{H}^+-\mathrm{H}}^{\mathrm{fr-fr}}(\omega) = 4\pi^3\alpha\left(\frac{\hbar^2}{m_e}\right)\frac{R_\omega^2 f_{ug}(R_\omega)}{\Delta F_{ug}(R_\omega)} \times \exp\left(-\frac{U_g(R_\omega)}{kT}\right)\frac{\Gamma(3/2, |U_g(R_\omega)|/kT)}{\Gamma(3/2)} N_{\mathrm{H}} N_{\mathrm{H}^+}, \tag{29}$$

$$\Gamma(3/2, z) = \int_z^\infty t^{1/2} e^{-t} dt = \Gamma(3/2) - \gamma(3/2, z). \tag{30}$$

As in the case of photodissociation, the total contribution of the continuum to the absorption coefficient is described by a simple formula in the quasi-classical approximation. Comparison of expressions (25) and (29) for the absorption coefficients for bound–free (3) and free–free (4) transitions shows that, in the quasi-classical approximation, they differ only in the factors of $\gamma(3/2, z)$ and $\Gamma(3/2, z)$ corresponding to the contributions of the discrete and continuous spectra of the H_2^+ ion (where $z = |U_g(R_\omega)|/kT$). In particular, both contributions are proportional to the product $N_{\mathrm{H}} N_{\mathrm{H}^+}$ of the number densities of hydrogen atoms H(1*s*) and protons H$^+$ in the continuum. This enables us to derive a more compact analytical expression for the total absorption coefficient for processes (3) and (4). In a quasi-continuum approximation, the general formula takes the form

$$k_T(\omega) = k_{H_2^+}^{\mathrm{ph.d}}(\omega) + k_{\mathrm{H}^+-\mathrm{H}}^{\mathrm{fr-fr}}(\omega) = 4\pi^3\alpha\left(\frac{\hbar^2}{m_e}\right)\frac{R_\omega^2 f_{ug}(R_\omega)}{\Delta F_{ug}(R_\omega)} \exp\left(-\frac{U_g(R_\omega)}{kT}\right) N_{\mathrm{H}} N_{\mathrm{H}^+}. \tag{31}$$

This result has a clear physical interpretation: The absorption coefficient is proportional to the oscillator strength $f_{ug}(R_\omega)$ of the $^2\Sigma_g^+ \longrightarrow {}^2\Sigma_u^+$ electron transition at the intersection of the terms (14). It is also proportional to the probability $W_T(R_\omega) \propto 4\pi R_\omega^2 \exp[-U_g(R_\omega)/kT]$ that the H(1*s*) and H$^+$ particles are separated by a distance R_ω in the initial bound state $U_g(R)$. The Boltzmann factor $\exp(-U_g/kT)$ in (31) specifies the temperature dependence of the total absorption coefficient.

Formula (31) represents the total contribution of the direct processes (3) and (4) to the H–H$^+$ system photoabsorption coefficient. Taking into account stimulated emission, the resulting absorption coefficient $K_T(\omega)$ under conditions of thermodynamic equilibrium is given by the well-known relation (see [14])

$$K_T(\omega) = k_T(\omega)\left[1 - \exp\left(-\frac{\hbar\omega}{kT}\right)\right]. \tag{32}$$

We are primarily interested in a comparative analysis of the roles of the photoabsorption processes (3), (4) and (1), (2) as functions of the frequency ω. The factor in square brackets in (32) affects the formulas for the absorption coefficients for the direct and inverse processes in the same way. Therefore, we present our results for the absorption coefficients below, without taking into account stimulated emission.

Combining (31) and (32) leads to the well-known result of Bates [7] for photoabsorption by the H–H$^+$ system, derived using a simple model with fixed Coulomb centers and a classical Boltzmann distribution function for their coordinates. Our treatment was based on the initial quantum formulas for the cross sections for photodissociation and free–free transitions. Our results show that, in a quasi-classical limit for the nuclear wave functions, the total contribution of these processes can be described by the simple analytic expression (31), if, in addition, we use a quasi-continuum approximation for the vibrational–rotational levels.

Our numerical computation was based on the more exact formula (15) for the partial photodissociation cross section and an analogous formula for the contribution of the continuum. The computation shows that the correction factor (17), allowing for the quantum character of the nuclear motion in the classically forbidden region near the turning points, affects the total absorption coefficients in the visual, near-infrared, and near-ultraviolet only slightly for the gas temperatures T = 4500–10000 K under consideration. This immedi-

Table 3. Dependence of $k_T(\omega)$, cm^{-1} on ω (or wavelength λ) for temperatures in the range $T = 4500$–10000 K. Values of $\eta_T(\omega) = k_T(\omega)/N_H H_{H^+}$ calculated using (31) are in units of 10^{-39} cm^5

$\hbar\omega$, eV	λ, μm	R_ω [a_0]	T, K							
			4500	5000	5500	5800	6000	6500	8000	10000
			$\eta_T(\omega)$, 10^{-39} cm^5							
5.701	0.217	3.0	16.09	9.33	5.98	4.76	4.13	3.02	1.49	0.807
4.925	0.252	3.2	12.40	7.55	5.03	4.08	3.59	2.69	1.41	0.809
4.256	0.291	3.4	9.54	6.08	4.21	3.48	3.10	2.39	1.33	0.805
3.676	0.337	3.6	7.44	4.96	3.56	3.01	2.71	2.14	1.27	0.803
3.173	0.391	3.8	5.93	4.12	3.06	2.63	2.39	1.94	1.21	0.806
2.736	0.453	4.0	4.80	3.47	2.67	2.33	2.14	1.78	1.17	0.811
2.356	0.526	4.2	3.97	2.98	2.36	2.09	1.94	1.64	1.13	0.820
2.027	0.612	4.4	3.39	2.63	2.14	1.92	1.80	1.55	1.12	0.840
1.744	0.711	4.6	2.95	2.36	1.96	1.79	1.69	1.48	1.11	0.863
1.497	0.828	4.8	2.64	2.17	1.85	1.70	1.62	1.45	1.12	0.898
1.282	0.967	5.0	2.41	2.03	1.78	1.64	1.57	1.42	1.14	0.940
0.580	2.137	6.0	2.04	1.88	1.75	1.69	1.66	1.58	1.41	1.29
0.253	4.900	7.0	2.38	2.29	2.22	2.18	2.16	2.11	2.01	1.92

ately suggests that the quasi-classical approximation can be applied to calculations of absorption coefficients in the photospheres of the Sun and hotter stars and confirms the validity of the semiclassical approach used by Bates.

Further development of the theory of absorption by a medium in equilibrium containing atomic and molecular components must go beyond the Born–Oppenheimer approximation, which assumes that the electron and nuclear motions are completely separate. This approximation is most justified for low vibrational–rotational states. As the quantum numbers v and K increase, the interdependence between the electron and nuclear motions ceases to be negligible and can lead to considerable additional effects. These effects have been studied in the physics of atomic collisions, where methods for taking into account electron–nuclear correlations were developed. Applying these methods to photoabsorption by diatomic systems could increase the absorption coefficient at long wavelengths. Another improvement of the theory is to use methods making it possible to go beyond the limitations of models with linearly intersecting terms (see, for example, [19]).

Note also that formulas (25), (29), and (31) refer to the frequency range of interest to us, where the quantum energy $\hbar\omega$ is considerably less than the splitting term ΔU_{ug} at the point R_0 where $U_g(R_0) = 0$ ($R_0 = 1.12\ a_0$ and $\Delta U_{ug}(R_0) = 22.2$ eV for the H_2^+ ion). When $\hbar\omega > \Delta U_{ug}(R_0)$, the classically permitted region of internuclear distances does not affect the photodissociation cross section, and only the contribution from the continuum is present. We do not consider this case of large transition frequencies here.

3. RESULTS AND DISCUSSION

We calculated the total molecular (quasi-molecular) ion H_2^+ absorption coefficient for several values of ω and T using formula (31) and the data from Table 2. The results for $k_T(\omega)$ are presented in Table 3.

The results show that, at the temperatures $T = 4500$–6500 K typical for the solar photosphere, after a very small decrease at $0.25 \le \hbar\omega < 1$ eV, the H_2^+ photoabsorption coefficient (31) increases with the frequency ω. This behavior is primarily determined by the Boltzmann factor $\exp[|U_g(R_\omega)|/kT]$. The increase in ω is followed by a decrease in the internuclear distance R_ω corresponding to the phototransition, and, accordingly, by an increase in the absolute value of the potential energy $|U_g(R_\omega)|$. (Recall that $U_g(R_\omega) < 0$ in the frequency range under consideration; see Table 2.) Absorption will occur from the lower levels vK, whose populations increase as the vibrational quantum number v decreases. The absorption coefficient $k_T(\omega)$ monotonically decreases as $\exp[|U_g(R_\omega)|/kT]$ as the temperature rises.

Table 4. $\beta_T(\omega)$ calculated using (31), (33), and (34) for T = 4500, 5800, 8000, and 10000 K, assuming the number densities of N_e and N_{H^+} are equal

$\hbar\omega$, eV	λ, μm	T, K			
		4500	5800	8000	10000
		β_T, %			
5.70	0.22	63.8	41.1	30.3	27.5
4.93	0.25	40.3	28.9	23.5	22.5
4.26	0.29	25.7	20.4	18.4	18.5
3.68	0.34	16.7	14.7	14.5	15.2
3.17	0.39	11.1	10.7	11.5	12.6
2.74	0.45	7.7	8.0	9.4	10.6
2.36	0.53	5.4	6.2	7.7	9.1
2.03	0.61	4.1	5.0	6.9	8.0
1.74	0.71	3.2	4.2	5.4	7.2
1.50	0.83	2.7	3.7	5.5	6.8
1.28	0.97	2.6	3.6	5.4	6.7
0.86	1.43	5.6	7.2	8.3	9.2
0.58	2.14	10.0	8.0	6.6	6.0
0.54	2.28	9.0	7.2	6.0	5.5
0.38	3.22	4.7	4.0	3.5	3.3
0.25	4.90	2.2	2.1	1.7	1.6

Let us compare the resulting values for the H_2^+ absorption coefficient $k_T(\omega)$ and the total coefficient for absorption by the negative ion H^- via the process (1)

$$k_{H^-}^{b\text{–}fr}(\omega) = \sigma_{H^-}(\omega)N_{H^-} = \sigma_{H^-}(\omega) \times \left\{\frac{1}{4}\left(\frac{2\pi\hbar^2}{m_e kT}\right)^{3/2} \exp\left(\frac{|E_{H^-}|}{kT}\right)\right\} N_H N_e \ [\text{cm}^{-1}] \quad (33)$$

and via free–free transitions (2)

$$k_{e\text{–}H}^{fr\text{–}fr}(\omega) = \langle v_e \sigma_{e\text{–}H}\rangle_T N_H N_e \ [\text{cm}^{-1}]. \quad (34)$$

Here, $\sigma_{H^-}(\omega)$ [cm^2] is the cross section for the photoejection (1) of an electron from an H^- ion and $\langle v_e\sigma_{e\text{–}H}\rangle$ [cm^4 s] is the effective cross section for photoabsorption (2), normalized to a unit flux of electrons with velocity v_e colliding with the H(1s) atom (for details, see [14]).

Let us consider the ratio

$$\beta_T(\omega) = \frac{k_{H_2^+}^{ph.d}(\omega) + k_{H^+\text{–}H}^{fr\text{–}fr}(\omega)}{k_{H^-}^{b\text{–}fr}(\omega) + k_{e\text{–}H}^{fr\text{–}fr}(\omega)} = \frac{k_T(\omega)}{k_{H^-}^{b\text{–}fr}(\omega) + k_{e\text{–}H}^{fr\text{–}fr}(\omega)}, \quad (35)$$

determined by (31), (33), and (34). It follows from these formulas that, when $N_e = N_{H^+}$, $\beta_T(\omega)$ is a dimensionless parameter that depends only on the frequency ω and the temperature T. Values for $\beta_T(\omega)$ are presented in Table 4. We used the photoejection cross sections $\sigma_{H^-}(\omega)$ from [2] and the results of [3] for $\langle v_e\sigma_{e\text{–}H}\rangle$ for the absorption coefficient (34) for free–free transitions (2).

Thus, the values of $\beta_T(\omega)$ in Table 4 characterize the additional photoabsorption by molecular and quasimolecular H_2^+ ions over the total photoabsorption by the negative ions H^- and collisions of electrons with neutral hydrogen atoms H. Note that the H_2^+ absorption spectrum extends to frequencies considerably greater than those in Tables 2–4. However, a comparison of the H_2^+ and H^- absorption coefficients is meaningless at energies $\hbar\omega > 4.93$ eV, since absorption from the triplet level $3s3p\ ^3P$ of the Mg atom becomes dominant (see [1]).

The frequency range $\hbar\omega \sim 0.5$–3 eV, which approximately corresponds to the half-width of the Planck distribution for black-body emission at temperature $kT \sim 0.5$ eV, is of particular interest for studies of solar emission. In this frequency range, $\beta_T(\omega)$, which specifies the relative contributions of photoabsorption by the H–H^+ system and photoabsorption via (1) and (2), is, on average, equal to ~6–7% and is only weakly dependent on temperature. There is a considerable increase in $\beta_T(\omega)$ (by ~30–40%) at $\hbar\omega \sim 3$–5 eV due to both the increase in $k_T(\omega)$ [see (31) and Table 3] and the decrease in the absorption coefficients for H^- ions and free–free electron transitions in the field of the hydrogen atom, which are determined by (33) and (34). However, the range $\hbar\omega \sim 3$–5 eV is of little interest for calculations of the radiation integrated over the spectrum, since its contribution is appreciably suppressed by the exponential dependence of the Planck distribution.

For stars hotter than the Sun with temperatures T = 8000–10000 K, the range of photon energies $3 < \hbar\omega < 5$ eV either partially (at T = 8000 K) or completely (T = 10000 K) overlaps the half-width of the Planck distribution. The results presented above (Table 4) show that photoabsorption by H_2^+ ions substantially increases the total absorption coefficient. In this case, the characteristic values of $\beta_T(\omega)$ are approximately 7–12% at visual wavelengths and can be as large as 20–30% at short wavelengths.

At temperatures of about 3000 K, the contribution of photodissociation of H_2^+ ions and free–free phototransitions in the H–H^+ system integrated over the spectrum is approximately 3% of the total contribution of photoabsorption by H^- and free–free electron transitions. However, the relative contributions of photoabsorption by the H–H^+ system and of photoabsorption

via processes (1) and (2) appreciably increases at short wavelengths, and the corresponding values of $\beta_T(\omega)$ reach ~50–150% at energies $4.5 < \hbar\omega < 5.5$ eV. Note also that the free–free electron phototransitions in the fields of neutral hydrogen molecules H_2, whose number density sharply increases with decreasing temperature, must be also taken into account when considering absorption in stellar atmospheres with temperature $T \sim 3000$ K.

ACKNOWLEDGMENTS

We are grateful to A.A. Boyarchuk for stimulating discussions. This work was supported by the Russian Foundation for Basic Research (project no. 99-02-16602) and the "Integratsiya" Federal Program (grant 2.1-35).

REFERENCES

1. A. Unsöld and B. Baschek, *The New Cosmos* (Springer, Berlin, 1991).
2. M. Venuti and P. Decleva, J. Phys. D **30**, 4839 (1997).
3. K. L. Bell and K. A. Berrington, J. Phys. B **20**, 801 (1987).
4. R. Wildt, Observatory **64**, 195 (1942); R. Wildt, Astron. J. **54**, 139 (1949).
5. D. R. Bates, J. Chem. Phys. **19**, 1122 (1951); D. R. Bates, K. Ledsham, and A. L. Stewart, Philos. Trans. R. Soc. A **246**, 215 (1953).
6. D. M. Bishop and L. M. Cheung, J. Phys. B **11**, 3133 (1978).
7. D. R. Bates, Mon. Not. R. Astron. Soc. **112**, 40 (1952).
8. L. D. Landau and E. M. Lifshitz, *Statistical Physics* (Nauka, Moscow, 1976; Pergamon, Oxford, 1980).
9. R. A. Buckingham, S. Reid, and R. Spence, Mon. Not. R. Astron. Soc. **112**, 382 (1952).
10. R. L. Kurucz, *Atlas: A Computer Program for Calculating Model Stellar Atmospheres*, Spec. Report No. 309 of Smith. Astrophys. Obs.
11. Yu. D. Oksyuk, Opt. Spektrosk. **23**, 214 (1967).
12. G. H. Dunn, Phys. Rev. A: Gen. Phys. A **172**, 172 (1968).
13. K. P. Huber and G. Herzberg, *Molecular Spectra and Molecular Structure: IV. Constants of Diatomic Molecules* (Van Nostrand Reinhold, New York, 1979; Mir, Moscow, 1984), Chap. 1.
14. I. I. Sobel'man, *Introduction to the Theory of Atomic Spectra* (Nauka, Moscow, 1977).
15. V. S. Lebedev and V. S. Marchenko, Tr. Fiz. Inst. im. P. N. Lebedeva **145**, 79 (1984).
16. L. D. Landau and E. M. Lifshitz, *Quantum Mechanics: Nonrelativistic Theory* (Nauka, Moscow, 1974; Pergamon, Oxford, 1977).
17. V. S. Lebedev, J. Phys. B: At. Mol. Opt. Phys. B **24**, 1993 (1991).
18. *Handbook of Special Functions*, Ed. by M. Abramovits and I. Stigan (Nauka, Moscow, 1979).
19. E. E. Nikitin and S. Ya. Umanskiĭ, *Nonadiabatic Transitions in the Presence of Slow Atomic Collisions* (Atomizdat, Moscow, 1979).

Translated by Yu. Dumin